ANALYSIS TECHNIQUES AND DIAGNOSTICS OF LOW β HADRON BEAMS

By

Christopher James Richard

A DISSERTATION

Submitted to
Michigan State University
in partial fulfillment of the requirements
for the degree of

Physics - Doctor of Philosophy

2020

ABSTRACT

ANALYSIS TECHNIQUES AND DIAGNOSTICS OF LOW β HADRON BEAMS

By

Christopher James Richard

Beam diagnostics are essential to the operation of particle accelerators. They are used to tune the accelerator, verify beamline modes, and ensure minimal beam loss and crucial to the machine protection systems. The diagnostic suite is usually set when the accelerator is initial constructed. If additional measurements are desired, it can be challenging to add new diagnostic devices due to spacial constraints. Another approach to gain more information about the beam is to develop new analysis techniques for the existing diagnostic devices.

This thesis presents further analysis of measurements from two devices. Firstly, it discusses converting phase space measurements taken with an Allison scanner from position-angle coordinates to action-phase coordinates. In this coordinate system, the distribution is stable under changes to linear optics. This allows for direct comparison of phase space measurements taken at different locations or with different transverse focusing. Secondly, beam profile measurements taken with Beam Position Monitors (BPMs) by measuring multiple harmonics are presented. The measurements are primarily focused on non-relativistic beams and the challenges associated with these measurements.

Lastly, the design of a test stand to calibrate BPMs for non-relativistic effects is presented. The test stand relies on a helical transmission line can can propagate signals with phase velocity of 0.03c.

TABLE OF CONTENTS

LIST OF TABLES

LIST OF FIGURES

Chapter 1

Introduction

1.1 Hadron Accelerators

Hadron accelerators play a critical role in fundamental science as well as industry. Nuclear physics makes use of heavy ion accelerators to produce rare isotopes for studies. These machines, such as FRIB, continualy push towards higher beam intensities to increase the creation rate of rare isotopes. The high intensity beams can quickly cause significant damage to the accelerator if even a small portion of the beam is lost. Similar issues are faced by proton accelerators, such as the Large Hadron Collider at CERN and the Proton Improvement Plan 2 upgrade at Fermilab, that push for higher and higher energies for high energy physics experiments. Other hadron machines used in industry and medical fields, require minimal beam losses to minimize down time.

Essential to all of these accelerators is a diagnostics suite to ensure a high quality beam is passing through the accelerator with minimal losses. The diagnostic system typically includes a variety of devices to measure the beam current, position, size, and other properties.

Ensuring minimal losses starts at the low energy front end which is significantly longer than electron accelerators due to the mass of hadrons causing them to accelerator slower. Measurements of the beam position and size need to be taken to ensure the beam is properly matched to the rest of the accelerator. If the beam is too large or has significant halo or tails, the extraneous particles can be removed via purposefully scraping the beam with less concern

of radiation from the particles hitting the scraper or boring holes through the scraper. The lower energy also causes the beam to be less rigid allowing for more manipulation of the beam which can enable certain diagnostic techniques and use of certain devices.

The first step in ensuring a quality beam is leaving the low energy front end is to measure the beam. To do this, we need to understand the signals produced by the diagnostic devices, how they relate to the beam, and their limitation. This ongoing study of existing devices can lead to development of new diagnostics or to devise new analysis techniques that can be applied to glean more information about the beam.

This thesis discusses new techniques for two diagnostics. Chapter 2 presents an analysis technique for space space distribution measurements using action-phase coordinates instead of the standard position-angle coordinates. Chapter 3 discusses broadband measurements using Beam Position Monitors (BPMs) to measure the bunch profile. This focuses on beams traveling at non-relativistic velocities where the measured signals must be related to be beam through the electric field. In chapter 4, the design on a BPM test stand capable of calibrating for the non-relativistic effects outlined line chapter 3 is presented. Chapter 5 concludes this thesis with a brief discussion on the challenges of the presented techniques and optimistic hope for better measurements in the future.

Chapter 2

Analysis of Phase Portraits using Action-Phase Coordinates

It is insufficient for prevention of beam loss to only measure the beam profiles at a given location. As the beam is transported down the beamline, particles move in transverse position-velocity ($x - x'$) phase space and alternate between having large traverse position offsets x and large transverse velocities x'. The transverse velocity is typically normalized to the longitudinal velocity and called angle and denoted in radians. Therefore, if the beam size in position is measured at a given location and it appears to be sufficiently small to avoid losses downstream, it is possible for particles that had small offset but large angle to later have smaller angles and larger offsets and be lost. By measuring the beam distribution in $x - x'$ phase space it can be ensured that the beam is within the admittance of the beamline, i.e. the maximum size in phase space that can be transported through the accelerator without losses. The distribution in phase space is often characterized in terms of the emittance ϵ and

Twiss parameters

$$\epsilon = \sqrt{\langle x^2 \rangle \langle x'^2 \rangle - \langle xx' \rangle^2} \tag{2.1}$$

$$\beta = \frac{\langle x^2 \rangle}{\epsilon} \tag{2.2}$$

$$\alpha = -\frac{\langle xx' \rangle}{\epsilon} \tag{2.3}$$

$$\gamma = \frac{\langle x'^2 \rangle}{\epsilon} = \frac{1+\alpha^2}{\beta} \tag{2.4}$$

where the terms in $\langle ... \rangle$ are the second order moments of the phase space distribution and are often rms values. The emittance is the area in phase space that the beam occupies and is a conserved quantity for linear focusing. The emittance is often normalized by multiplying by the product of the relativistic factors $\beta_r \gamma_r$ so it remains constant during acceleration. The maximum ϵ than can be transported through the beamline is known as the acceptance. Measurements of the phase space, referred to as phase portraits here, are taken to ensure the beam is within the acceptance. Particles far from the beam center are typically considered to be part of the beam tails or halo [1, 2]. These particles are the most likely to be lost in the accelerator. Therefore, knowledge of the size and extent of the beam tails in phase space is desired so they can be removed via scraping if necessary.

However, measuring tails is challenging. A variety of techniques and definitions are used to measure and quantify beam tails [3, 4], however, understanding the dynamics of the distribution from direct comparison of different phase portraits in $x - x'$ coordinates is challenging since the portraits may differ dramatically when the Twiss parameters change even for purely linear optics (e.g. Fig 2.14 (a)) [1]. Instead, it can be beneficial to describe

the phase portraits in action-phase coordinates. The action J and phase ϕ are defined as

$$J = \frac{1}{2}\left(\gamma x^2 + 2\alpha x x' + \beta x'^2\right) \tag{2.5}$$

$$\phi = -\arctan\left(\frac{\alpha x + \beta x'}{x}\right) \tag{2.6}$$

where α, β, and γ are the Twiss parameters and x and x' are the position and angle coordinates of a particle [5].

In linear optics with no x-y coupling, action is a constant of motion, i.e. the action of a particle remains the same along the beamline even if the optics settings are changed. Therefore, a description of the particle distribution over the action provides a more stable description of the beam, allowing for easier distinction of beam tails and changes in the beam distribution.

There are many different types of instruments for measuring the transverse phase space distributions including pepperpots, tomography, slit-harp scanners, two slit scanners, and Allison-type scanners. The phase space measurements presented in this chapter were taken with an Allison scanner in the Medium Energy Beam Transport line (MEBT) at the Proton Improvement Plan II Injector Test (PIP2IT) facility at Fermilab [6]. Allison scanners [7] consist of a rigid box with a thin slit on either end and a variable electric dipole between the slits (Fig. 2.1). The beam is intercepted by the front plate and particles can only pass through the first slit to select narrow position range. The passed beamlet is deflected by the dipole field until it strikes rear wall. If the particles have the correct transverse angle then the deflection will cause the particles to pass through the second slit and into a Faraday cup to measure the passed current. For an Allison scanner of length ℓ and a beam of mass m

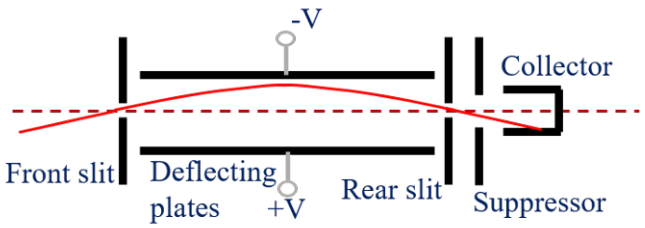

Figure 2.1: Simplified schematic of an Allison scanner. The red line shows the trajectory of particles through the device.

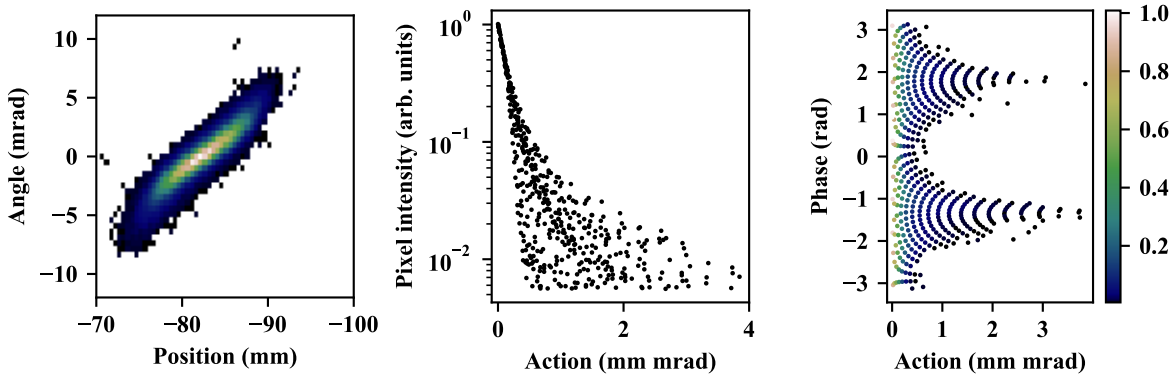

Figure 2.2: Measured phase portrait in $x - x'$ coordinates and $J - \phi$ coordinates taken at location 1.

traveling at $v = \beta c \ll c$ the passed angle x_0' for a given voltage V is

$$x_0'(V) = \frac{qV\ell}{2m\beta^2c^2}. \tag{2.7}$$

The 2D transverse phase space can therefore be measured by stepping the whole box through the beam so the front slit can take slices at different positions and at each position the electric dipole strength is swept to scan a range of angles. At each position-dipole setting the current on the Faraday cup is measured to determine the intensity of the beam in the small phase space area that passed through the scanner. An example of a phase portrait measured with an Allison scanner is shown in Fig 2.2 in $x - x'$ coordinates and with each pixel converted into $J - \phi$ coordinates.

Table 2.1: Parameters of the PIP2IT MEBT Allison scanner

Parameter	Value	Unit
Slit size	0.2	mm
Slit separation	320	mm
Plate voltage	±1000	V
Plate length	300	mm
Plate separation	5.6	mm
Maximum measurable angle at 2.1 MeV	±12	mrad

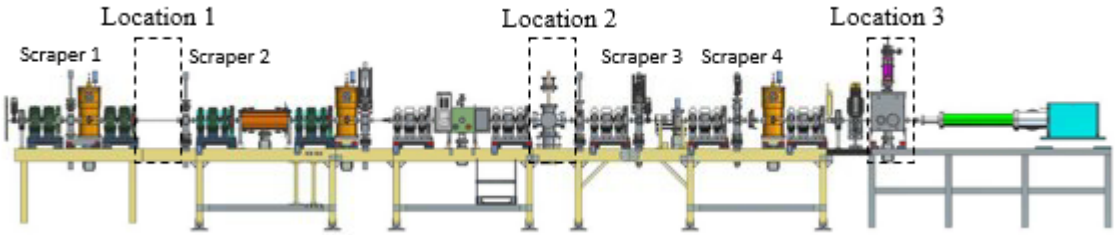

Figure 2.3: Final configuration of the PIP2IT MEBT (side view). Transverse focusing is provided by quadrupoles with two doublets and seven triplets.

The PIP2IT MEBT was assembled and beam measurements were performed in several stages between 2016 - 2018. Its configuration at the end of 2018 run is shown in Fig. 2.3. The main beam parameters are summarized in Table 2.2. The Allison scanner was used in three locations and was moved at different phases of the MEBT construction:

1. In section #1, downstream of the second doublet, in the horizontal position
2. In section #5, in lieu of the absorber prototype, in the vertical position
3. Toward the end of the line as shown in Fig. 2.3, in the vertical position.

Most of the measurements presented there were taken in the first location of the Allison scanner (Fig. 2.4). Results from other two locations are explicitly noted.

Table 2.2: PIP2IT MEBT beam parameters

Parameter	Value	Unit
Beam energy	2.1	MeV
Macro-pulse repetition rate	1-20	Hz
Macro-pulse length	0.005-25	ms
Bunch repetition rate	162.5	MHz
Pulse beam current	Up to 10	mA
Transverse emittance, rms norm.	≤ 0.23	mm mrad
Longitudinal emittance, rms norm.	≤ 0.34	mm mrad

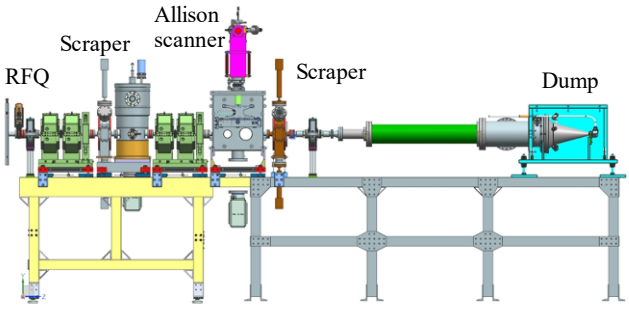

Figure 2.4: Initial MEBT configuration.

2.0.1 Allison scanner noise

Measurements with the PIP2IT MEBT Allison scanner unfortunately were noisy. The noise floor of the scanner was relatively large compared to the measured beam intensities. For a typical scan of a 5 mA beam, its rms noise is 0.2%-0.3% of the maximum amplitude for nominal operation. This limited the dynamic range of the device to ∼2 orders of magnitude.

In addition, the beam properties varied during the time it takes to make a scan (approximately 5 minutes for typical scans). Significant jitter of the beam centroid was measured with the BPMs in the MEBT, but the source of the jitter could not be located nor the jitter eliminated [8]. In the MEBT, the jitter is predominately in the vertical plane with the amplitude varying along the beamline in accordance with the optics and reaching up to 0.2 mm rms in amplitude. Spectral analysis of the BPM readings shows the jitter has frequencies up to ∼3 Hz with no dominant harmonics. Therefore, even individual angular scans are affected

as it takes ∼1 s to sweep the voltage over the angle range while measuring at 20 Hz. [9] The majority of the results presented in the following sections use measurements taken in the first location of the Allison scanner where the scanner was oriented horizontally to reduce the effects of the jitter.

To estimate the effect of the jitter on the pixel amplitude, multiple phase portraits taken with the same focusing were used to estimate the rms scatter at each pixel σ_{I_i} [10]. At location 2, this was found to increase approximately linearly with the pixel amplitude I_i (Fig. 2.5 left) with the linear fit

$$\sigma_{I_i} = 0.0067 + 0.024 I_i. \tag{2.8}$$

The intensities vary by 2-3% for pixels near the center of the beam and is dominated by electronic noise at low intensities. The error bars shown in results from measurements taken at location one follow Eq. 2.8.

For measurements taken at locations two and three, the jitter in the vertical plane significantly increases the variation in the pixel amplitude and follow the general trend (Fig. 2.5 right)

$$\sigma_i = \begin{cases} 0.01 + 0.3 I_i & \text{for } I_i < 0.9 \\ 0.28 & \text{for } I_i \geq 0.9 \end{cases} \tag{2.9}$$

This jitter has minimal effect on the measured rms parameters of the beam and causes an error of only ∼2% [9]. However, it confounds detailed measurements of the distribution in phase space and beam tails.

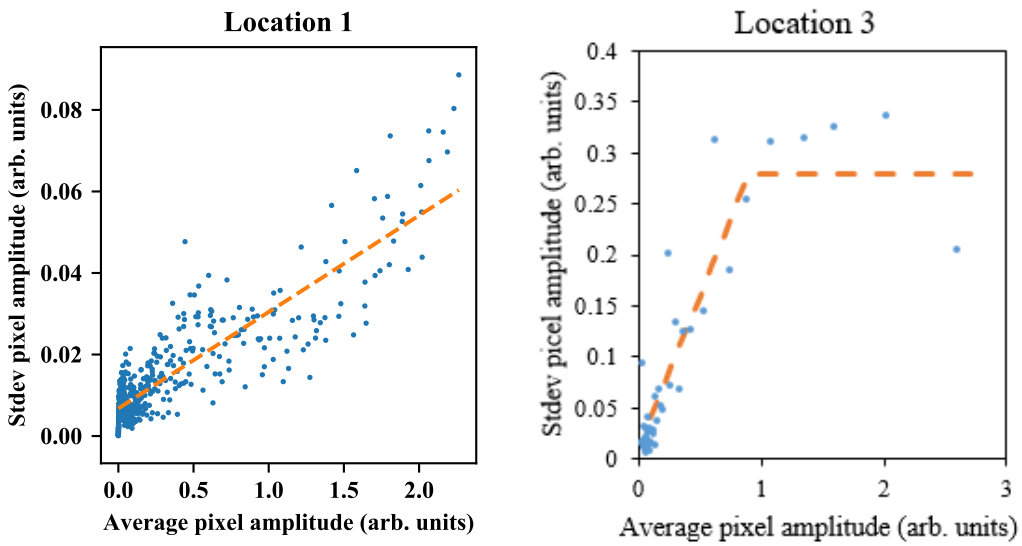

Figure 2.5: The rms scatter of the pixel amplitudes plotted as a function of the average amplitudes (blue) phase portraits measured at location one (left) and location three (right). The orange lines show the fit from Eqs.(2.8) and (2.9).

2.1 Beam description using $J - \phi$ coordinates

2.1.1 Core description

When the phase portraits measured in the MEBT were converted to action-phase coordinates, it was found that in the central portion of the beam, i.e. at small actions, the pixel amplitude is mostly independent of the phase and decreases exponentially with action

$$I_{\text{gauss}} = I_0 e^{-J/\epsilon_c} \tag{2.10}$$

which describes a Gaussian distirbution in $x - x'$ coordinates. On semi-logarithmic scale, Eq. (2.10) represents a straight-line with slope $-1/\epsilon_c$, ϵ_c is referred to here as the central slope. Since Eq. (2.10) describes a perfect Gaussian distribution, the central slope can be interpreted as the rms emittance of the beam if the Gaussian core was extended and the tails removed.

2.1.2 Discussion on the beam distribution

The beam arrives to the MEBT after passing ∼12 betatron periods in the RFQ. After experiencing multiple betatron oscillations in a periodic structure, the beam is expected to relax toward the Maxwell-Boltzmann distribution [11], which corresponds to Eq. (2.10). However, it was not obvious that Eq. (2.10) would adequately describe the portraits measured at the PIP2IT MEBT. One considerations was that the distribution of the beam coming out of the ion source significantly deviates from Eq. (2.10) for all actions since the beam is initially spatially limited by the ion source extraction aperture resulting in the beam distribution coming for the ion source being uniform in position and Guassian in angle. This distribution, referred to here as uniform-Gaussian (UG), is clearly seen in the phase portraits recorded near the ion source in the PIP2IT low energy beam transport line (LEBT) [12]. The UG distribution, projected into one plane and expressed in terms of action-phase, is very different from the Gaussian's:

$$I_{UG}(J,\phi) = I_0\sqrt{1-\frac{J\cos^2(\phi)}{2\epsilon_{UG}}}e^{-\frac{J\sin^2(\phi)}{\epsilon_{UG}}} \times H\left(1-\frac{J\cos^2(\phi)}{2\epsilon_{UG}}\right) \tag{2.11}$$

where ϵ_{UG} is the rms emittance and H is the Heaviside function

$$H(x) = \begin{cases} 0 \text{ if } x < 0 \\ \\ 1 \text{ if } x \geq 0 \end{cases}. \tag{2.12}$$

Two other models commonly used for approximating the beam distribution are the Kapchinskiy-Vladimirskiy (KV) and waterbag (WB) distributions. In action they are

$$I_{KV}(J,\phi) = I_0 \cdot H\left(1 - \frac{J}{2\epsilon_{KV}}\right) \tag{2.13}$$

$$I_{WB}(J,\phi) = I_0 \left(1 - \frac{J}{3\epsilon_{WB}}\right) H\left(1 - \frac{J}{3\epsilon_{WB}}\right) \tag{2.14}$$

where ϵ_{KV} and ϵ_{WB} are the corresponding emittances.

In Fig. 2.6, the high-amplitude pixels within the normalized action $J < 0.15$ mm mrad (containing 60% of the measured beam), are plotted together with fits of the idealized distributions Eq.2.10, Eq. 2.11, Eq. 2.13, and Eq. 2.14. The Gaussian distribution Eq. (2.10) is the best fit with reduced $\chi^2 = 2.07$. For a waterbag distribution, the reduced $\chi^2 = 6.55$ while the UG and KV distributions poorly fit the data with the reduced χ^2 of 47 and 687 respectively.

The large absolute value of χ^2 for the Gaussian fit indicates that Eq. (2.10) does not fully catches the distribution details. Moreover, the χ^2 value grows quickly when including in the fit additional pixels with larger action. The growth is caused primarily by appearance of a phase dependence of the pixel amplitudes, which is discussed below.

2.1.2.1 Central parameters

The first attempts to compare the measured data with Eq. (2.10) showed a relatively large scatter of pixel intensities for any given action, even at low actions (Fig. 2.7, blue). This was caused by the choice of Twiss parameters used to define the action which can significantly affect the distribution in $J - \phi$ coordinates. For the distribution of Fig. 2.7, blue, the Twiss parameters used were the rms parameters of the entire beam (referred here as the rms Twiss

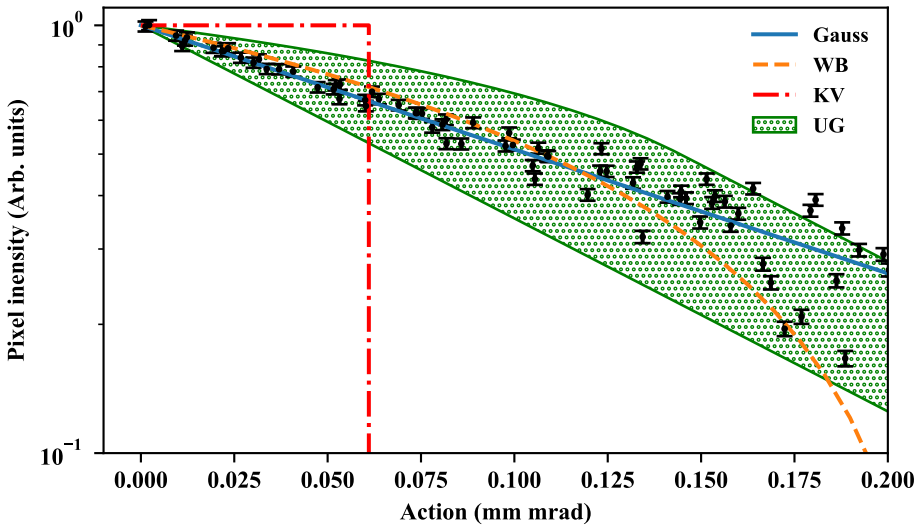

Figure 2.6: Comparison of the measured distribution in action in the beam core (black) with several ideal distributions: Gaussian, KV, UG, and WB. Note that the UG distribution is phase-dependent, and, therefore, pixel intensities vary for a given action and is represented here by the area shaded in green.

parameters). This choice of Twiss parameters results in a large scatter even for particles with low action because it includes the non-Gaussian beam tails.

Alternatively, the action can be defined using pixels in the 'central' portion of the beam. The central portion was found by removing the lower intensity pixels of the beam then fitting Eq. (2.20) to determine the 'central' Twiss parameters and central slope. The fraction removed was scanned from 30-60% of the total intensity in 1% steps. Generally, the central slope increases at large and small cuts (Fig. 2.8). The increase at small cuts is attributed to the tails affecting the fit and at large cuts poor statistics increases the central slope significantly when the number pixels is below ∼30. To avoid both of these effects, the central slope was fit to a cubic polynomial and the cut was chosen to be the point closest to the minimum of the fitted curve.

When these central Twiss parameters are used to define action, the scatter in the beam's central region is reduced (Fig. 2.7, red). This is seen in the reduced χ^2 for fitting Eq. 2.10

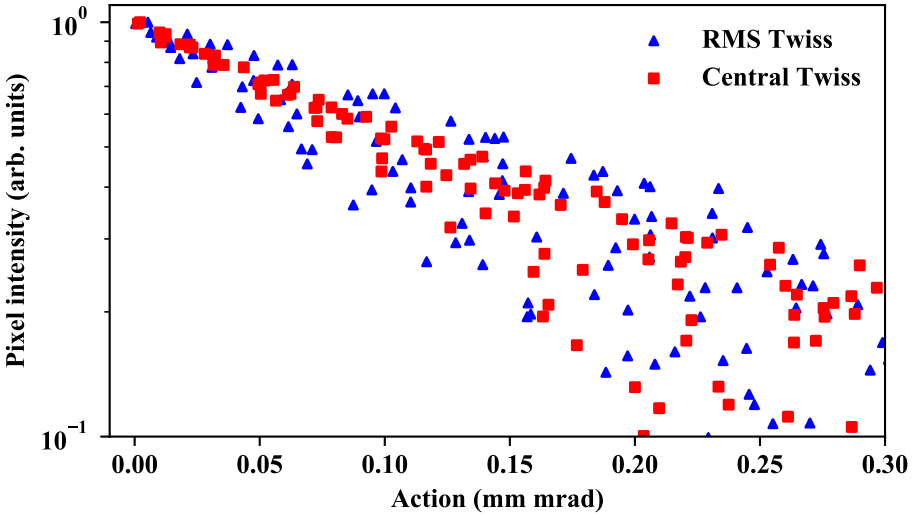

Figure 2.7: Action distribution using central Twiss parameters (red) and rms Twiss parameters (blue).

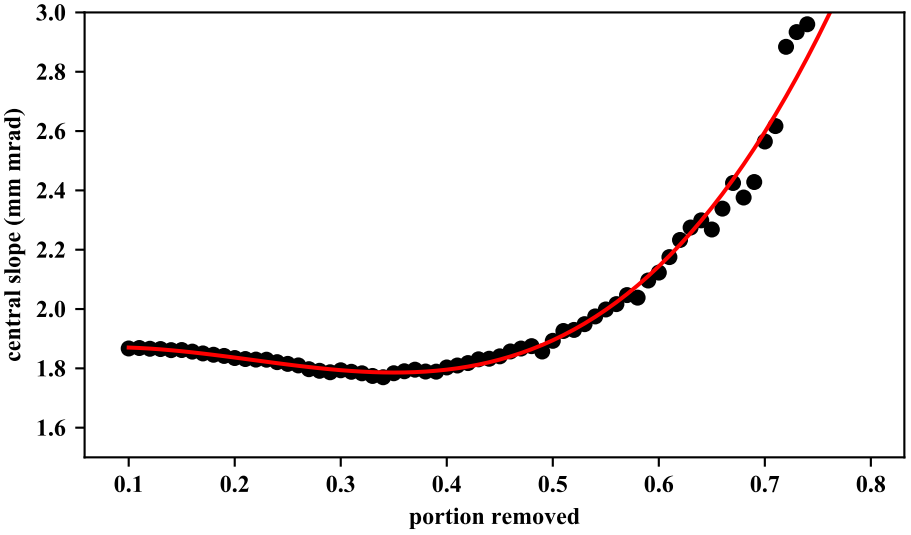

Figure 2.8: Central slope as a function of the portion of the beam removed. The curve is fit to a cubic polynomial.

to pixels with $J < 0.15$ mm mrad which is 64 when using the rms Twiss parameters and 2 when using the central Twiss parameters.

2.1.3 Allison scanner phase dependence

Equation 2.7 to determine the passed angle for a given voltage assumes the slits in the Allison scanner are infinitesimally small. In reality the slits have finite size $2d$. This causes the measured phase space area for every position-voltage setting to be a rhomboid (Fig. 2.9) with vertices at

$$\left(x_0 + d, x_0'\right) \tag{2.15}$$

$$\left(x_0 - d, x_0'\right) \tag{2.16}$$

$$\left(x_0 + d, x_0' - \frac{2d}{\ell}\right) \tag{2.17}$$

$$\left(x_0 - d, x_0' + \frac{2d}{\ell}\right). \tag{2.18}$$

This distorts the measured distribution from the true distribution. For example, if a pure 2D Gaussian is measured with an Allison scanner of slit to slit length ℓ and slits y_1 and y_2 the measured intensity distribution is given by integrating over both slits [13]

$$I_{\text{meas}}(x, x') = \frac{1}{4d^2}\int_{-d}^{d}\int_{-d}^{d} \exp\left(-\frac{1}{2\epsilon_c}\left[\gamma(x+y_1)^2 + 2\alpha(x+y_1)\left(x' + \frac{y_2 - y_1}{\ell}\right) + \beta\left(x' + \frac{y_2 - y_1}{\ell}\right)^2\right]\right) \mathrm{d}y_1 \mathrm{d}y_2. \tag{2.19}$$

The integrand was expanded to second order in y_1 and y_2 and the resulting measured dis-

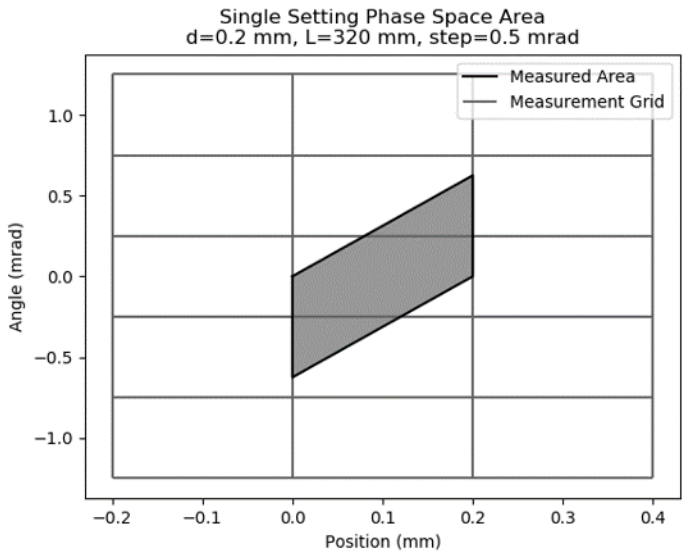

Figure 2.9: The shaded area represents the passed phase space area for a given position and voltage setting of an Allison scanner. The grid is the displayed pixel size.

tribution up to order d^2 is

$$I_{\text{meas}}(x,x') = \exp\left(-\frac{1}{2\epsilon_c}\left[\gamma x^2 + 2\alpha x x' + \beta x'^2\right]\right) \left(1 + \frac{d^2}{6\epsilon_c^2}\left[\epsilon_c\left(\frac{2\alpha}{\ell} - \frac{2\beta}{\ell^2} - \gamma\right) + 2\left(\frac{\alpha x + \beta x'}{\ell}\right)^2 + \left(\alpha x' + \gamma x\right)^2 - 2\left(\frac{\alpha x + \beta x'}{\ell}\right)\left(\alpha x' + \gamma x\right)\right]\right). \quad (2.20)$$

This results in a phase dependence of the pixel intensities for all actions. At large J, when the parameters in Table 2.1 are used, this variation is approximately 2% of the measured intensity variation at a given action and was generally ignored. However, at low J, this distortion needs to be accounted for when defining action central parameters.

The effect of the slits can be seen by varying the strength of a quadrupole magnet directly upstream of the Allison scanner to change the Twiss parameters at the Allison scanner (Fig. 2.10 top). Because this is changing a linear optic, the action distribution and ϵ_c should not

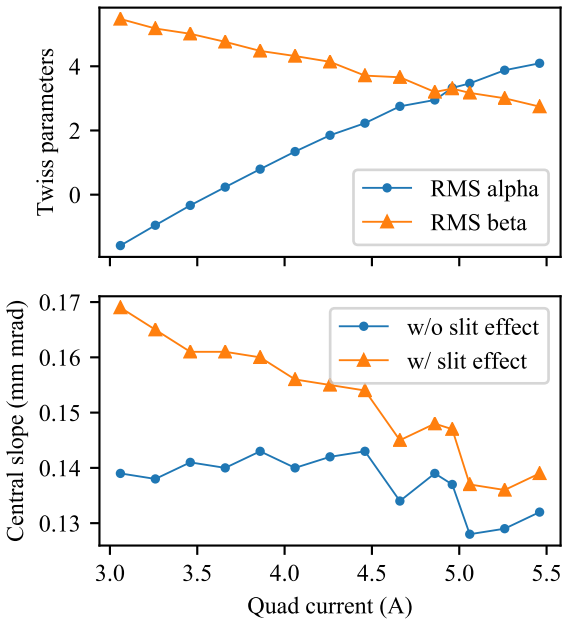

Figure 2.10: Top: Variation of parameters with quadrupole current. Bottom: The central slope is constant when accounting for the slit size.

change. If the slit effect is not accounted for and the central Twiss parameters are found by taking rms values over the high intensity pixels, then the central slope decreases linearly with the quadrupole current (Fig. 2.10 bottom). If instead, the central slope and central Twiss parameters are found by fitting to Eq. 2.20 then ϵ_c is constant within $\pm 5\%$.

2.1.4 Tail description

The distinction between the beam core and tails is defined by the transition action J_{tr} where the distribution deviates significantly from Eq. 2.10. The transition action is found by firstly, determining the central parameters as outlined above and calculating the action and phase of each pixel. Then, all the pixels are sorted into normalized action bins J_i, typically 0.05 mm mrad in size, and the mean amplitude $I(J_i)$ and the standard deviation $\sigma_{Int}(J_i)$ of the amplitude in each action bin is calculated. The value of J_{tr} is defined as the action of the

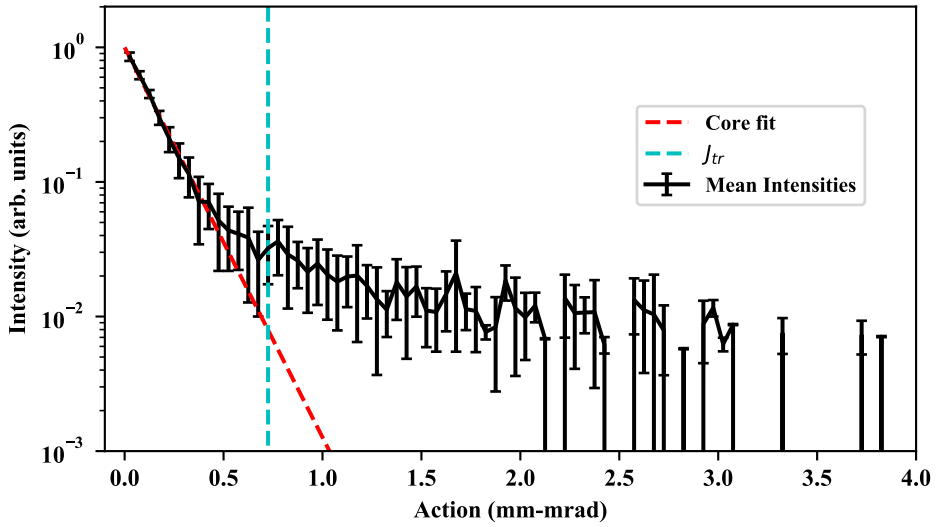

Figure 2.11: The intensities are binned in action to determine J_{tr} with Eq. (2.21) to separate the tails from the core.

bin where the mean amplitude deviates from the fit of Eq. (2.10) by more than three times the standard deviation of the mean (Fig. 2.11)

$$I(J_{tr}) - I_0 e^{-J_{tr}/\epsilon_c} = 3\sigma_{Int}(J_{tr}). \tag{2.21}$$

All particles with action less than the transition action are defined to be in the core, and particles with larger action are in the tail. The percentage of the beam in the tails is typically about 10-20% of the total intensity.

With this definition, the transition action and percent of the beam in the core are constant under linear optics. Therefore, these two parameters can be used as a metric for tail growth due to non-linear effects. In theory the maximum action can also be used. However, in practice, because the pixel with maximum action has intensity just above the noise floor, the maximum action is very noisy and is an unreliable measure.

At actions above J_{tr} the scatter of pixel intensities at a given action visibly increases

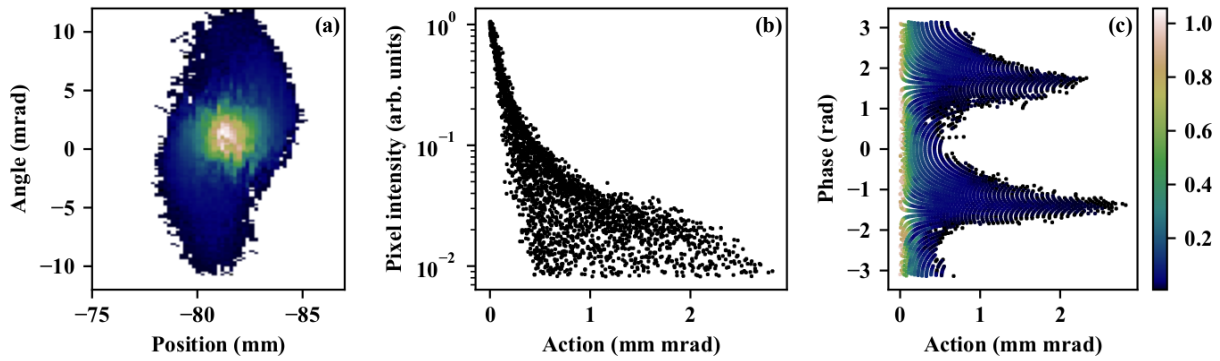

Figure 2.12: Phase portrait in position-angle phase space (a) and action-phase phase space (c). The beam splits into two branches separated in phase at large actions. The pixel amplitude versus action (b) shows deviation from the core distribution at large action.

and clearly deviates from the Gaussian core. The dominant part of this scatter comes from strong phase dependence with the tail being split into two "branches" of similar intensities that are separated in phase by approximately π rad which are clearly evident when the data is plotted in $J - \phi$ coordinates (Fig. 2.12). The location in phase of the branches ϕ_b is defined by the phase of the second harmonic of this distribution. This is found by taking the Fourier transform of the intensities as a function of phase for $J > 1.5J_{tr}$. Unfortunately, attempts to find an analytical description of the tail distribution did not succeed.

Hence, the measured beam distribution is described in action phase coordinates by seven parameters. The beam core is characterized by the central slope ϵ_c and central Twiss parameters α_c, β_c and is defined by pixels with action less than the transition action J_{tr}. All particles with action larger than the transition action are in the tails which are characterized by the phase of the branches ϕ_b, the maximum action $J_{\max}$, and the fraction of the particles in the core.

Note that because the beam centroid jitter is assumed to be from a single source and therefore predominately along a single line in phase space, it would add an asymmetry for an initially symmetric distribution. This effect was modeled using a 2D Gaussian distribution

with rms parameters equal to the typically measured central parameters and 0.2 mm rms position jitter added. The resulting asymmetry, quantified by the amplitude of the second harmonic in phase calculated for pixels with actions $J > 0.5$ mm mrad, was found to be at least an order of magnitude lower than observed in measurements.

2.2 Selected beam measurements

2.2.1 Background removal

After taking a scan, the scanner operating program removes the background and calculates the RMS parameters of the phase portrait. The background removal is performed by setting to zero all pixels with intensity less than a user-defined threshold. By default, the threshold is set to 1% of the peak intensity, which is adequate to remove the noise for the nominal 5 mA beam. However, for low intensity beams such rejection does not remove all noise, artificially increasing the reported emittance. And, for high intensity, the cut level can be too aggressive, removing otherwise observable beam tails. Therefore a more robust method was desired.

In order study beam tails, a new method was devised to define the cut threshold based on the noise level and remove only the pixels that cannot be distinguished from the beam signal. This cut level is established by firstly, finding the area that is most likely to contain only noise. The portrait matrix is divided into four identical rectangles, and the rectangle with minimum total intensity is chosen. A 6×6 pixels square in the outermost corner of this rectangle is assumed to contain only noise signal. The mean signal of this square is then subtracted from each pixel over the entire portrait. The rms of the noise level σ_n in this

square is calculated and the cut threshold T_c is set to

$$T_c = A_n \sigma_n. \tag{2.22}$$

To determine the coefficient A_n, let us consider a rectangular portrait containing $N_{pixels} = K \times M$ pixels for which amplitudes are determined by random Gaussian noise so that the probability density P_p of finding a pixel with a given intensity I_p is

$$\frac{dP_p}{dI_p} = \frac{1}{\sqrt{2\pi}\sigma_n} e^{-\frac{I_p^2}{2\sigma_n^2}}. \tag{2.23}$$

The probability P_0 of having a pixel with amplitude A_n times higher than the rms noise amplitude σ_n is

$$P_0 = 0.5\text{erfc}\left(\frac{A_n}{\sqrt{2}}\right) \tag{2.24}$$

and he probability P_1 of having at least one pixel above the threshold is

$$P_1 = 1 - (1 - P_0)^{N_{pixels}} \approx P_0 N_{pixels}. \tag{2.25}$$

The cleaning procedure can use P_1 to set a cut threshold that will remove all the noise. To achieve this then $A_n \approx 3.3$. However, if after the cut single pixels remain above the threshold with all zero neighbors then these can be easily removed. Therefore, the cut level can be set lower and single pixels can be removed after. For this, the cut threshold needs to be set high enough so no pairs of neighboring pixels (side-by-side or diagonally) fluctuate

above $A_n\sigma_n$. The total number of independent neighboring pairs N_{pairs} is

$$N_{pairs} = 4KM - 3(K + M) + 2, \tag{2.26}$$

which tends to

$$N_{pairs} \approx 4N_{pixels} \text{ for } K \gg 1,\ M \gg 1. \tag{2.27}$$

The probability P_2 that two neighboring pixels are both above the threshold is

$$P_2 = 1 - (1 - P_0^2)^{N_{pairs}} \approx 4P_0^2 N_{pixels}. \tag{2.28}$$

In practice, it was accepted that one in ~ 100 portraits may contain an un-removed noise pair ($P_2 = 0.01$) and calculated the value of P_0 from Eq. (2.27) and (2.28) and then the threshold by inverting Eq. (2.24). For a typical number of pixels of 3000, the multiplier in Eq. (2.22) is $A_n \approx 2.2$. For the nominal beam in PIP2IT, the cut threshold calculated with this method is typically $\sim$0.5% of the peak intensity.

To test the robustness of this method, a horizontal scraper was stepped through the beam upstream of the Allison scanner and the phase portraits in the vertical plane were measured at each step. Removal of the beam horizontally results in a lower intensity of a given pixel in the vertical phase space, so that the peak intensity can be used as a measure of the remaining current. When the noise-based cut is used, the measured emittance is constant within 10%, showing that the beam ellipse is not x-y coupled (Fig. 2.13). However, when the same data are analyzed with the 1% cut, the emittance appears to increase when the peak intensity goes below $\sim$1.5, corresponding to a beam current of roughly 2 mA, due to noise flooding the phase portrait.

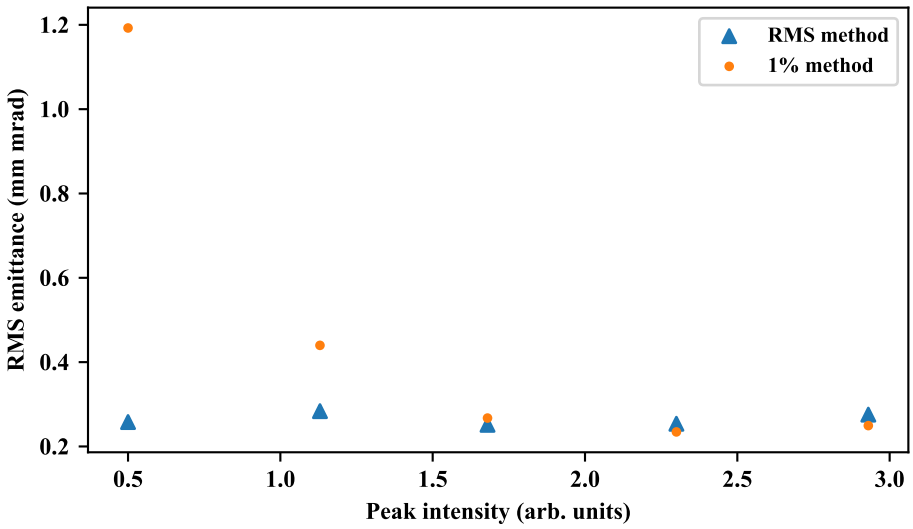

Figure 2.13: Vertical RMS emittance with horizontal scraping. The five data points correspond to 1, 2, 3, 4, 5 mA of beam current after scraping.

2.2.2 Quadrupole scan

To test that the stability of the measured distributions in $J - \phi$ coordinates, the strength of a quadrupole magnet close to the Allison scanner was varied. This is a change to a linear optic so the Twiss parameters will change but no significant changes in the distribution over action are expected. Despite the dramatic visible changes of the portraits in x-x' coordinates (Fig. 2.14(a)), the distribution in action-phase coordinates stays the same (Fig. 2.14 (d,e)), and portion of particles outside of a given action is stable for more than 99% of the measured beam (Fig. 2.14 (f)). The portion of particles in the core and the central slope are found to be stable (Fig. 2.14(b)) within $\pm 3\%$ and $\pm 5\%$, correspondingly.

Note that in a given portrait the particle phase is defined according to Eq. (2.6) with respect to the particles with zero canonical angle, i.e.

$$\phi = 0 \text{ at } x'_c \equiv \frac{\alpha x}{\sqrt{\beta}} + x'\sqrt{\beta} = 0. \tag{2.29}$$

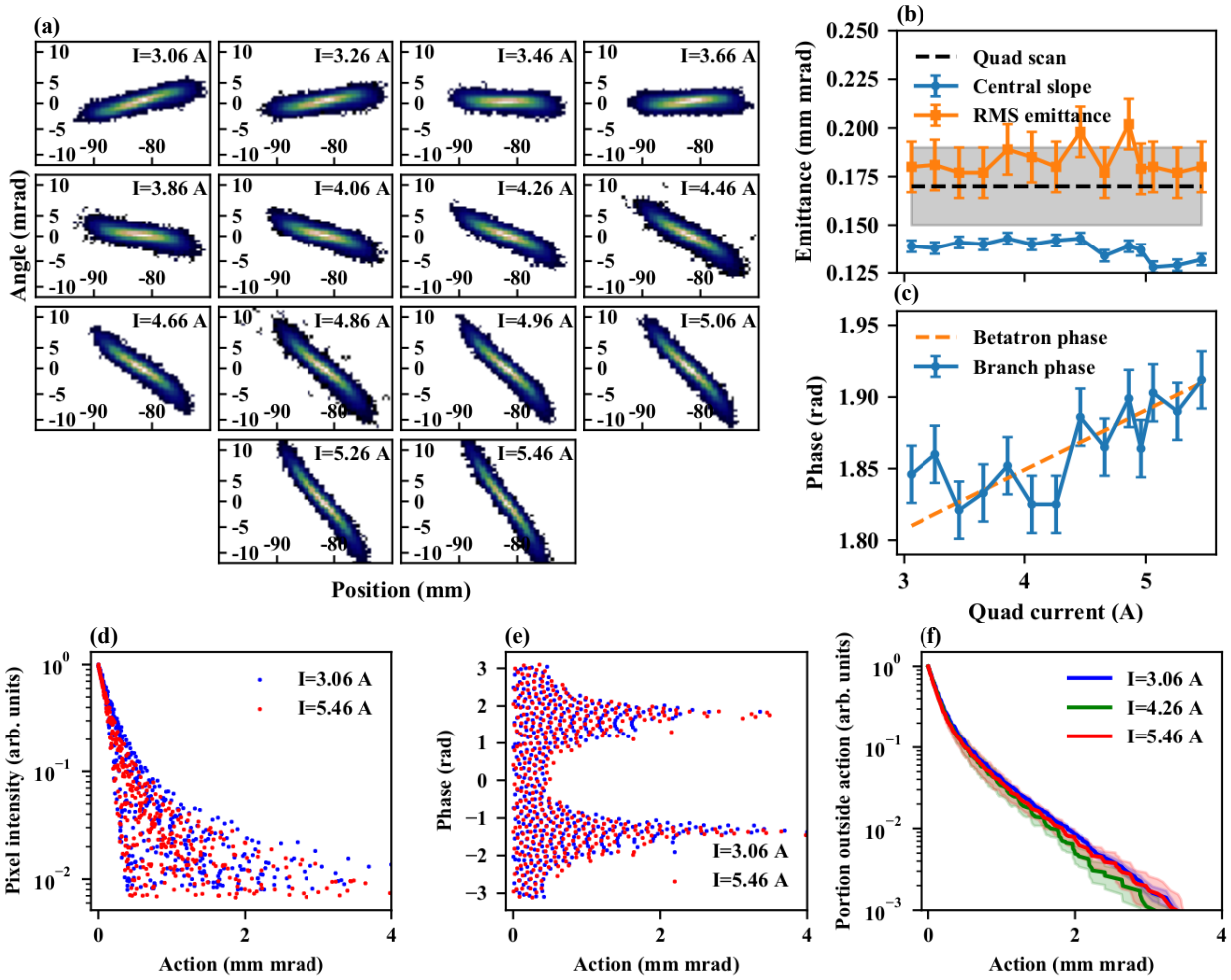

Figure 2.14: Analysis of a quadrupole scan. (a) phase portraits in (x,x') coordinates recorded at the quadrupole currents increasing from left to right and from top to bottom from 3.06A to 5.46 A. The x and x' ranges in each plot are 30 mm and 24 mrad, correspondingly. No significant variation of the slit - corrected central slope and percent in the core are observed while a quadrupole strength was scanned (b). The average branch phase agrees with small changes of the simulated betatron phase (c). Phase portraits in action-phase coordinates for the minimum and maximum quadrupole currents overlap (d), (e). The portion of the beam outside of a given action is stable over most of the beam (f).

Therefore, the phase of the particles for scans with different optics shifts by the difference in betatron phase advance between these portraits. While a phase shift cannot modify the appearance of the phase-independent core, the phase position of the tails should change accordingly. In the case of the presented quadrupole scan (as well as in other quadrupole scans recorded), the actual change in the phase advance is small because the distance between the varied quadrupole and the Allison scanner is small. The observed phase position of the branches is in agreement, within measurement errors, with the simulated phase advance (Fig. 2.14 (c)).

2.2.3 Comparison of measurements in different locations

The stability of description of the distributions in action-phase coordinates allows for comparisons of the phase portraits of the beam that have passed through significantly different optics. As mentioned above, phase portraits were recorded in three locations and with two scanner orientations over 18 months. The results of measurements, performed with the same settings for the ion source, LEBT, and RFQ, are summarized in Table 2.3. Each result represents an average over 10 measurements made on different days in an attempt to separate day-to-day variability from difference between locations and orientation. Errors are the rms error over each set of 10 measurements.

Across all three locations of the Allison scanner, the RMS emittance is the same within these errors. Also, no change, within the scatter, between locations 2 and 3 is observed in the central slope and fraction of intensity in the core, in which the Allison scanner measured in the vertical plane. This is interpreted as an absence of measurable changes in the beam core parameters in the MEBT. Higher values of the central slope and percent in the core at the location 1 are attributed to the difference between the horizontal and vertical planes,

Table 2.3: Average rms emittances and core and tail parameters for the three locations of the Allison scanner. The beam current is 5 mA.

Location	rms ϵ	ϵ_c	% in core
1 - horz	0.20 ± 0.013	0.146 ± 0.003	88 ± 2.5
2 - vert	0.19 ± 0.015	0.117 ± 0.013	71 ± 11
3 - vert	0.22 ± 0.024	0.123 ± 0.011	72 ± 10

since these values stay constant from location 2 to location 3. This difference between the two planes is also seen in the larger spread in intensities at low action for the horizontal plane at location 1 compared to the other two locations (Fig. 2.15 (a)). However, direct comparison by measuring both planes in single location was not performed to confirm this theory. Outside of 99% of the measured beam intensity, the difference between distributions is larger that one would expect from statistical fluctuations and reconstruction errors by comparing with Fig. 2.14 (f). The increase of particle population outside of large actions from location 2 to location 3 visible in Fig. 2.15 (c) may be a sign of tail growth. However, due to the limited dynamic range of the Allison scanner, it is difficult to make a definitely claim.

2.2.4 Distribution at different beam currents

The action distribution can give more information about the beam distribution than the rms parameters. For example, Fig. 2.16 shows how the beam parameters at location 1 vary when the current is increased by increasing the extraction voltage of the ion source. All other settings, tuned to optimize performance at the nominal 5 mA, are kept constant.

Looking solely at the rms parameters that are typically used, an increase in the rms emittance is seen starting at $\sim$3 mA corresponding to the flattening of the peak intensity of the beam. This appears to be a saturation of the beam core resulting in increased tails.

However, the parameters used to describe the action distribution tell a different story. At 3 mA the fraction of the beam in the core plateaus as does J_{tr} signifying minimal tail growth at higher currents. The central slope, however, continues to increase for all currents. At low current, the growth of the central slope is compensated by a reduction in the size of the tails resulting in minimal changes to the rms emittance. Above 3 mA, the central continues to broaden, but tails see less variation. The broadening of the central region results in the increase in the rms emittance, not tail growth.

2.2.5 Scraping

The MEBT contains four sets of four scrapers (each set consists of a bottom, top, right and left scraper) used for collimation and machine protection plus a temporary set of two scrapers (a.k.a. F-scraper, top and right). One goal of the scraping system in the PIP2IT MEBT is to remove far tails. Intercepting part of the beam with the scraping system was foreseen as a normal mode of operation, with preliminary estimates made for a phase-independent Gaussian beam in Ref. [14]. In this case, it is optimal to separate the scraper by $\pi/2$ betatron phase advance to minimize the maximum passable action. However, measurements with the Allison scanner showed the situation to be more complicated due to the phase-dependent branches. For illustration, Fig. 2.17 compares phase portraits recorded when removing beam with a single scraper at different locations. For this study the top scraper was moved into the beam at each of the stations, one at a time, to intercept 10% of the current (0.5 mA) based on the measured current at the beam dump. In Fig. 2.17 phase portraits with (red) and without (blue) scraping are overlapped in x-x' (left) and $J - \phi$ (right) coordinates. The action and phase of the scraped beams are calculated using the beam centroid and the central Twiss parameters of the non-scraped beam to maintain the same definition of action

for direct comparisons.

Figure 2.17 shows that scraping the same fraction of the beam current by different scrapers results in different decrease of the tails due to a strong dependence of the tail intensity on phase. For example, inserting the scraper M71 (Fig. 2.17(d)) removes primarily the tail particles, while the scraper just upstream, M61 (Fig. 2.17(c)) misses a significant portion of the branches and does not reduce the maximum action of the beam. Instead, in order to remove 10% of the current, the scraper removes particles with lower action. Therefore, in order to achieve maximal tail reduction for a given reduction of the output beam current, the beam phasing at the scrapers could be optimized by adjusting the optics and/or scraper locations such that the phases of the branches are at 0 or π at the scrapers. Alternatively, if such changes to the optics are not possible, scrapers that are not expected to intercept the tails can be positioned to remove less of the total beam current.

Visually, Fig. 2.17 hints that for the upstream scrapers propagation through the beam line smears the scraping boundary beyond of what is expected from the finite width of the scanner slits. This could be related to non-linear space-charge fields, as expected from preliminary simulations in Ref. [14]. In attempting to make a numerical estimation of this effect, one can propagate the scraper footprint using the transfer matrix and calculate the portion of the particles beyond the cut line in the recorded portrait. A scraper with vertical offset d from the beam center produces a line in the Allison scanner portrait

$$y_1'(y) = \frac{y}{\beta_1}\left(\cot(\Delta\phi) - \alpha_1\right) - \frac{d}{\sqrt{\beta_0\beta_1}\sin(\Delta\phi)} \tag{2.30}$$

where subscripts 0 and 1 denote the locations of the scraper and Allison scanner, correspondingly, $\Delta\phi$ is the vertical betatron phase advance between them, and α and β are the Twiss

parameters. The center of the coordinate system is placed at the center of the distribution. The rms Twiss parameters at the scanner are measured directly; the offset and the rms beam size and, assuming a constant emittance, β_0 can be reconstructed from the corresponding scraper scan. The phase advance, however, needs to be delivered by the optics model. The rms parameters, simulated by TraceWin [15], are found in a good agreement with the envelope measurements performed with scrapers [16], and the phase advances are calculated using the rms beam sizes and emittances delivered by the program. The scraper footprints drawn according to Eq. 2.30 are shown on all plots of Fig. 2.17 with solid lines. These lines were expected to approximately coincide with the scraped edge of the beam distribution. Unfortunately, this visually is not the case, and numerical estimations of the particles' diffusion over the scraper footprints cannot be made. A possible interpretation of this result is that the accuracy of prediction with the linear Courant-Snyder model with uniform phase advance for all particles becomes unsatisfactory for the case of long propagation of the tails. Simulations performed with the same initial conditions and the same magnet settings but with a zero beam current show the phase advances that are larger than at nominal 5 mA by 10 - 20% (depending on the longitudinal position). Staying within the linear model, one can visualize the tail particles advancing in the phase with the rate somewhere between zero current and nominal cases. The dashed lines in Fig. 2.17 drawn with the phase advances increased by 10% for each portrait are indeed visually closer to the scraper footprints.

This assumption of non-linear optics is supported by an increasing phase shift of the second harmonic as a function of action throughout the MEBT. The second harmonic was calculated by taking the Fourier transform with respect to phase in action bins ΔJ=0.05 mm mrad wide. This was done for measurements at each of the three locations of the Allison scanner and the phases were shifted by a constant for easier comparison (Fig. 2.18). At location 1,

the phase is mostly constant with action. At location two, the phase starts to decrease at lower actions and this behavior becomes larger at location three. The shift in the second harmonic is approximately proportional to the amplitude of the 0^{th} harmonic in all locations. This effect can be interpreted as the tails have a different phase advance as the core resulting in the beam becoming 'S' shaped.

This increasing 'S' shape can explain that despite having the same ϵ_c and fraction in the core, the distribution at location 3 extends to higher action compared to location 2. The tail particles are shifting away from the primary axis of the ellipse encompassing the core. This would cause the tails to move to higher actions without the central distribution or the total population of tail particles changing.

2.3 Future measurements

This method of analyzing the phase portraits using action-phase coordinates is feasible and can lead to better measurements and removal of beam tails. Unfortunately with the measurements in the PIP2IT MEBT, the electron noise and beam jitter confounded the measurements making definitive claims of beam growth challenging. While the measurements presented above are sufficient to show that this method is practical, to further this method, it would be beneficial to use cleaner measurements.

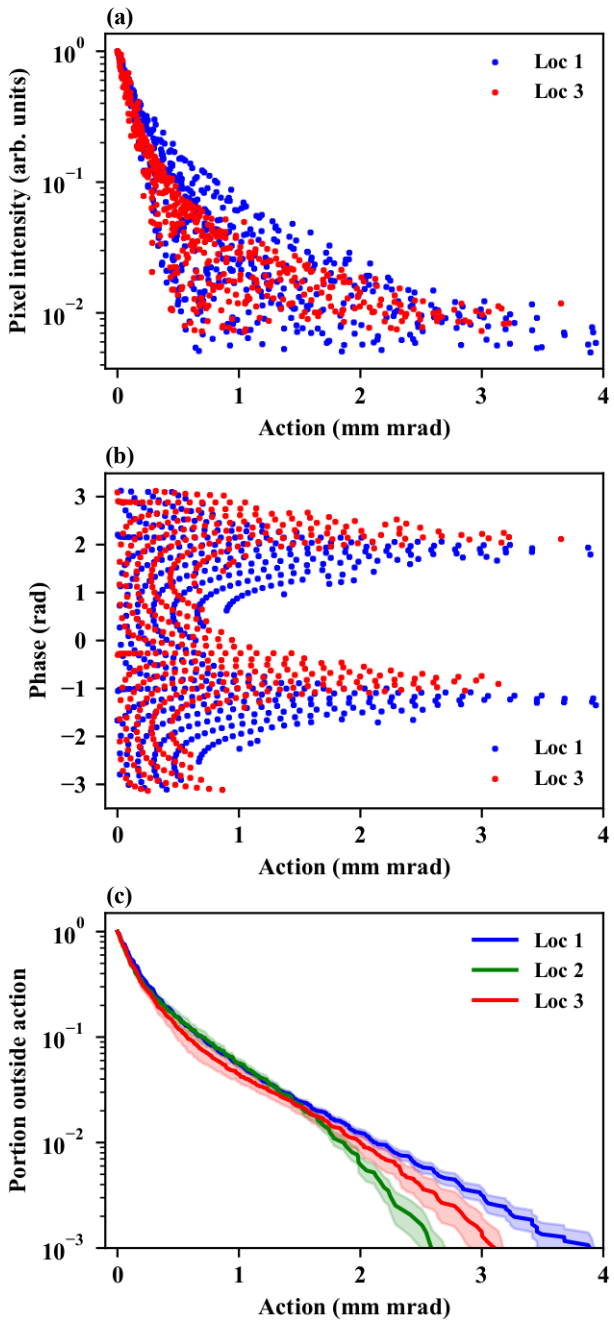

Figure 2.15: Comparison of the amplitude versus action distribution (a) and the phase portraits in action-phase phase space (b) at the beginning and end of the MEBT. The extent of the far tails is shown in (c). The shaded areas represent the rms errors calculated by propagation of the pixel amplitude fluctuations.

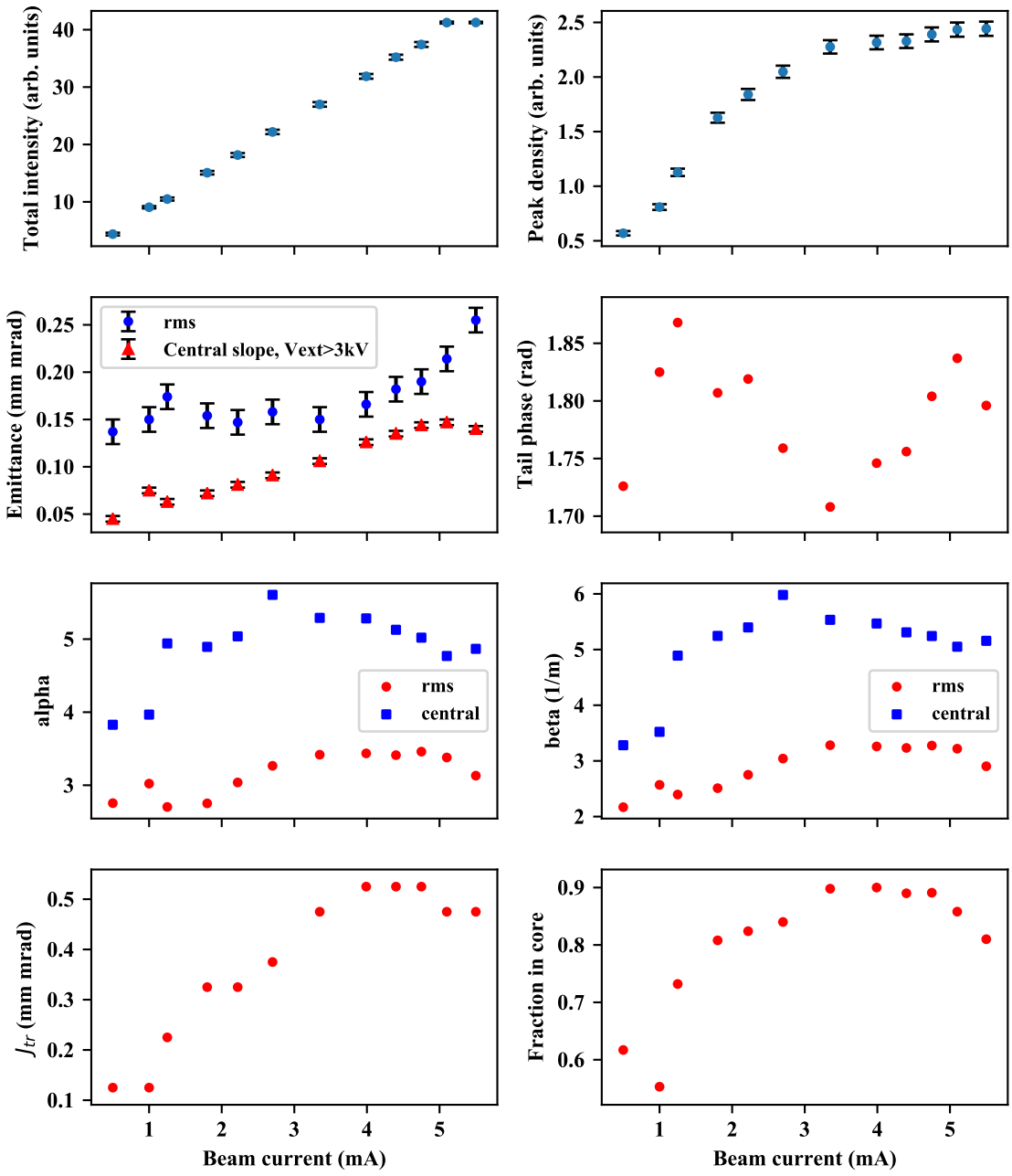

Figure 2.16: The total beam intensity (a), peak pixel amplitude (b), emittance (c), and Twiss parameters (d) for different extraction voltages V_{extr}. Parameters are plotted as functions of the beam current in the LEBT.

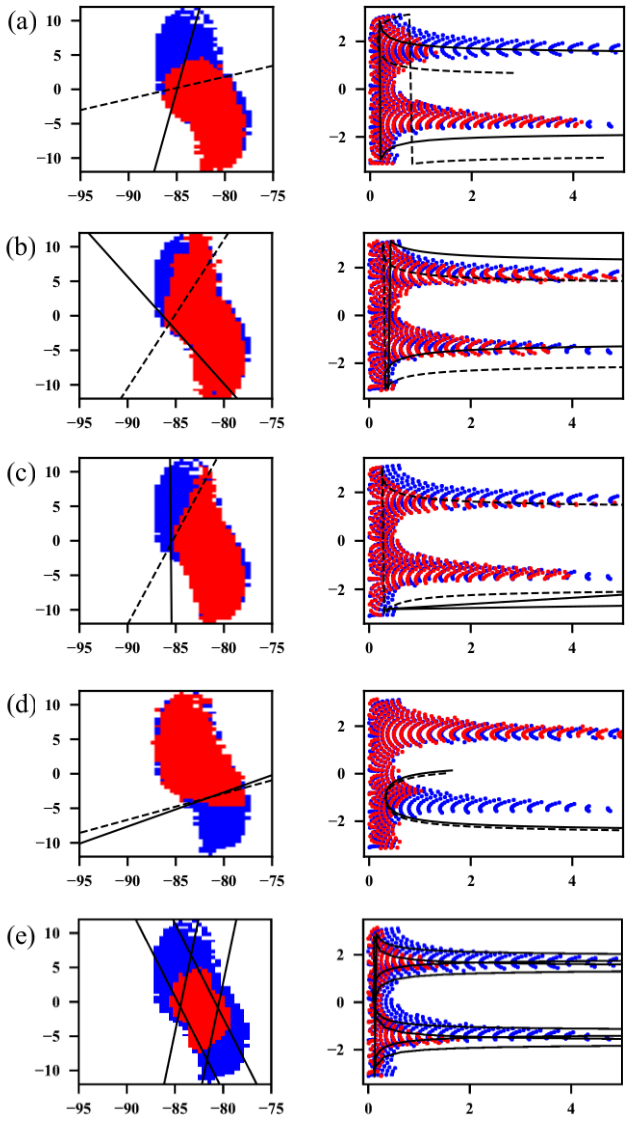

Figure 2.17: Phase portraits with scraping. Rows (a) - (d) correspond to moving into the beam one of the scrapers along the beam line presented in Fig. 2.3; from top to bottom M00, M11, M61, M71. In each case, 0.5 mA is intercepted out of the initial 5 mA. The row (e) represents the 'flat' beam when top and bottom scrapers are inserted in M00 and M11 stations. The solid lines represent the attempt of propagating the scrape lines according to 5 mA beam simulations. The dashed lines represent propagation with the phase advance increased by 10%. See other details in the text.

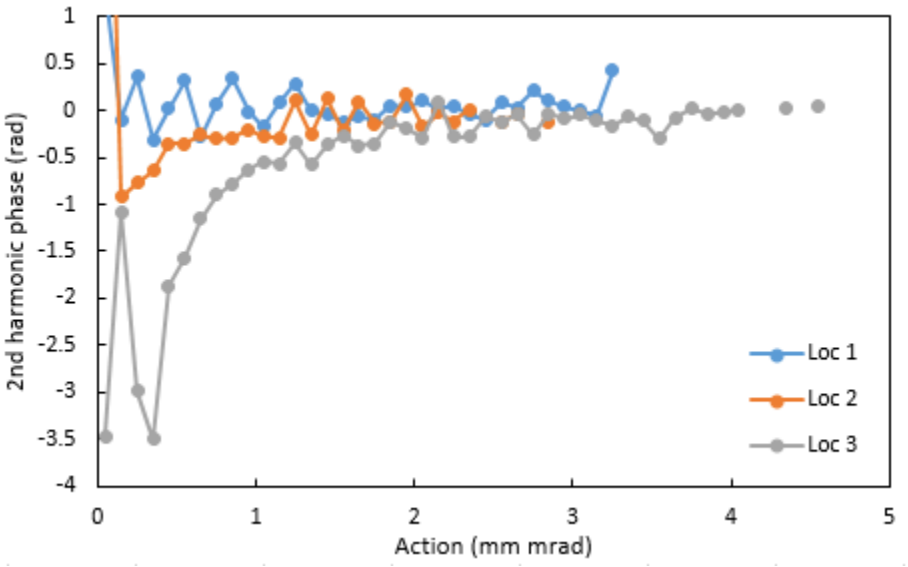

Figure 2.18: Phase of the second harmonic as a function of action for the three measured locations.

Chapter 3

Beam parameter measurements using BPMs

Measurements of the phase space distribution are useful to fully characterize the beam. However, they can typically only be used in low energy regions of the beam line because they rely on the lower rigidity of beam. In addition, because these devices intercept the beam, they must be able to withstand the deposited beam power which becomes more challenging at higher energies. In addition, because they are inserted into the beamline, the phase space measurements cannot be performed during operation.

On the other hand, beam position monitors (BPMs) are non-intercepting devices that are used throughout the entirety of accelerators but they only measure first order moments. They are one of the primary tools to verify the beam dynamics and tune of the beamline. Standard analysis of the BPM signals only gives the first order moments of the beam. If the analysis can be expanded to give more information about the beam distribution, it would be highly beneficial to operation of particle accelerators.

3.1 BPM signals

3.1.1 Beam position monitoring

BPMs in hadron linacs commonly use capacitive pickups that couple to the electric field generated by the beam. These have four pickups located at the top, bottom, left, and right sides of the beam pipe. To measure the beam position, the image charge generated by the electric field from the beam on each of the pickups is measured. The radial electric field at (r, ϕ) from a pencil beam at $(x_0, y_0) = (r_0, \phi_0)$ in a pipe of radius R_p traveling at $v = \beta c$ and charge modulated with frequency ω is given by [17]

$$\begin{aligned} E_r(r,\phi) =& D_\omega \cos\left(\omega\left[t + \frac{z_0 - z}{\beta c}\right]\right) \sum_{n=0} \frac{g I_n(g r_0)}{\epsilon_0 N \pi I_n(g R_p)} \cos(n[\phi - \phi_0]) \times \\ & \left[I_n'(gr) K_n(g R_p) - I_n(g R_p) K_n'(gr)\right] \end{aligned} \tag{3.1}$$

where I_n and K_n are the modified Bessel functions of the first and second kind, primes denote derivatives with respect to the argument, and

$$N = \begin{cases} 2, \text{ n=0} \\ 1, \text{ else} \end{cases} \tag{3.2}$$

$$g = \frac{\omega}{\gamma \beta c}. \tag{3.3}$$

The image charge at a point on the beam pipe is

$$\sigma = -D_\omega \cos\left(\omega\left[t + \frac{z_0 - z}{\beta c}\right]\right) \sum_{n=0} \frac{I_n(g r_0)}{N \pi R_p I_n(g R_p)} \cos(n[\phi - \phi_0]) \tag{3.4}$$

The signals are measured at two locations on opposite sides of the beam pipe $\phi = \phi_m$ and $\phi = \phi_m + \pi$. The difference of these two signals divided by the sum is

$$\frac{\Delta}{\Sigma} = \frac{\sum_n \frac{I_n(gr_0)}{NI_n(gR_p)} \left(\cos(n[\phi_m - \phi_0]) - \cos(n[\phi_m + \pi - \phi_0])\right)}{\sum_n \frac{I_n(gr_0)}{NI_n(gR_p)} \left(\cos(n[\phi_m - \phi_0]) + \cos(n[\phi_m + \pi - \phi_0])\right)}. \tag{3.5}$$

Taking terms linear in r_0

$$\frac{\Delta}{\Sigma} \approx \frac{2\frac{I_1(gr_0)}{I_1(gR_p)} \cos(\phi_m - \phi_0)}{\frac{I_0(gr_0)}{I_0(gR_p)}} \tag{3.6}$$

$$\frac{\Delta}{\Sigma} \approx \frac{gI_0(gR_p)}{I_1(gR_p)} r_0 \cos(\phi_m - \phi_0) \tag{3.7}$$

$$\frac{\Delta}{\Sigma} \approx \frac{gI_0(gR_p)}{I_1(gR_p)} \left[x_0 \cos(\phi_m) + y_0 \sin(\phi_m)\right]. \tag{3.8}$$

Therefore the position of the beam can be determined using the Δ/Σ signal from a horizontal pair of pickups to measure x_0 and a vertical pair to measure y_0. However, for large enough g the result is dependent on the measured frequency and beam velocity and therefore multiple calibrations must be used to correctly measure the beam position as the beam accelerates and β increases. If $g \ll 1$, corresponding to relativistic beams, then Eq. 3.8 becomes frequency independent

$$\frac{\Delta}{\Sigma} \approx \frac{2}{R_p} \left[x_0 \cos(\phi_m) + y_0 \sin(\phi_m)\right]. \tag{3.9}$$

The low β effects are most important in the front ends of hadron machines where the beam is traveling non-relativistically [18]. For example, at FRIB, with f=161 MHz and $R_p \approx$20 mm, these effects become negligible around $\beta \approx 0.07$ [19].

The linear response of Eqs. 3.8 and 3.9 hold for small beam offsets from the center of the BPM. When the beam is further away, the Δ/Σ signals vary non-linearly with beam

position. These non-linearities are mapped on a test stand, described in the proceeding chapter, and a higher order polynomial is used to calculate the beam position **??**.

Equation 3.4, holds for a infinitesimally small beam transversely with charge modulated longitudinally at a single frequency. While, this is clearly a significant abstraction from an actual beam, it is an adequate model in most cases of the BPM signals and widely used. The single frequency model is acceptable because BPM signal processing typically relies on narrowband filtering to only measure a single harmonic of the bunch repetition rate to reduce noise. In addition, at higher beam energies, the Δ/Σ signals are frequency independent. The pencil beam is an acceptable model of the transverse distribution if the beam is small compared the pipe radius.

When the beam size is larger, the signals measured by the pickups can be modeled by summing over a collection of pencil beams to generate the transverse profile. The components of this discretized model far from the center will be affected by the non-linearities in the pickups' response and cause the measured position to be distorted **??**. This distortion is dependent on the exact transverse distribution making it challenging to model. Because this effect is due solely to non-linearities caused by the geometry of the BPM, it is independent of the beam velocity.

This is effect is typically on the order of a few percent variation and typically is not considered when determining the beam position. For example, consider a Gaussian beam with $\sigma_y = 2$ mm located at x_0=2 mm and y_0=1.0 mm in a pipe of radius $R_p = 23.5$ mm. When σ_x is varied from 1 mm to 5 mm, the resulting Δ/Σ, and therefore position measurement, varies by 2-3% (Fig. 3.1). While the beam offset is larger than idea, these parameters are representative of a beam in the FRIB MEBT.

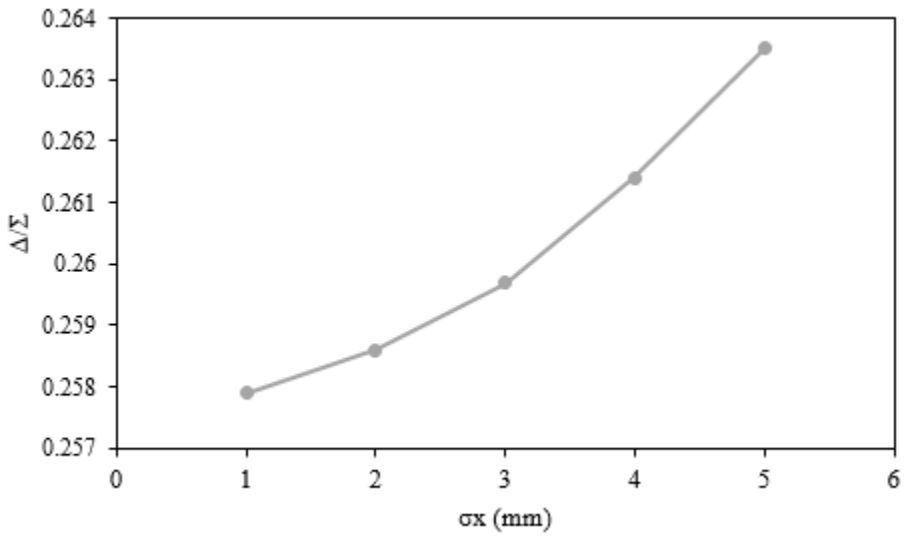

Figure 3.1: Variation of Δ/Σ when changing σ_x of a Gaussian beam centered at x_0=2 mm and y_0=1 mm for a 47 mmm aperture BPM with 20 mm diameter button pickups.

3.1.2 Bunch profile dependence

While this infinitesimally thin, single frequency model of a beam is generally adequate for position measurements, in reality the signals from BPM pickups also contain information of the transverse and longitudinal beam profiles. The longitudinal profile is contained in D_ω which is the Fourier amplitude of the longitudinal profile at the measured frequency. Therefore, it is possible, using beamline models and careful calibration, to measure the longitudinal size of the bunch by varying the optics and measuring changes in the amplitude of a signal harmonic [20].

The dependence of the pickup signals on the transverse distribution is more complex. Equation 3.4 for a pencil beam must be integrated over the transverse distribution $T(r,\phi)$

$$\sigma_{\text{wall}}(\omega, z_m, \phi_m) = D_\omega \cos\left(\omega\left[t + \frac{z_0 - z}{\beta c}\right]\right) \times \iint r dr d\phi \sum_{n=0} \frac{I_n(gr/R_p)}{\pi N I_n(gR_p)} \cos[n(\phi_m - \phi)] T(r,\phi). \tag{3.10}$$

This effect is strongly tied to the beam position and requires measurements of multiple harmonics of the beam repetition rate to be resolved.

However, when multiple frequencies are measured, the geometry of the pick ups must be taken into account. The pickups have some finite size causing their measured signal to be the integrated image charge over the button geometry

$$\sigma_{\text{pickup}}(\omega) = \int_{\text{button}} \sigma_{\text{wall}} \, \mathrm{d}A_{\text{but}}. \tag{3.11}$$

For a round button pickups, which are used at FRIB, of radius R_b this becomes

$$\sigma_{\text{pickup}}(\omega) = \int_{-R_b}^{R_b} \mathrm{d}z \int_{-\frac{1}{R_p}\sqrt{R_b^2-z^2}}^{\frac{1}{R_p}\sqrt{R_b^2-z^2}} R_p \, \mathrm{d}\phi_m \sigma_{\text{wall}}. \tag{3.12}$$

For simplicity all terms independent of z and ϕ_m will be put into a single coefficient F and $\phi \mapsto \phi + \phi_p$ to accommodate any azimuthal pickup location ϕ_p

$$\begin{aligned}
\sigma_{\text{meas}}(\omega) = \int_{-R_b}^{R_b} \mathrm{d}z_m \int_{-\frac{1}{R_p}\sqrt{R_b^2-z^2}}^{\frac{1}{R_p}\sqrt{R_b^2-z^2}} R_p \, \mathrm{d}\phi_m \iint r \mathrm{d}r\mathrm{d}\phi \times \\
\sum_{n=0} F \cos[n(\phi_m - \phi_p - \phi)] \cos\left[\frac{\omega}{\beta c}(z_m - z_0)\right] \qquad (3.13) \\
\sigma_{\text{meas}}(\omega) = \iint r \mathrm{d}r\mathrm{d}\phi \sum_{n=0} F R_p \frac{2}{n} \cos[n(\phi_p + \phi)] \times \\
\int_{-R_b}^{R_b} \mathrm{d}z_m \cos\left[\frac{\omega}{\beta c}(z_m - z_0)\right] \sin\left[\frac{n}{R_p}\sqrt{R_b^2 - z^2}\right] \qquad (3.14) \\
\sigma_{\text{meas}}(\omega) \equiv \iint r \mathrm{d}r\mathrm{d}\phi \sum_{n=0} F R_p \cos[n(\phi_p + \phi)] \cdot P(\omega) \qquad (3.15)
\end{aligned}$$

where

$$P(\omega) = \frac{2}{n} \int_{-R_b}^{R_b} \mathrm{d}z_m \cos\left[\frac{\omega}{\beta c}(z_m - z_0)\right] \sin\left[\frac{n}{R_p}\sqrt{R_b^2 - z^2}\right] \tag{3.16}$$

is the transit time factor for a round button pickup. Therefore the correction for the button shape can be separated from the effects of the beam distribution.

This derivation approximates the pickup geometry as flush with the round pipe wall. In practice, flat button pickups are commonly used because they are simple to manufacture. Show in Fig. 3.2 is the inside of a BPM used at FRIB where flat, 20 mm diameter pickups are used and they are recessed 1 mm from the pipe. This difference in geometry needs to be accounted for when the measured wavelength is on the same order as the pickup size. For the 20 mm diameter pickups used at FRIB, the frequency needs to be above ∼0.5 GHz for a beam traveling at $\beta = 0.033$ corresponding to the beam energy after the RFQ. This estimate is confirmed by CST Microwave Studio [21] simulations of the two BPM geometries at this velocity which show the difference becomes significant at ∼400 MHz (Fig. 3.3). To limit the effect of the curved approximation, the broadband measurements presented below with the FRIB BPMs were limited to 400 MHz.

3.1.3 Pickup signal variation with transverse distribution

As discussed above, the position measurement is dependent on g for large g, i.e non-relativistic beams. This is due to the profile of the electric field on the pipe wall generated by a non-relativistic beam extending beyond the length of the beam and the fields profiles are different on each pickup and vary with beam position. As the beam increases in energy, relativistic effects 'pancake' the field distribution into the plane perpendicular to the beam velocity (Fig. 3.4) and the longitudinal profile of the fields becomes similar to the beam profile. At these higher energies, varying the beam position causes little change in the field profiles on the wall and only changes the amplitude resulting in no frequency dependence in position measurements.

Figure 3.2: Geometry of FRIB BPMS.

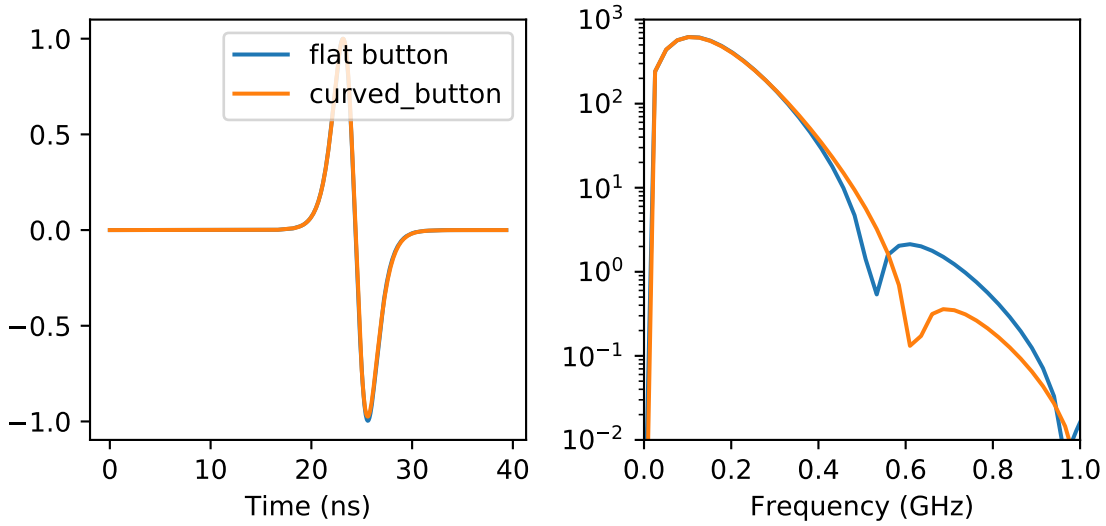

Figure 3.3: Signal on a flat and curved 20 mm diameter BPM pickup from a β=0.033 beam. The two geometries give similar results up to ∼400 MHz.

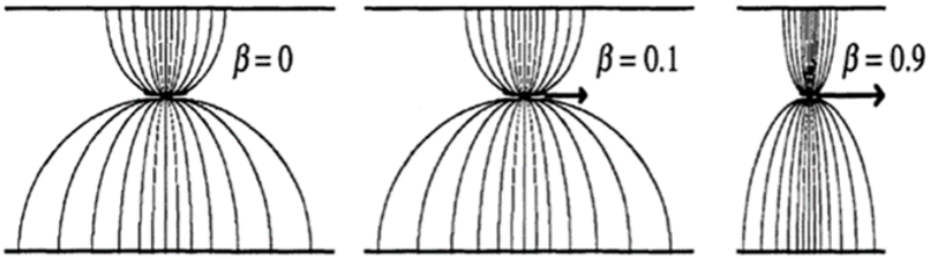

Figure 3.4: As the beam accelerates the electric field is compressed into to the plane perpendicular to the velocity resulting in the same field profile on opposite sides of the beam pipe.

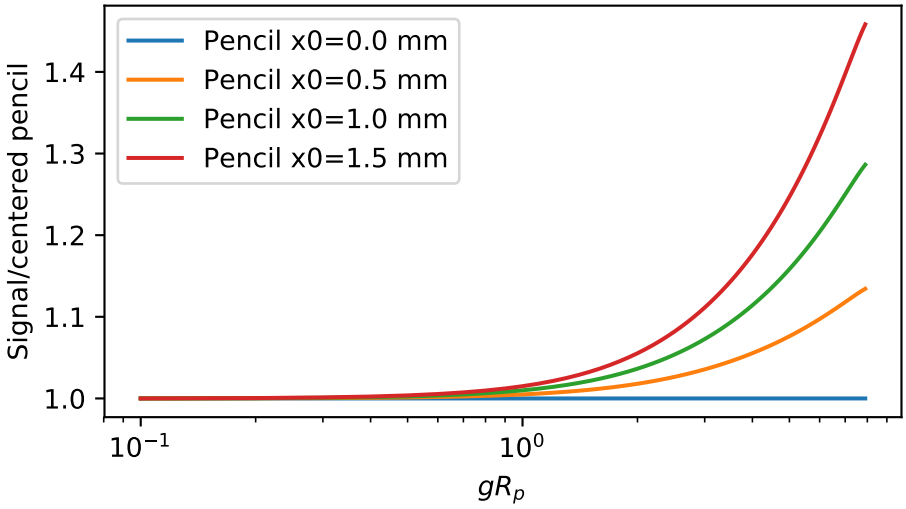

Figure 3.5: Variation in the measured spectra on a 20 mm diameter pickup for an offset pencil beam. The spectra are normalized to the centered case.

This variation of the field profile can be seen on the measured spectra from various offsets of a pencil beam (Fig. 3.5). Because for non-relativistic beams, the signals on the pickups vary with ω and β, they are best characterized in terms of gR_p with higher g corresponds to higher frequency and lower β. The effect of offsetting the beam is significant for $g > 1$ with variations on the order of 10s%. For $gR_p < 1$ the spectra on the buttons from an offset beam are the same as the spectra for a centered beam. For $gR_p > 1$ Eq. 3.8 must be used to correctly determine the position. For lower g Eq. 3.9 can safely be used.

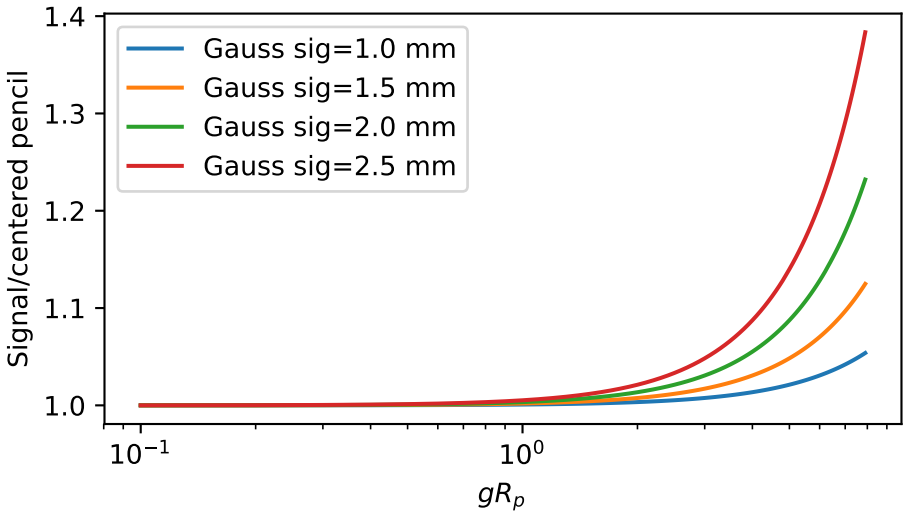

Figure 3.6: Variation in the measured spectrum for a centered round Gaussian beam of different sizes. The spectra are normalized to a centered pencil beam.

To see the effect of the transverse distribution, the amplitude of the integral in Eq. 3.10 is plotted in Fig. 3.6 as a function of gR_p and are normalized to the result a pencil beam. A Gaussian beam with $\sigma_x = \sigma_y$ was used and the transverse size was varied. Similar to offsetting the beam, the variations due to transverse beam size are significant for $gR_p > 1$. For $gR_p < 1$, the transverse size can be neglected and a pencil beam can be assumed. Similar effects are seen when varying σ_x or σ_y while leaving the other fixed.

If a BPM is operating in a region where where transverse distributions must be accounted for, it is important to use the exact distribution. It is not sufficient to use a model with the same first and second order moments. For example, consider a beam with transverse profile that is the sum of two Gaussian and a beam with a single Gaussian profile with parameters give in Table 3.1 (Fig. 3.7). At high g the measured signals vary both in amplitude and profile resulting in errors in the measured position. However, this effect is difficult to correct because it requires an accurate model of the the beam. At lower g the measured spectra become the same on all pickups and the distribution no longer needs to be taken into account.

Table 3.1: Parameters of the distributions used in Fig. 3.7.

	Amp 1	x_0 1	y_0 1	σ_x 1	σ_y 1	Amp 2	x_0 2	$_y$0 2	σ_x 2	σ_y 2
Double Gaussian	1	0 mm	1.07 mm	1.7 mm	2.49 mm					
Single Gaussian	1	0 mm	0 mm	1.7 mm	1 mm	0.4	0 mm	2 mm	1.7 mm	3 mm

This effect is solely due to the electric field distribution and is distinct from the errors caused by the transverse beam distribution due to non-linearities discussed above.

3.1.4 Button sum signal

The dependence on the pickup spectra on the transverse distribution makes measurements of the beam profiles challenging. To alleviate this sensitivity, the signals from all four buttons can be added together. By summing Eq. 3.15 over the four pickups, the summed signal is found to be

$$\sigma_{\text{sum}}(\omega) = P(\omega) \iint r\mathrm{d}r\mathrm{d}\phi \sum_{n=0} FR_p \Big(\cos[n(0+\phi)] + \cos[n(\pi/2+\phi)] + \cos[n(\pi+\phi)] + \cos[n(3\pi/2+\phi)] \Big) \tag{3.17}$$

$$\sigma_{\text{sum}}(\omega) = P(\omega) \int \mathrm{d}A_{\text{beam}} \sum_{n=0} FR_p \cdot 4\cos(n\phi) \begin{cases} 1, & n \equiv 0 \pmod 4 \\ 0, & \text{else} \end{cases} \tag{3.18}$$

For the circular button pickups used for FRIB, only azimuthal harmonics that are zero modulo four remain after summing. This significantly reduces the dependence of the signal on ϕ as well as the dependence on position and transverse distribution. In the case of rectangular pickups that cover the full 2π solid angle, only the $n = 0$ component remains and the signal is independent of ϕ.

The scalings discussed above are repeated in Fig. 3.8 using the summed signals. The dependence on beam offset for a pencil beam is reduced by a factor of $\sim$7 and the dependence

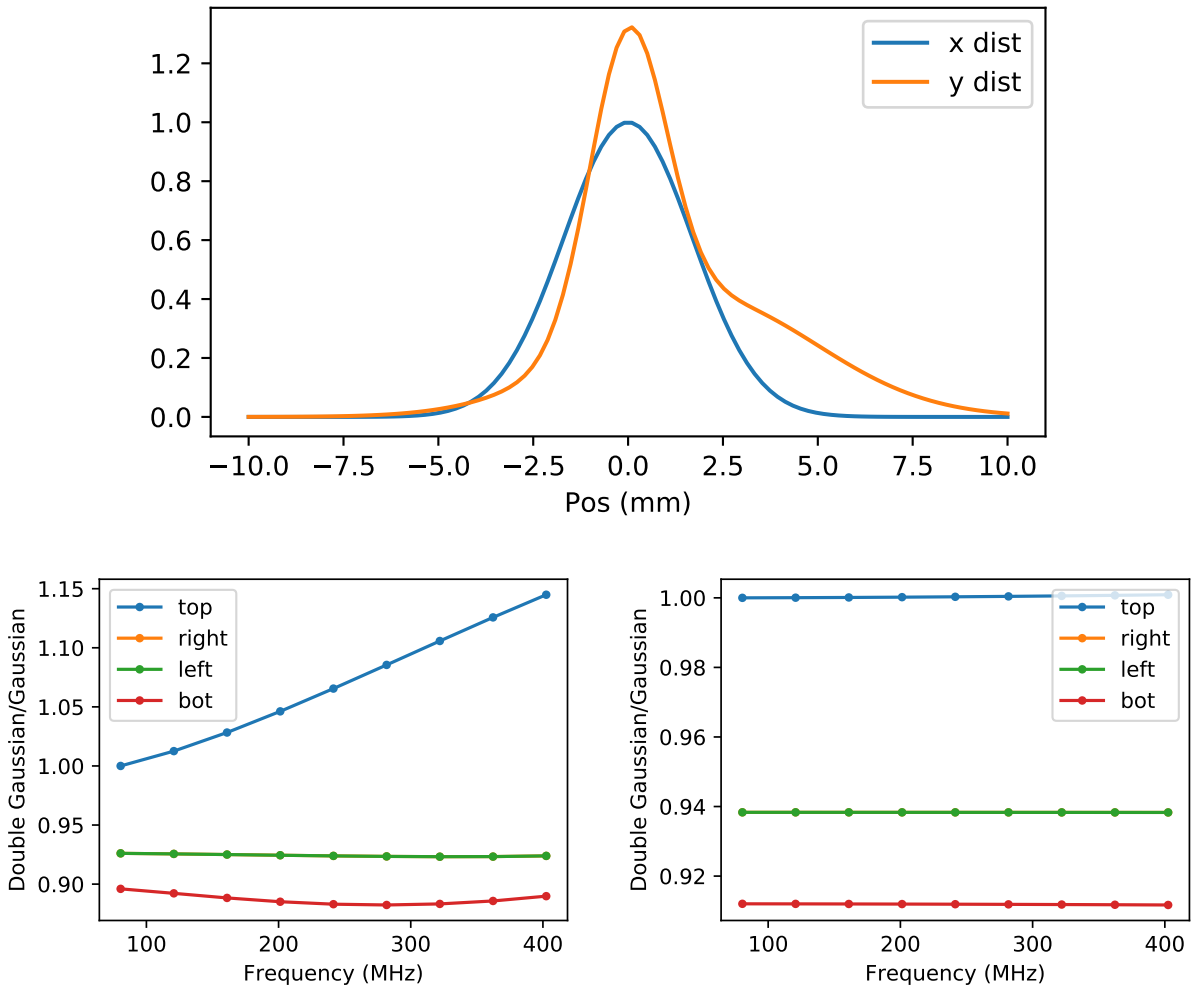

Figure 3.7: Comparison of measured spectra from a Gaussian and double Gaussian beam with the same first and second order moments with β=0.033 (left) and β=0.15 (right). At large g the different distribution results in a different measured spectra.

on the transverse size for a Gaussian beam is reduced by >20% at high g. The reduction of dependence on bunch shape is independent of the size of the beam. These reductions allow for the summed signal, the beam can be assumed to be a pencil beam at $gR_p \approx 3$ which is an improvement from the non-summed signals which require $gR_p \approx 1$ to assume a pencil beam.

However, while this method reduces the sensitivity to the transverse distribution which is beneficial for determining the longitudinal profile, at low enough β, g will be large enough that the transverse distribution still needs to be accounted for. But, due to symmetry, σ_x and σ_y cannot be distinguished from each other and the position can only be determined modulo a phase of $\pi/4$. This can result in the aggravating situation where the same number of parameters must be used to describe the beam as the non-summed case, but less information is obtained. In general, the sum signal should be be use when information of the transverse distribution is not needed and when $gR_p \in (1, 3)$.

3.1.5 CST simulations

The required correction to recover the beam parameters from the measured signals were checked using CST Microwave Studio simulations. The simulations were performed using the wakefield solver with a mono-energetic pencil beam and measure the field at the pipe wall at a single point to confirm Eq. 3.4. This eliminates corrections for the transverse size, energy spread, and the pickup geometry and impedance; with the plan to build up to more complex distributions to test Eq. 3.15. However, simulations using the wakefield solver showed a discrepancy between the field at a point on the wall in simulation results and the analytic field at the wall from a pencil beam for $\beta < 0.15$ (Fig. 3.9).

Instead, the simulation results matched the expected signals from a uniform square beam

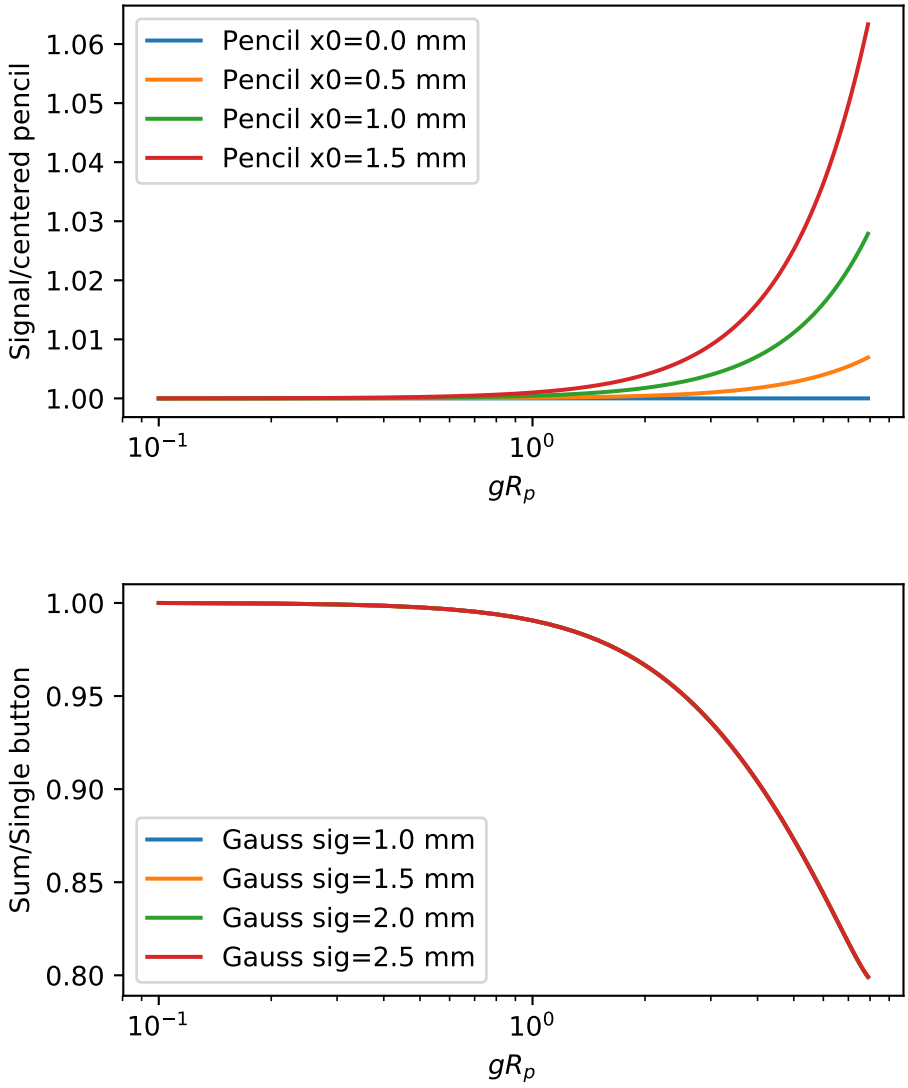

Figure 3.8: (Top) Variation of the summed signal for an offset pencil beam. The variations in the spectra are a factor of ∼7 lower than the non-summed signals. (Bottom) The summed signals of a 1 mm offset Gaussian beam normalized to the single pickup signals. The variations of the summed spectra are reduced by 20% compared to the non-summed signals.

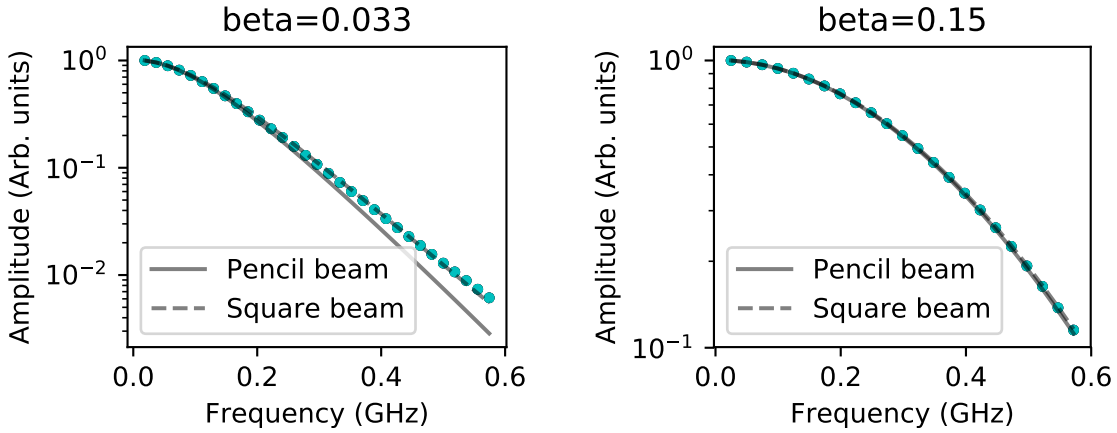

Figure 3.9: CST simulations using the wakefield solver must be fit to a uniform square beam with side length given by the mesh size. For the given frequency range, this artificial transverse distribution can be ignored for β >0.15.

with side length equal to twice the mesh cell size suggesting the discrepancy is caused by how CST handles meshing. The pencil beam used in the wavefield solver transversely lays on the intersection of four mesh cells. The solver appears to assume all cells touching the beam are part of the beam. If the analytic model uses a uniform, square transverse distribution much better agreement is achieved with simulations.

With this unwitting inclusion of a transverse distribution at low β, the wakefield solver was used for simulations including a BPM model. The model used is a simplified model consisting of flat cylindrical buttons that are connected to ground via 50 Ω discrete ports (Fig. 3.10). The impedance of these pickups was measured using $S_{2,1}$ between two pickups and fitting for the resistance and capacitance (Fig. 3.11). The measured capacitance to ground was 4.1 pF.

The BPM signals match the expected analytic signals within 5% for $\beta = 0.033$ and the difference decreased when β was increased (Fig. 3.12). From these signals, a resonance due to the button size can be seen around 500 MHz for β=0.033. This resonance is not seen in

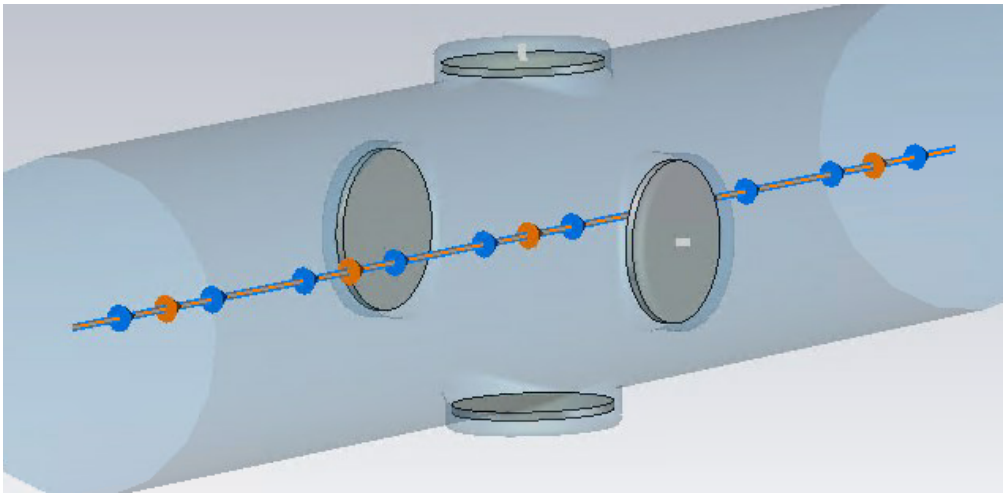

Figure 3.10: Model of the FRIB BPMS in CST Microwave Studio.

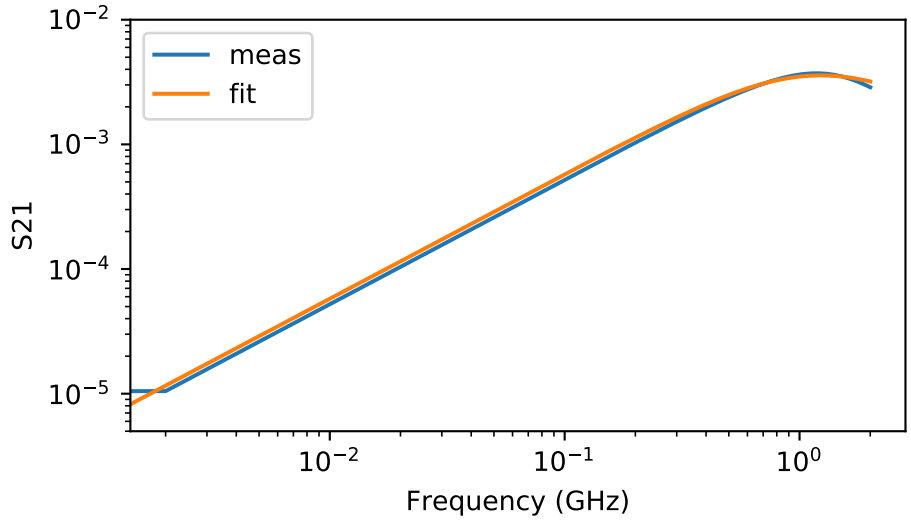

Figure 3.11: Fitting $S_{2,1}$ of a the CST button model to determine the impedance.

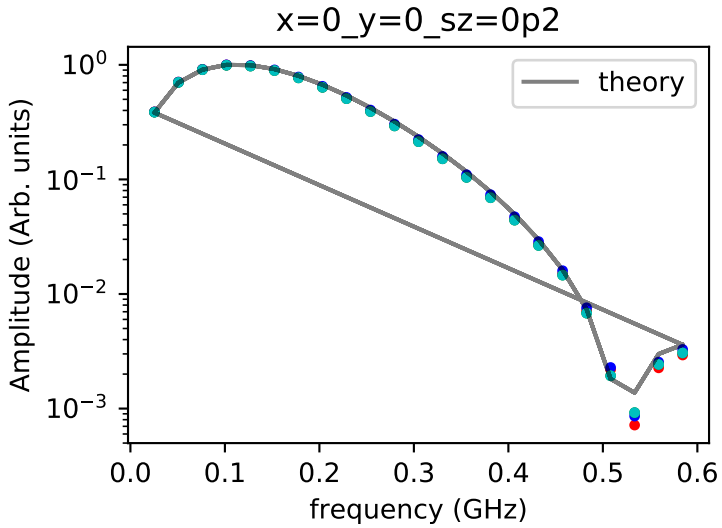

Figure 3.12: Simulation results compared to analytic results of BPM pickup signals from a centered pencil beam using the wakefield solver.

beamline measurements due to low pass filtering.

3.2 Bunch profile measurements

3.2.1 TIS waveforms

The BPM system at FRIB can measure the signals from the buttons over a wide bandwidth using a quasi-Time Interleaved Sampling (TIS) method. The beam is comprised of a series of individual bunches that are longitudinally spaced at a repetition rate of either 40.25 MHz or 80.5 MHz. The pickup signals from the bunch train are sampled by the digitizer at 119 MHz. Each sample of the digitizer occurs at a different phase with respect to the bunches (Fig. 3.13) resulting in an effective sampling rate of 2.737 GHz and can resolve harmonics of 40.25 MHz up to 1.3 GHz. However, measurements are limited to 0.5 GHz by a low-pass filter on the board. These measured signals are referred to here has the TIS waveforms.

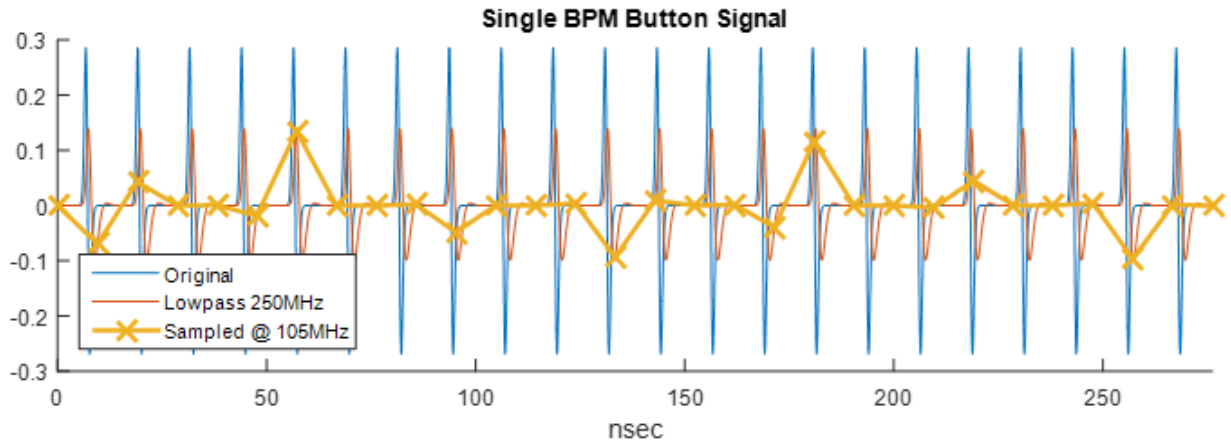

Figure 3.13: Example of the sampling procedure to measure the TIS waveforms. (Image courtesy of S. Cogan)

3.2.2 Impedance and filtering effects

The measured signals are affected by the impedance of the BPM pickup. The capacitive BPM pickup acts as a low pass filter with cut off frequency $\omega_c = 1/RC$ where R is the resistance and C is the capacitance of the pickup. The measured voltage from a button BPM is [22]

$$V_{\text{meas}}(\omega) \propto \frac{\omega/\omega_c}{\sqrt{1+(\omega/\omega_c)^2}}\sigma_{\text{pickup}}(\omega). \tag{3.19}$$

This causes the measured signals to appear like the derivative of the electric field at the wall. For FRIB C=3.3 pF and ω_c=6.06 GHz [19]. This effect is independent to the beam and is corrected for before fittings for the beam parameters.

After the signal is measured by the pickup, it, passes through a cable and lowpass filter to a digitizer. The response to this system was characterized by removing the cables from the pickups and inputting a harmonic of 80.5 MHz up to 483 MHz into the cables and recording the output of the digitizer. The Fourier transform of these signals was used to determine the transfer function for each harmonic. For this calibration, the TIS waveforms could not be recorded because that system requires the input signal to be phase locked to the 80.5 MHz

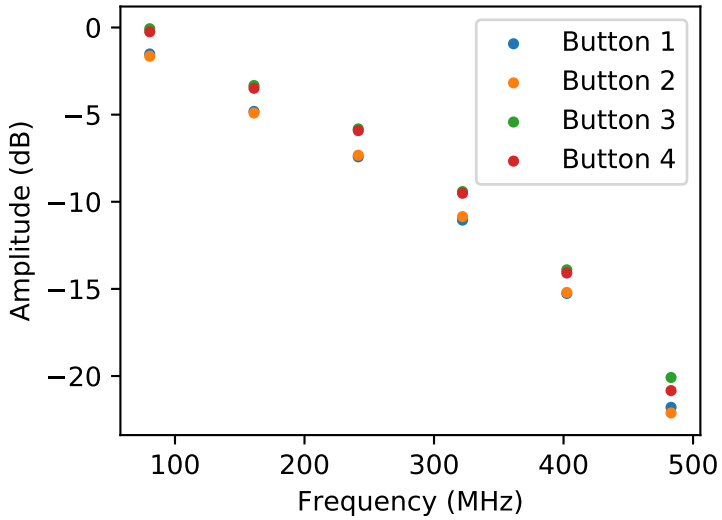

Figure 3.14: Cable and board calibration for four buttons on a BPM.

global clock while the single generator could only lock to a 5 MHz or 10 MHz clock. For any given tone, the harmonics of that tone were also seen. The first higher harmonic at twice the input frequency was at least three orders of magnitude lower than the primary tone and ignored in the analysis. This calibration is stable within ±10% for tested BPMs.

The calibration of one of the BPMs is shown in Fig. 3.14. Note that two of the buttons are $\sim$ 1.5 dB lower than the other two. For these buttons, the signal processing board includes a switch for injecting signals which causes the reduction. All BPMs have these switches for two of the buttons and these must be correctly accounted for.

Only harmonics of 80.5 MHz were calibrated because, at the time the calibration was performed, the TIS waveforms could only measure harmonics of 80.5 MHz. The software was later updated to measure harmonics of 40.25 MHz. The uncalibrated 40.25 MHz harmonics, except for 40.25 MHz, are corrected using a cubic spline interpolation of the 80.5 MHz harmonics measurements. These calibrations were also only performed for nine BPM near the RFQ including all four BPMs in the MEBT. For all other BPMs, the signals are corrected

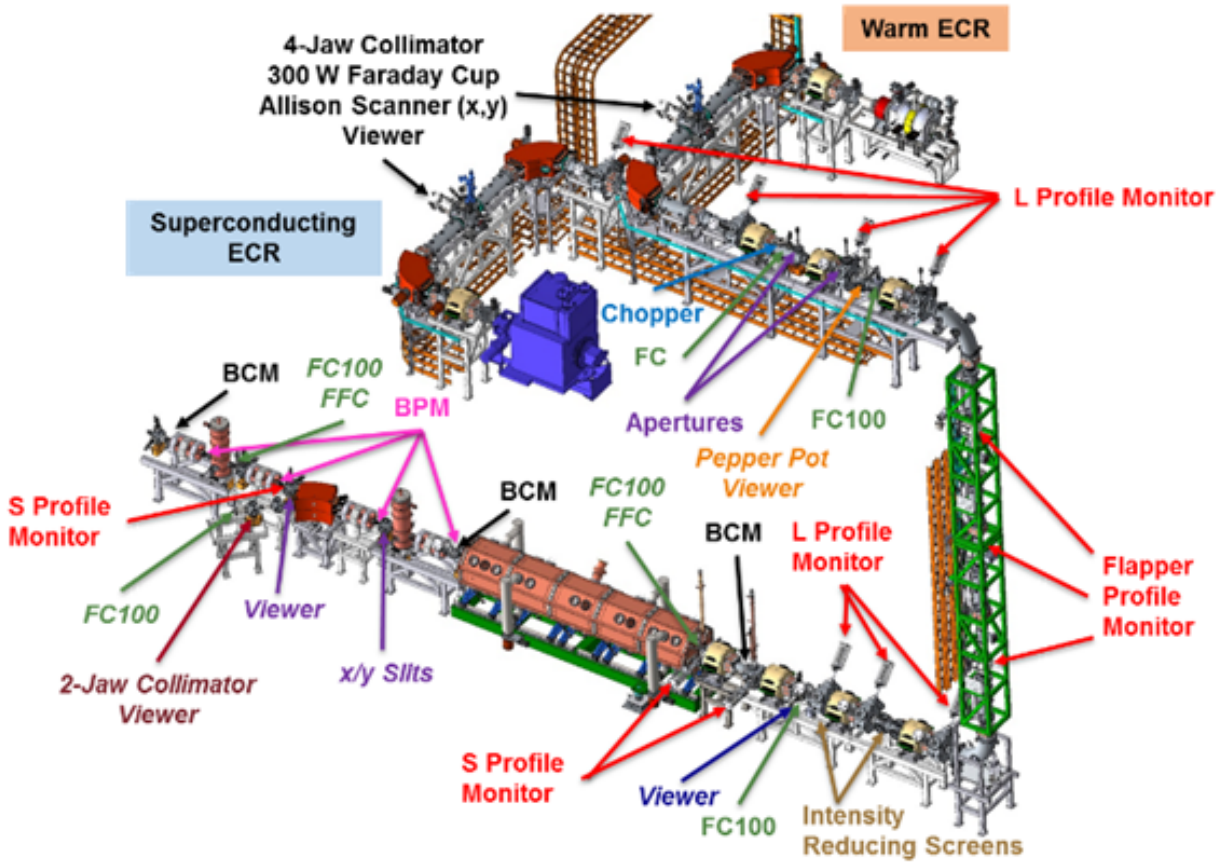

Figure 3.15: Overview of the diagnostics in the FRIB front end. The MEBT is shown in the lower left and contains the four BPMs.

using an average of these measurements.

3.2.3 Beamline measurements

Measurements of the BPM buttons signals were taken in the FRIB MEBT (Fig. 3.15). In this region the beam velocity is $\beta = 0.033$. The TIS waveforms were recorded for all four BPM in the MEBT which have a 47 mm diameter aperture and 4, 20 mm diameter buttons. However, most measurements of interest were taken with the third BPM because there is a wire profile monitor directly upstream of it and it is sufficiently downstream of a buncher cavity to change the bunch length.

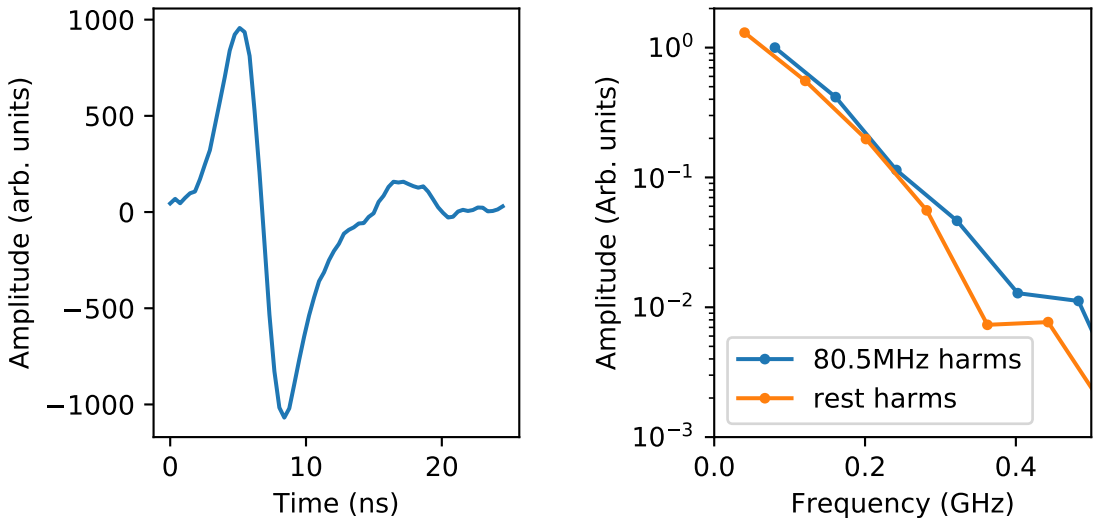

Figure 3.16: Example of a measured TIS waveform in the FRIB MEBT (left). The bump at 15 ns is a partially filled RF bucket. This causes the harmonics of 80.5 MHz to be higher than the rest of the harmonic of 40.25 MHz (right).

The TIS waveform were taken to measure harmonics of 40.25 MHz, however the RF frequency of FRIB is 80.5 MHz. This is possible because in single charge state operation, a prebuncher before the RFQ causes the bunches coming out of the RFQ only fill every other bucket. However, a small signal was seen in the bucket that was supposed to be empty. This causes the even harmonics of 40.25 MHz, i.e. the harmonics of 80.5 MHz, to be slightly higher than the odd harmonics (Fig. 3.16). The beamline was also operated without the prebuncher, in this case all RF buckets were filled and only the harmonics of 80.5 MHz are non-zero.

The raw signals are corrected for the impedance and board effects (Fig. 3.17) then fit to Eq. 3.15 assuming the beam is Gaussian transversely and longitudinally with fit parameters $x0$, $y0$, σ_x, σ_y, σ_{xy}, σ_z, an amplitude, and an offset to account for noise. Because the amplitude of each button depends on the transverse size and offset, all four button spectra must be fit simultaneously. The measured spectra in the MEBT fit well to Eq. 3.15 with

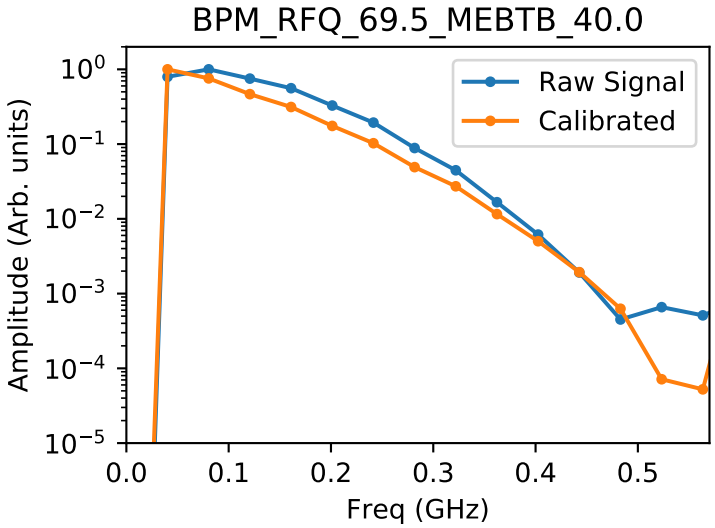

Figure 3.17: Raw and calibrated spectra of a BPM in the MEBT

differences primarily due to the discrepancy between the even and odd harmonics (Fig. 3.18).

Measurements were taken with the third BPM in the MEBT for a range of voltages of the upstream buncher cavity with it set to a bunching phase to change the bunch length at the BPM. Along with the TIS waveforms, the transverse profiles were recorded with the wire profile scanner. The Fast Faraday Cup (FFC) could not be used to verify the longitudinal profile for most measurements because a Faraday cup at the same location needed to be inserted to act as a beam stop. Instead, simulations were used to compare the expected longitudinal size to the BPM measurements (Fig. 3.19). While the BPM measurements give longitudinal and transverse sizes on the same order as the simulation results, the longitudinal measurements fail to follow the expected trend from changing the buncher voltage.

Separate measurements were taken with the FFC for the same range of buncher voltages and they follow the expected trend of going through a minima. In addition the FFC measurements confirm that the longitudinal beam profile is primarily Gaussian.

The abnormal behavior of the BPM measurements is believed to be cased by the trans-

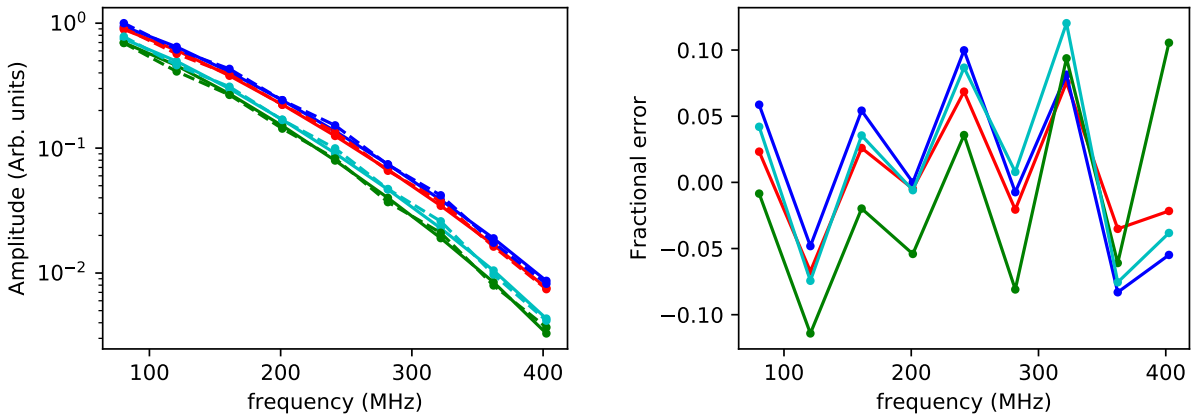

Figure 3.18: Fitting the measured spectra and fractional error from the measured values.

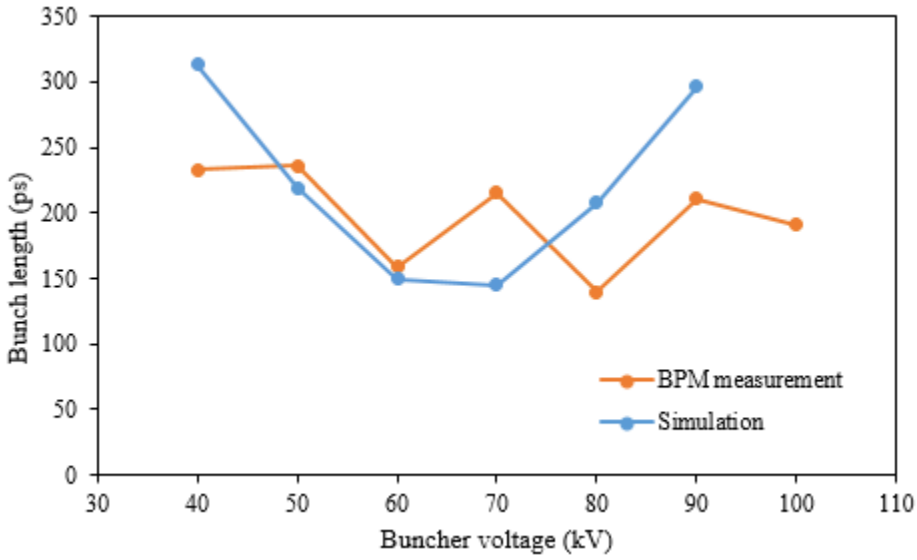

Figure 3.19: Comparison of the measured bunch length with simulations at the third BPM in the MEBT when the buncher cavity voltage is varied. The BPM measurement fails to produced to expected trend.

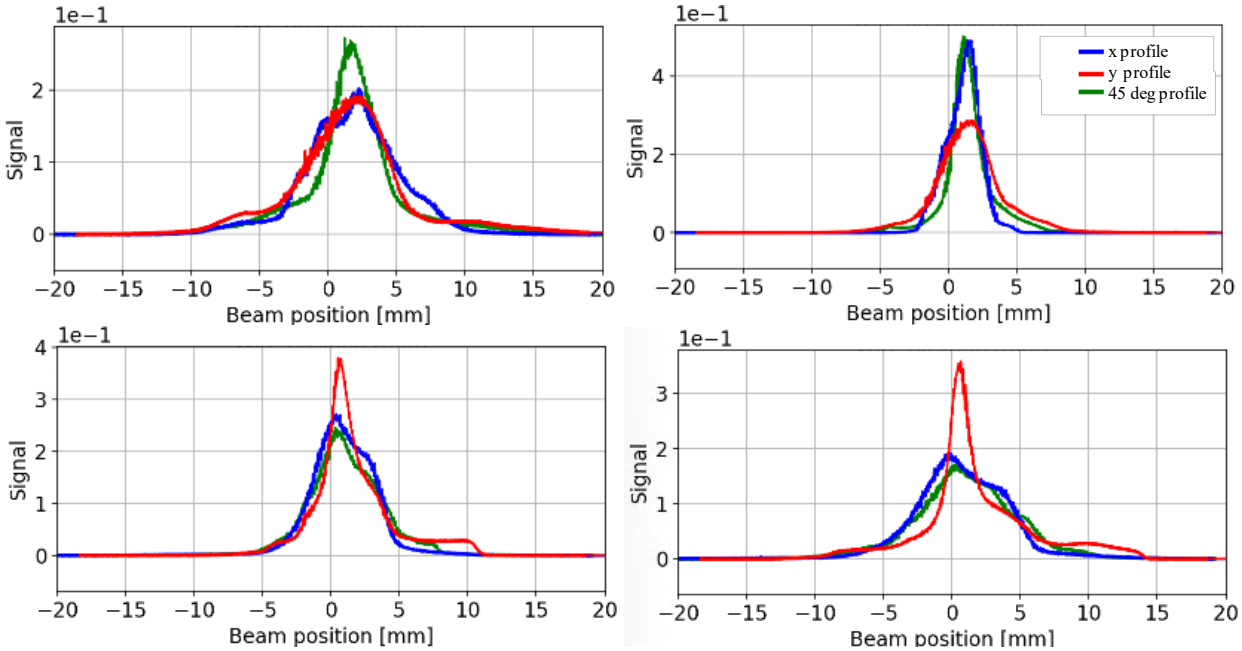

Figure 3.20: Transverse profile measurement in the MEBT.

verse distribution of the beam. Measurements of the transverse profile with the wire scanner clearly show clearly non-Gaussian profiles, especially in the vertical plane, while the BPM measurements assume Gaussian (Fig. 3.20). For the TIS waveforms in the MEBT, gR_p ranges from 1.2 to 6.0 and in this range the effect of using the incorrect distribution will be significant even for the summed signal. Varying an upstream quadrupole to change the transverse distribution at the third BPM in the MEBT resulted in a variety of measured transverse profiles at the BPM. Because of this, a better model of the beam was not developed. It is possible to input the measured profiles into Eq. 3.15 in order to fit the longitudinal profile. However, this procedure cannot be generally applied to the other BPM because there are no measurements of the beam distribution at these locations.

In an attempt to remove the transverse effects, the spectra were measured with BPMs at the end of the first accelerating linac segement of FRIB where the beam is traveling at $\beta = 0.185$ corresponding to a maximum gR_p of 1.07. This is low enough to ignore the

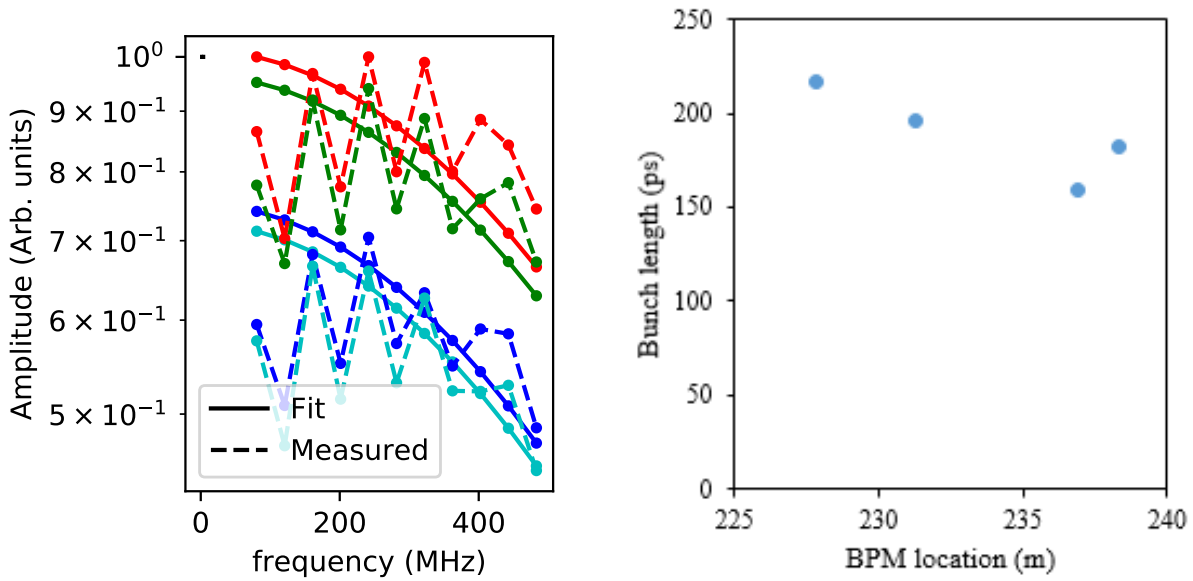

Figure 3.21: Spectra and fitting a pencil beam to measurements at $\beta = 0.185$. The droop at low frequency is hypothesized to be caused by incorrectly modeling the pickup impedance.

transverse distribution and assume a pencil beam. These measurements were taken with four BPMs and, based on simulations, the beam length should be linearly increasing across the four locations. The BPM measurements,once again, fail to reproduce the expected trend (Fig. 3.21 right).

The measured spectra, after corrections for the impedance and cable and board effects, retained a droop at low frequency (Fig. 3.21 left). The longitudinal profile was measured to be primarily Gaussian with a wire scanner in this region of the beamline which contradicts the BPM spectra. Therefore, the it is likely that the averaged cable and board corrections were insufficient and/or the impedance of the BPM is not properly being compensated.

3.3 Conclusion

Using the BPMs as profile monitors is a complicated measurement. It requires thorough understanding of the BPM's response to the beam and, especially at low β, it requires an

adequate model of the transverse profiles. Currently with the FRIB BPM system, neither of these requirements are achieved. These issues must be addressed before the BPMs can give reliable results.

Chapter 4

Helical transmission line for BPM calibration

Measurements with the BPMs at high gR_p are more challenging than measurements at lower gR_p. These measurements are also challenging to study because we must rely on analytic and numeric models that, in practice, cannot exactly model a BPM. It would be beneficial for BPM measurements at high g, both broadband measurements and position measurements, to have a test stand capable of calibrating and testing the BPMs in the regime where they will be operated. Measurements with high gR_p typically are made when the beam is traveling non-relativistically, i.e. low β. In order to calibrate for effects from non-relativistic beams, a test stand must be capable of replicating the measured beam's expected velocity and longitudinal profile and generate the correct field distribution on the BPM pickups. To calibrate and test the BPMs in the FRIB MEBT, this requires replicating a 200 ps long beam traveling at $\beta = 0.033$.

The typical test stand for calibrating for non-linearities in BPMs consists of a straight wire that is strung through the BPM [23]. A tone at the measurement frequency of the BPM is passed down the wire and the signals on the pickups are measured. This is repeated while moving the wire over a grid of positions within the BPM. The wire position is then related to the pickup signals with a polynomial fitting to calibrate the BPM response.

Because these test stands rely on a straight wire, they propagate signals at the speed of light and cannot be used to calibrate for non-relativistic effects. These devices are still useful for non-relativistic BPMs to calibrate for the velocity independent non-linear effects and validate the models in the speed of light limit.

One possible method to create a test stand capable of replicating non-relativistic beams is to use an electron beam tuned to match the properties of the desired beam. However, this relies on an entirely new test stand from the currently existing straight wire one which requires additional hardware and cost. It would be preferable to modify the existing test stand to allow for calibration for non-relativistic effects.

A possible structure to replace the straight wire is a Gaubou line which can propagate signals at less than the speed of light and are sometimes used to replicate electron beams to calibrate beamline devices **??**. Gaubou lines are single conductor transmission lines comprised of a conducting wire of radius R_i covered in a dielectric with radius a and permittivity ϵ_i (Fig. 4.1). This dielectric layer causes a surface wave to propagate at less than the speed of light. The dispersion relation for a Gaubou line centered in a conducting pipe of radius R_e is

$$\frac{\gamma_i}{\epsilon_i}\frac{I_0(\gamma_i R_i)K_0(\gamma_i a) - I_0(\gamma_i a)K_0(\gamma_i R_i)}{I_0(\gamma_i R_i)K_1(\gamma_i a) + I_1(\gamma_i a)K_0(\gamma_i R_i)} = \frac{\gamma_e}{\epsilon_e}\frac{I_0(\gamma_e R_e)K_0(\gamma_e a) - I_0(\gamma_e a)K_0(\gamma_e R_e)}{I_0(\gamma_e R_e)K_1(\gamma_e a) + I_1(\gamma_e a)K_0(\gamma_e R_e)} \tag{4.1}$$

where γ_i and γ_e are the transverse propagation constants in the dielectric and outside the dielectric respectively. The longitudinal propagation constant h is found by

$$h^2 = \gamma_i^2 + \epsilon_i \mu \omega^2 = \gamma_e^2 + \epsilon_e \mu \omega^2 \tag{4.2}$$

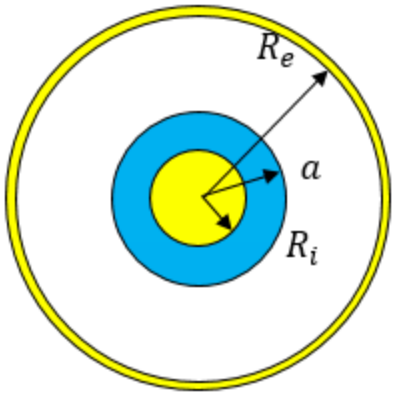

Figure 4.1: Cross section of a Gaubou line.

However, assuming $\epsilon_e = \epsilon_0$, the high frequency limit of the phase velocity $v_p = c/\sqrt{\epsilon_i}$ which it reaches when $\lambda \approx a$. In order to achieve a phase velocity of $v_p = 0.1c$, a material with a dielectric constant of 100 must be used which is impractical. In addition, the low frequency limit is significantly larger than the high frequency limit (Fig. 4.2). To calibrate the broadband measurements of the BPMs, the phase velocity must match the beam within the measured bandwidth, e.g. up to 0.5 GHz for the FRIB BPMs. The low frequency limit can be reduced by increasing a, however, even when the dielectric layer fills a significant portion of the beampipe, the reduction is not enough to reach non-relativistic phase velocities.

4.1 Helical RF structures

A radio frequency (RF) structure that is known to be capable of propagating at sufficiently low phase velocities is a helical transmission line. The low phase velocity of helices is relied on for devices such as slow traveling wave tubes . Many solutions and applications of helical RF structure properties have been published, however, most concern radiation modes for antennae or transmission lines for signal propagation at 10s to 100s of GHz . For use as a BPM test stand, the helical structure will be used as transmission line at low frequency with

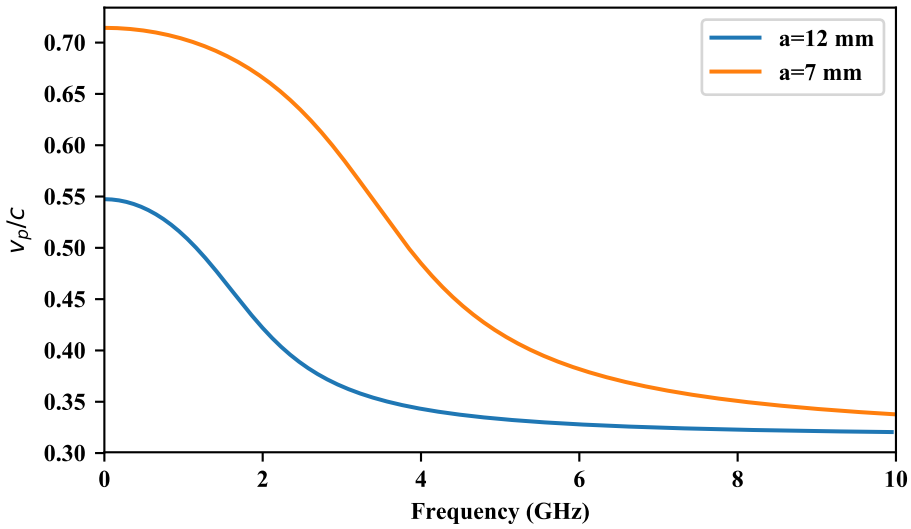

Figure 4.2: Normalized phase velocity of a Gaubou line with R_i=2 mm, R_e=20 mm, ϵ_i=10ϵ_0, and two different dielectric layer radii a. The low frequency limit is too large to replicate a non-relativistic beam.

a minimum usable bandwidth of $40 - 500$ MHz to fully calibrate the TIS waveforms.

While many of these solutions are not directly applicable to the use of a helical structure for a low frequency broadband transmission line, the general solutions can provide insights into the challenges of using a helical transmission line at lower frequencies. The dispersion relation for a helix in free space [24] shows the high frequency limit of the phase velocity is $v_p = c \cdot \sin(\psi)$ where ψ is the pitch angle of the helix. While this appears to allow these structures to be created for any desired beam velocity by constructing a helix with the correct ψ, the low frequency limit of the phase velocity is the speed of of light. This clearly will not replicate the velocity of a non-relativistic beam within the desired frequency band and, in addition, the large discrepancy between the high and low frequency limits quickly causes the input pulse to deform due to dispersion making replicating the correct bunch shape challenging. Most transmission can ignore these effects because they operate at higher frequencies where the phase velocity mostly constant and has reached its high

frequency limit. These effects will affect the lower frequency transmission line and steps must be taken to mitigate this issue.

4.2 Helical transmission lines - analytic solution

The geometry of a helical conductor makes exactly solving for the electromagnetic fields challenging. However, the boundary conditions can be significantly simplified using the sheath helix model [24]. This model approximates a helix as a thin cylinder that conducts on a helical path along the surface making the structure a 1D conductor that is longitudinally uniform. Specifically, the boundary conditions at the helix become

$$E_{\parallel}^{i} = E_{\parallel}^{e} = 0 \tag{4.3}$$

$$E_{\perp}^{i} = E_{\perp}^{e} \tag{4.4}$$

$$H_{\parallel}^{i} = H_{\parallel}^{e} \tag{4.5}$$

where the superscripts e and i denote fields in the external and internal regions of the helix and the subscripts $\parallel$ and $\perp$ denote the field components parallel and perpendicular to the direction of conductivity of the sheath helix. These unit vectors in cylindrical coordinates are

$$\hat{\parallel} = \sin(\psi)\hat{z} + \cos(\psi)\hat{\theta} \tag{4.6}$$

$$\hat{\perp} = \cos(\psi)\hat{z} + \sin(\psi)\hat{\theta} \tag{4.7}$$

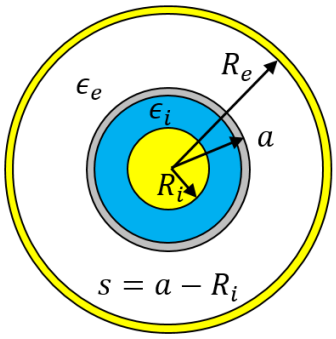

Figure 4.3: Cross section of helical transmission line geometry.

where ψ is the pitch angle of the helix. While this model is an abstraction from real helix, it is shown below that it well represents the tightly wound helices needed to replicate slow beams.

The transmission line for the test stand consists of a helix of radius a and pitch ψ, a conducting rod of radius R_i centered inside of the helix, a dielectric with permittivity ϵ_i of thickness $s = a - R_i$ fills the space between the rod and the helix to support the helix, and the helix is centered inside a conducting pipe of radius R_e. The analytic solution also assumes the region between the helix and the outer conductor is filled with a dielectric with permittivity ϵ_e; however, this is set to ϵ_0 for all studies (Fig. 4.3).

The derivation of the electromagnetic fields presented here follows the work of S. Sensiper and others starting with the Hertzian potentials

$$\nabla^2 \mathbf{\Pi_e} - \mu\epsilon \frac{\partial^2 \mathbf{\Pi_e}}{\partial t^2} = 0 \tag{4.8}$$

$$\nabla^2 \mathbf{\Pi_m} - \mu\epsilon \frac{\partial^2 \mathbf{\Pi_m}}{\partial t^2} = 0. \tag{4.9}$$

If $\mathbf{\Pi_e}$ and $\mathbf{\Pi_m}$ are assumed to only have a $\hat{z}$ component, then the fields are given by

$$\mathbf{E} = \nabla \times \nabla \times \mathbf{\Pi_e} - \nabla \times \frac{\partial^2 \mathbf{\Pi_m}}{\partial t^2} \tag{4.10}$$

$$\mathbf{H} = \nabla \times \nabla \times \mathbf{\Pi_m} - \nabla \times \frac{\partial^2 \mathbf{\Pi_e}}{\partial t^2}. \tag{4.11}$$

In cylindrical coordinates the general field equations in the internal region are

$$E_{i,r} = \Big[-ih\gamma_i \left(\mathrm{I}'_n(\gamma_i r) A^{(1)}_{i,n} + \mathrm{K}'_n(\gamma_i r) A^{(2)}_{i,n}\right) - \frac{\omega\mu n}{r}\left(\mathrm{I}_n(\gamma_e r) B^{(1)}_{i,n} + \mathrm{K}_n(\gamma_i r) B^{(2)}_{i,n}\right)\Big] e^{-in\theta} e^{-ihz} \tag{4.12}$$

$$E_{i,\theta} = \Big[-\frac{hn}{r}\left(\mathrm{I}_n(\gamma_i r) A^{(1)}_{i,n} + \mathrm{K}_n(\gamma_i r) A^{(2)}_{i,n}\right) + i\omega\mu\gamma_i \left(\mathrm{I}'_n(\gamma_e r) B^{(1)}_{i,n} + \mathrm{K}'_n(\gamma_i r) B^{(2)}_{i,n}\right)\Big] e^{-in\theta} e^{-ihz} \tag{4.13}$$

$$E_{i,z} = -\gamma_i^2 \left[\mathrm{I}_n(\gamma_i r) A^{(i)}_{i,n} + \mathrm{K}_n(\gamma_i r) A^{(2)}_{i,n}\right] e^{-in\theta} e^{-ihz} \tag{4.14}$$

$$H_{i,r} = \Big[\frac{\omega\epsilon_i n}{r}\left(\mathrm{I}_n(\gamma_i r) A^{(1)}_{i,n} + \mathrm{K}_n(\gamma_i r) A^{(2)}_{i,n}\right) - ih\gamma_i \left(\mathrm{I}'_n(\gamma_i r) B^{(1)}_{i,n} + \mathrm{K}'_n(\gamma_i r) B^{(2)}_{i,n}\right)\Big] e^{-in\theta} e^{-ihz} \tag{4.15}$$

$$H_{i,\theta} = \Big[-i\omega\epsilon_i\gamma_i \left(\mathrm{I}'_n(\gamma_i r) A^{(1)}_{i,n} + \mathrm{K}'_n(\gamma_i r) A^{(2)}_{i,n}\right) - \frac{hn}{r}\left(\mathrm{I}_n(\gamma_e r) B^{(1)}_{i,n} + \mathrm{K}_n(\gamma_i r) B^{(2)}_{i,n}\right)\Big] e^{-in\theta} e^{-ihz} \tag{4.16}$$

$$H_{i,z} = -\gamma_i^2 \left[\mathrm{I}_n(\gamma_i r) B^{(1)}_{i,n} + \mathrm{K}_n(\gamma_i r) B^{(2)}_{i,n}\right] e^{-in\theta} e^{-ihz} \tag{4.17}$$

where I_n and K_n are the modified Bessel functions of the first and second kind and γ_i and h_i are the transverse and longitudinal propagation constants respectively and are related by

$$h^2 = k_i^2 + \gamma_i^2 \tag{4.18}$$

where $k_i = \sqrt{\mu\epsilon_i}\omega$ is the free space propagation constant. The external fields have the same form except with different propagation constants and coefficients and are denoted by exchanging the subscript i for e.

The field coefficients $A_{i,n}^{(1)}$, $A_{i,n}^{(2)}$, $A_{e,n}^{(1)}$, $A_{e,n}^{(2)}$, $B_{i,n}^{(1)}$, $B_{i,n}^{(2)}$, $B_{e,n}^{(1)}$, and $B_{e,n}^{(2)}$ are found by applying the boundary conditions at the helix (Eqs. 4.3, 4.4, 4.5) and the inner and outer conducting surfaces. The boundary conditions in cylindrical coordinates at the conductors and the sheath helix are

$$E_{i,z}\big|_{R_i} = 0 \tag{4.19}$$

$$E_{i,\theta}\big|_{R_i} = 0 \tag{4.20}$$

$$H_{i,r}\big|_{R_i} = 0 \tag{4.21}$$

$$E_{e,z}\big|_{R_e} = 0 \tag{4.22}$$

$$E_{e,\theta}\big|_{R_e} = 0 \tag{4.23}$$

$$H_{e,r}\big|_{R_e} = 0 \tag{4.24}$$

$$H_{i,z}\big|_a + H_{i,\theta}\big|_a \cot(\psi) = H_{e,z}\big|_a + H_{e,\theta}\big|_a \cot(\psi) \tag{4.25}$$

$$H_{i,r}\big|_a = H_{e,r}\big|_a \tag{4.26}$$

$$E_{i,z}\big|_a = E_{e,z}\big|_a \tag{4.27}$$

$$E_{i,\theta}\big|_a = E_{e,\theta}\big|_a \tag{4.28}$$

$$E_{e,z}\big|_a = -E_{e,\theta}\big|_a \cot(\psi) \tag{4.29}$$

$$E_{i,z}\big|_a = -E_{i,\theta}\big|_a \cot(\psi), \tag{4.30}$$

Only a linearly independent subset of the boundary conditions are needed to solve for the field coefficients. Using $A_{i,n}^{(1)}$ as an overall amplitude and Eqs. 4.19, 4.21, 4.23, 4.24, 4.25,

4.27, and 4.28 the field coefficients become:

$$A_{i,n}^{(2)} = -A_{i,n}^{(1)} \cdot \frac{\mathrm{I}_n\left(\gamma_i R_i\right)}{\mathrm{K}_n\left(\gamma_i R_i\right)} \tag{4.31}$$

$$A_{e,n}^{(2)} = -A_{e,n}^{(1)} \cdot \frac{\mathrm{I}_n\left(\gamma_e R_e\right)}{\mathrm{K}_n\left(\gamma_e R_e\right)} \tag{4.32}$$

$$A_{e,n}^{(1)} = A_{i,n}^{(1)} \cdot \frac{\gamma_i^2}{\gamma_e^2} \frac{K_n(\gamma_e R_e) w_{1,i}}{K_n(\gamma_i R_i) w_{1,e}} \tag{4.33}$$

$$B_{i,n}^{(2)} = -B_{i,n}^{(1)} \cdot \frac{\mathrm{I}_n'\left(\gamma_i R_i\right)}{\mathrm{K}_n'\left(\gamma_i R_i\right)} \tag{4.34}$$

$$B_{e,n}^{(2)} = -B_{e,n}^{(1)} \cdot \frac{\mathrm{I}_n'\left(\gamma_e R_e\right)}{\mathrm{K}_n'\left(\gamma_e R_e\right)} \tag{4.35}$$

$$\begin{aligned} B_{i,n}^{(1)} = -iA_{i,n}^{(1)} \cdot \Bigg[& a^2 \gamma_i \gamma_e^2 \mathrm{K}_n'\left(\gamma_i R_i\right) w_{4,e} \left(\gamma_i k_e^2 w_{1,i} w_{2,e} - \gamma_e k_i^2 w_{1,e} w_{2,i}\right) \\ & - nh w_{1,i} w_{1,e} w_{3,e} \mathrm{K}_n'\left(\gamma_i R_i\right) \left(nh\cot(\psi) + a\gamma_e^2\right) \left(\gamma_i^2 - \gamma_e^2\right) \Bigg] \times \\ & \Bigg\{ a\mu\omega\gamma_e^2 \mathrm{K}_n\left(\gamma_i R_i\right) w_{1,e} \times \\ & \left[\gamma_i \left(nh\cot(\psi) + a\gamma_e^2\right) w_{3,e} w_{4,i} - \gamma_e \left(nh\cot(\psi) + a\gamma_i^2\right) w_{3,i} w_{4,e}\right] \Bigg\}^{-1} \end{aligned} \tag{4.36}$$

$$\begin{aligned} B_{e,n}^{(1)} = B_{i,n}^{(1)} \cdot \Bigg[& a^2 \gamma_i^2 \gamma_e \mathrm{K}_n'\left(\gamma_e R_e\right) w_{4,i} \left(\gamma_i k_e^2 w_{1,i} w_{2,e} - \gamma_e k_i^2 w_{1,e} w_{2,i}\right) \\ & - nh w_{1,i} w_{1,e} w_{3,i} \mathrm{K}_n'\left(\gamma_e R_e\right) \left(nh\cot(\psi) + a\gamma_i^2\right) \left(\gamma_i^2 - \gamma_e^2\right) \Bigg] \times \\ & \Bigg[a^2 \gamma_e \gamma_i^2 \mathrm{K}_n'\left(\gamma_i R_i\right) w_{4,e} \left(\gamma_i k_e^2 w_{1,i} w_{2,e} - \gamma_e k_i^2 w_{1,e} w_{2,i}\right) \\ & - nh w_{1,i} w_{1,e} w_{3,e} \mathrm{K}_n'\left(\gamma_i R_i\right) \left(nh\cot(\psi) + a\gamma_e^2\right) \left(\gamma_i^2 - \gamma_e^2\right) \Bigg]^{-1} \end{aligned} \tag{4.37}$$

where

$$w_{1,i,e} = \mathrm{I}_n\left(\gamma_{i,e}a\right)\mathrm{K}_n\left(\gamma_{i,e}R_{i,e}\right) - \mathrm{I}_n\left(\gamma_{i,e}R_{i,e}\right)\mathrm{K}_n\left(\gamma_{i,e}a\right) \tag{4.38}$$

$$w_{2,i,e} = \mathrm{I}'_n\left(\gamma_{i,e}a\right)\mathrm{K}_n\left(\gamma_{i,e}R_{i,e}\right) - \mathrm{I}_n\left(\gamma_{i,e}R_{i,e}\right)\mathrm{K}'_n\left(\gamma_{i,e}a\right) \tag{4.39}$$

$$w_{1,i,e} = \mathrm{I}_n\left(\gamma_{i,e}a\right)\mathrm{K}'_n\left(\gamma_{i,e}R_{i,e}\right) - \mathrm{I}'_n\left(\gamma_{i,e}R_{i,e}\right)\mathrm{K}_n\left(\gamma_{i,e}a\right) \tag{4.40}$$

$$w_{1,i,e} = \mathrm{I}'_n\left(\gamma_{i,e}a\right)\mathrm{K}'_n\left(\gamma_{i,e}R_{i,e}\right) - \mathrm{I}'_n\left(\gamma_{i,e}R_{i,e}\right)\mathrm{K}'_n\left(\gamma_{i,e}a\right). \tag{4.41}$$

The dispersion relation can be found by creating a matrix from the boundary conditions used to determine the field coefficients and setting the characteristic equation to 0.

$$\begin{vmatrix}
0 & 0 & I_n(\gamma_e R_e) & K_n(\gamma_e R_e) \\
0 & 0 & \frac{n\epsilon_e\omega}{R_e} I_n(\gamma_e R_e) & \frac{n\epsilon_e\omega}{R_e} K_n(\gamma_e R_e) \\
I_n(\gamma_i R_i) & K_n(\gamma_i R_i) & 0 & 0 \\
\frac{n\epsilon_i\omega}{R_i} I_n(\gamma_i R_i) & \frac{n\epsilon_i\omega}{R_i} K_n(\gamma_i R_i) & 0 & 0 \\
-i\omega\cot(\psi)\gamma_i\epsilon_i I'_n(\gamma_i a) & -i\omega\cot(\psi)\gamma_i\epsilon_i K'_n(\gamma_i a) & i\omega\cot(\psi)\gamma_e\epsilon_e I'_n(\gamma_e a) & i\omega\cot(\psi)\gamma_e\epsilon_e K'_n(\gamma_e a) \\
0 & 0 & -\left(\gamma_e^2 + \frac{nh}{a}\cot(\psi)\right) I_n(\gamma_e a) & -\left(\gamma_e^2 + \frac{nh}{a}\cot(\psi)\right) K_n(\gamma_e a) \\
-\gamma_i^2 I_n(\gamma_i a) & -\gamma_i^2 K_n(\gamma_i a) & \gamma_e^2 I_n(\gamma_e a) & \gamma_e^2 K_n(\gamma_e a) \\
-\frac{nh}{a} I_n(\gamma_i a) & -\frac{nh}{a} K_n(\gamma_i a) & \frac{nh}{a} I_n(\gamma_e a) & \frac{nh}{a} K_n(\gamma_e a)
\end{vmatrix}$$

$$\begin{vmatrix}
0 & 0 & 0 & 0 \\
0 & 0 & -ih\gamma_e I'_n(\gamma_e R_e) & -ih\gamma_e I'_n(\gamma_e R_e) \\
0 & 0 & 0 & 0 \\
-ih\gamma_i I'_n(\gamma_i R_i) & ih\gamma_i K'_n(\gamma_i R_i) & 0 & 0 \\
-\left(\gamma_i^2 + \frac{nh}{a}\cot(\psi)\right) I_n(\gamma_i a) & -\left(\gamma_i^2 + \frac{nh}{a}\cot(\psi)\right) K_n(\gamma_i a) & \left(\gamma_e^2 + \frac{nh}{a}\cot(\psi)\right) I_n(\gamma_e a) & \left(\gamma_e^2 + \frac{nh}{a}\cot(\psi)\right) K_n(\gamma_e a) \\
0 & 0 & i\mu\omega\cot(\psi)\gamma_e I'_n(\gamma_e a) & i\mu\omega\cot(\psi)\gamma_e K'_n(\gamma_e a) \\
0 & 0 & 0 & 0 \\
i\mu\omega\gamma_i I_n(\gamma_i a) & i\mu\omega\gamma_i K_n(\gamma_i a) & -i\mu\omega\gamma_e I_n(\gamma_e a) & -i\mu\omega\gamma_e I_n(\gamma_e a)
\end{vmatrix} = 0 \tag{4.42}$$

After simplification the dispersion relation is

$$\begin{aligned} 0 =& \gamma_i^3 \left[nh\cot(\psi) + a\gamma_e^2 \right]^2 w_{1,i} w_{1,e} w_{3,e} w_{4,i} + \gamma_e^3 \left[nh\cot(\psi) + a\gamma_i^2 \right]^2 w_{1,i} w_{1,e} w_{3,i} w_{4,e} \\ &+ a^2 \cot^2(\psi) \gamma_e^2 \gamma_i^2 w_{4,i} w_{4,e} \left(\gamma_e k_i^2 w_{1,e} w_{2,i} - \gamma_i k_e^2 w_{1,i} w_{2,e} \right). \end{aligned} \tag{4.43}$$

This is solved numerically for γ_e as a function of k_e using

$$\gamma_e^2 = \gamma_i^2 + k_i^2 - k_e^2 \tag{4.44}$$

and $h(\omega)$ can be determined along with the phase velocity $v_p(\omega) = k_e/h = \beta c$.

4.2.1 Dispersion distortion correction

In order to produce the specific pulse shape at the device under test, it is ideal for the phase velocity to be constant with frequency so any pulse input into the transmission line will not be deformed throughout propagation. However, for a helix in free space, the phase velocity varies from $\beta = 1$ to $\beta = \sin(\psi)$ which causes significant deformation to any input pulse. Initial designs of the test stand added a conducting pipe around the helix. For this geometry, the low frequency limit of the phase velocity was significantly less than $\beta = 1$ (Fig. 4.6). However, the deformation due to dispersion was still a major issue.

One method to mitigate the deterioration is to use dispersion itself to correct the pulse at a given location. This is achieved by propagating the desired pulse along the helix and measuring the pulse at the desired location of the device under test. This pulse is then reversed in time and input into the helix. This effectively subtracts the accumulated phase shifts at each frequency due to dispersion and the original signal will be reconstructed at

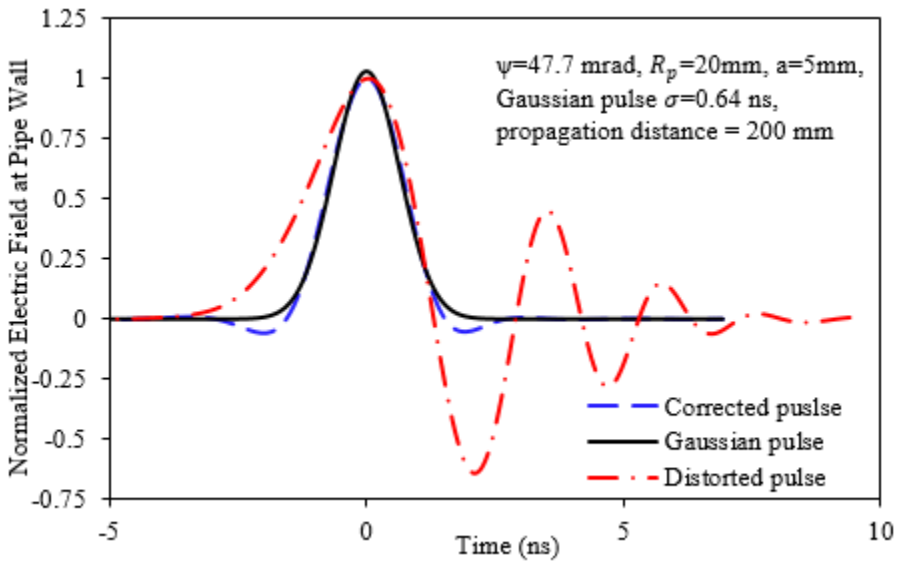

Figure 4.4: The deformed pulse is found by analytically propagating a pulse a set distance. It is then reversed in time and input into the transmission line. When this pulse is propagated along the transmission line, the dispersion will correct the pulse at the set distance. The DUT can be placed at this location.

the place of measurement (Fig. 4.4). This method was rejected because the deformed pulses input into the helix are rather complex and generating one would have proved challenging.

Another considered method was to slowly decrease the pitch of the helix from a loosely wound helix at the input to the required pitch for the desired velocity. In the region of decreasing ψ, the decreasing pitch compressed the pulse more quickly than dispersion could distort it. This results in a shorter pulse at the end of the compression section that was input and minimal deformation (Fig. 4.5). Once the pulse propagates along the constant pitch portion of the system, the effects of dispersion once again deforms the pulse shape. For this case the device under test could be placed directly after the compression section to measure the desired pulse shape at the correct velocity.

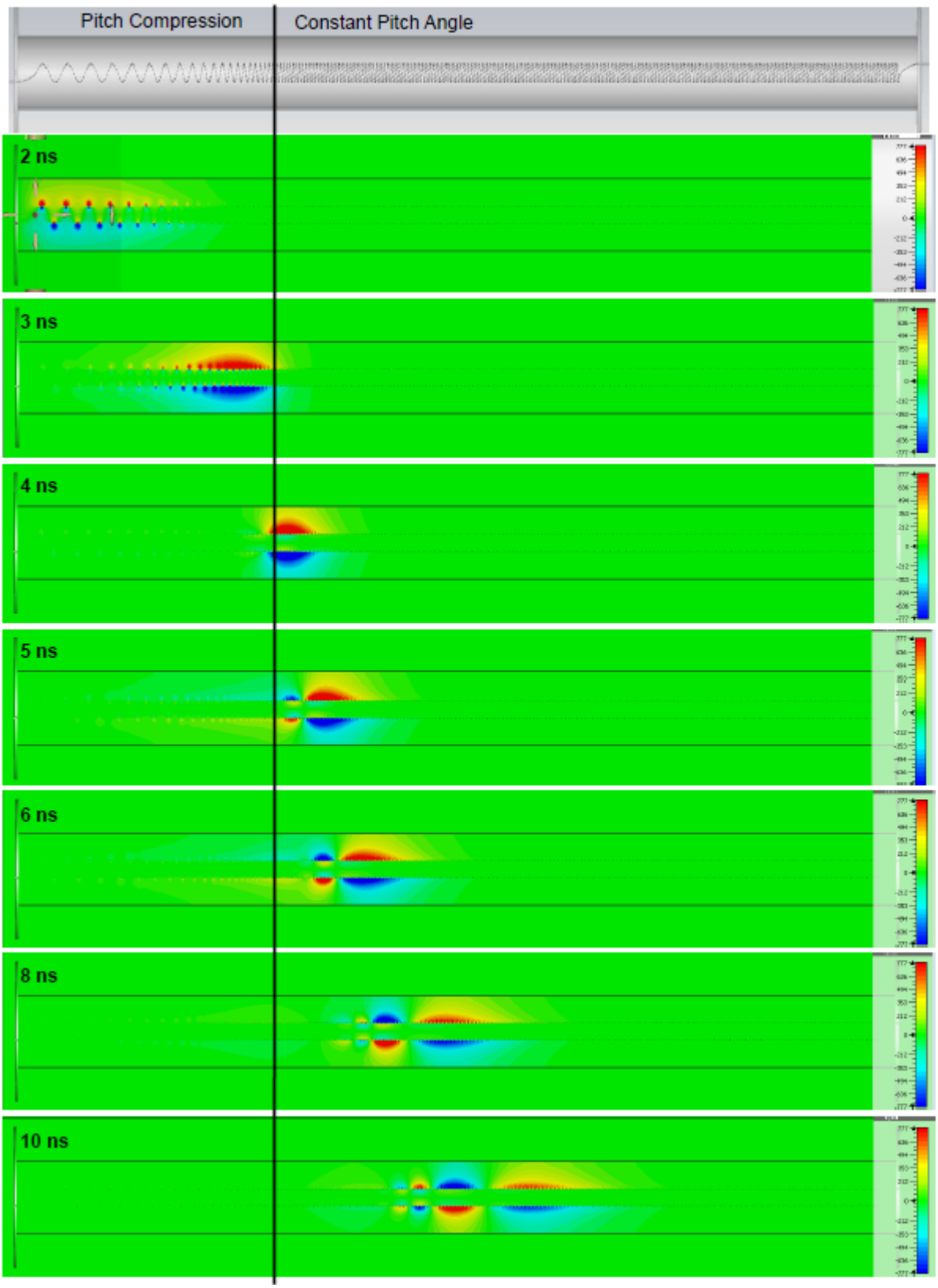

Figure 4.5: Propagation of a Gaussian pulse along a helix with reducing pitch. The pulse is compressed but maintains its form during the pitch reduction but dispersion deforms the pulse in the constant pitch section

4.2.2 Dispersion reduction geometry

A more practical solution to prevent pulse deformation is to add an conductor inside of the helix. The hypothesis was this would increase the capacitance of the system which would lower the phase velocity at low frequency while leaving the high frequency limit unchanged. Using s=0.5 mm, the dispersion becomes significantly flatter than without the inner conductor with all other geometry the same. The change total variation in phase velocity is Δv_p=0.039 without the inner conductor and Δv_p=0.001 with the inner conductor for the parameters given in Fig. 4.6. Numerically solving Eq. 4.43 shows the low frequency limit of the phase velocity linearly increases with separation s between the helix and inner conductor as approximately

$$\lim_{f \to 0} (v_p) \propto 0.0025s. \tag{4.45}$$

for s in mm. The high frequency limit remains the same but the phase velocity converges more slowly for smaller s. The slow convergence results in less variation in v_p over a given bandwidth despite the larger variation between the low and high frequency limits. For example, in Fig. 4.7, for a bandwidth up to 1 GHz, s=1 mm have a range of Δv_p=0.0028 and for s=0.1 mm Δv_p=0.00057. Therefore, a narrow separation should be used when constructing a helical transmission line to limit the deformation of pulses.

The dielectric constant of the dielectric layer can also be varied. In the case of $\epsilon_i = \epsilon_e = \epsilon_0$, the high frequency limit of the phase velocity is $v_p = c \cdot \sin(\psi)$ and the low frequency limit is higher than this. As the internal dielectric constant increases the high frequency limit drops approximately as $\epsilon_i^{-1/3}$ for a fixed geometry while the low frequency limit drops as $\epsilon_i^{-1/2}$ (Fig. 4.7). This causes the low frequency limit to drop below the high frequency limit. The difference in scaling causes the disparity between the low and high frequency limits

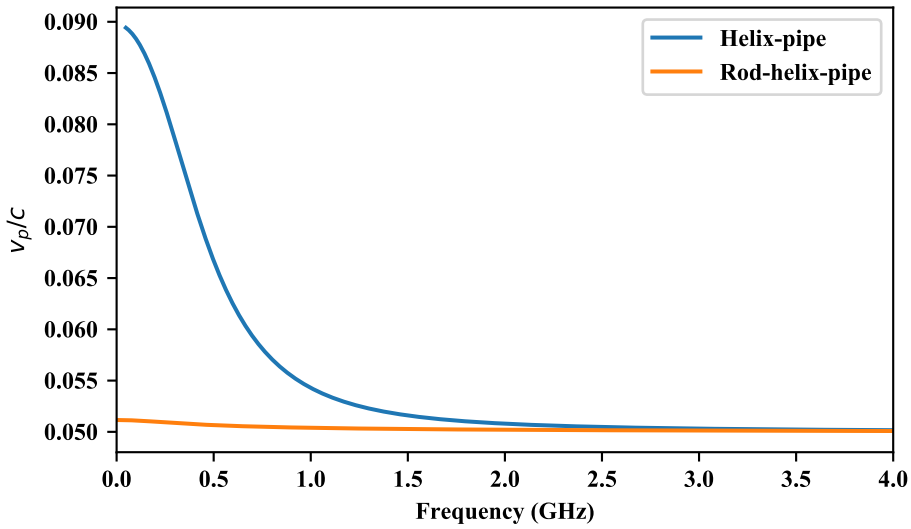

Figure 4.6: Dispersion for different transmission line geometries. The addition of the inner conductor significantly flattens $v_p(\omega)$. Helix parameters s=0.5 mm, a=5 mm, R_e=23.75 mm, ψ=0.05, $\epsilon_i = \epsilon_0$.

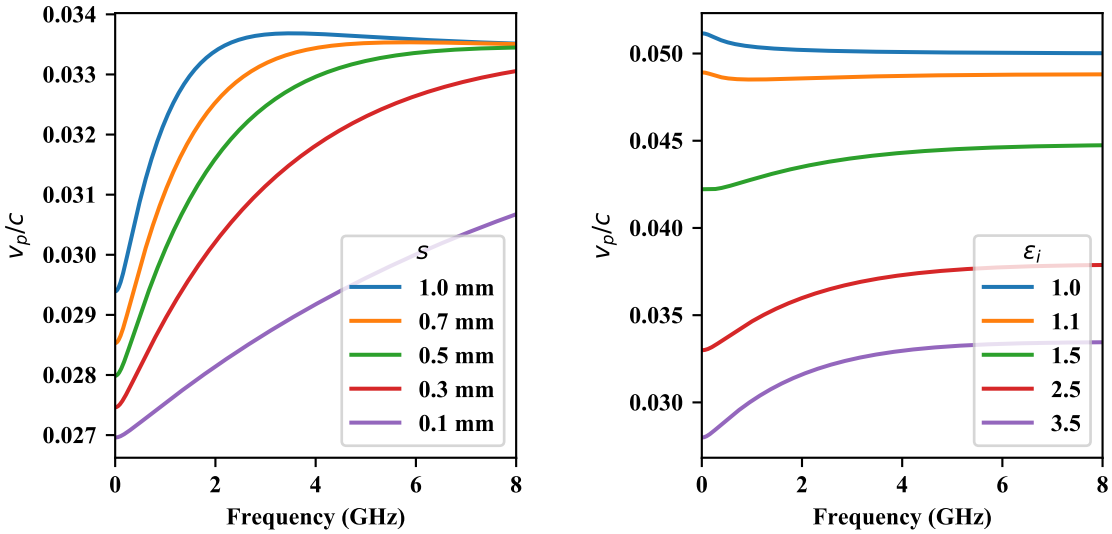

Figure 4.7: Dispersion scaling with s (left) and ϵ_r (right). Helix parameters: s=0.5 mm, a=5 mm, R_e=23.75 mm, ψ=0.05, $\epsilon_i = \epsilon_0$.

of the phase velocity to increase with ϵ_i which is non-ideal for maintaining pulse shapes. However, its effects can be mitigated by reducing s. In theory, the dielectric constant can be chosen such that the high and low frequency limits of v_p are equal which would be an ideal system, however, in practice this is difficult to realize.

It should be noted that while significant efforts were made to flatten the dispersion curve, the pulses near the helix still become significantly deformed due to dispersion. This is caused by the short pulse propagating along helix of $\sim$200 ps rms needed to replicate the bunch. For pulses this short the bandwidth is large enough to cause significantly different phase shifts resulting in distortion. However, the fields near the helix are not representative of the fields at the pipe wall where they will be measured by the BPM being calibrated. As the radial distance from the helix increases, the high frequency components are suppressed because the field is non-relativistic. Therefore, the fields at the pipe wall will propagate with minimal deformation even though the signal near the helix has significant distortions (Fig. 4.8).

For the test stand, the helix will need to be offset in the pipe. As shown below, this does not change the dispersion properties, however, it will reduce the radial distance between the helix and the pipe wall resulting in a shorter pulse being measured by at least one of the BPM pickups. Fortunately, for offsets up to 5 mm, the higher frequencies are still sufficiently suppressed in the measured bandwidth and the measured signals are still not significantly deformed.

4.2.3 Higher order effects

The discussions above focuses solely on the $n = 0$ mode, however, helical transmission lines support higher order modes . The n^{th} higher order mode is excited at $ka \approx n$. For $a = 5$ mm which will be used for the test stand, this corresponds to $\omega \approx$10 Ghz which is well outside the

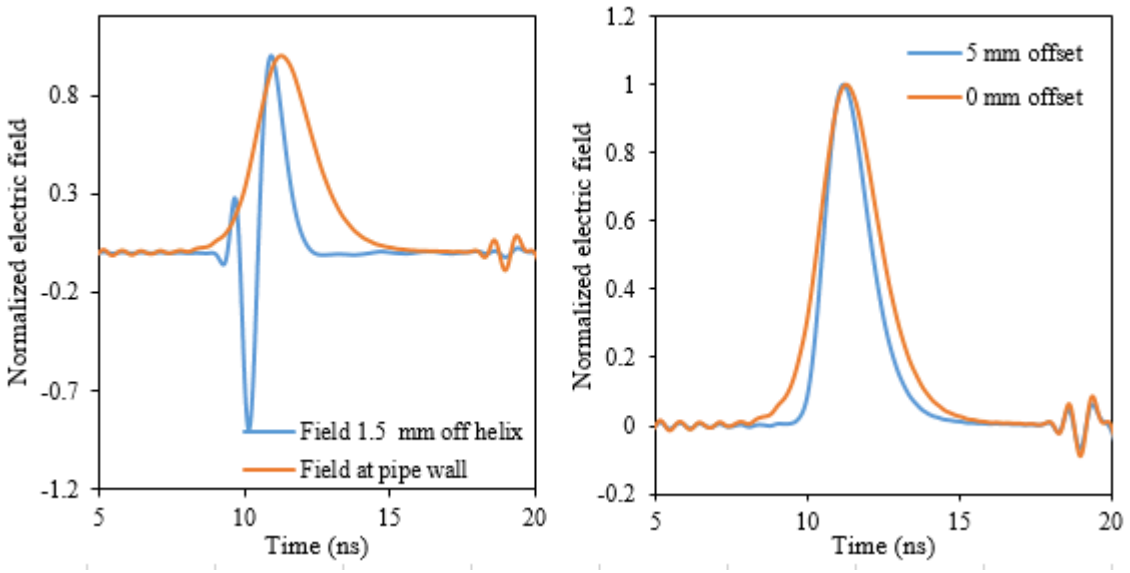

Figure 4.8: Despite efforts to reduce dispersion effects, the pulses near the helix are significantly deformed due to dispersion (left). However, the fields near the pipe wall have the high frequency components suppressed and therefore maintain their shape. This same effect distorts the pulse when the helix is offset in the pipe. Offsets up to 5 mm can be achieved with minimal deformations (right). The pulses shown here are from Microwave Studio simulations.

required bandwidth. Unlike the $n = 0$ mode which has significantly reduced phase velocity at low frequency compared to the helix in free space, the higher order modes propagate at $v_p(\omega_c) = c$ at the cutoff frequency (Fig. 4.9). The high frequency limits of the higher order modes are the same as the $n = 0$ mode.

The presented analysis relies solely on the sheath helix model. More complex models can also be made using a tape helix with windings of finite width. These models introduce forbidden regions in $k - h$ space and near the boundaries of these regions, the dispersion diverges from the sheath helix model . However, for the given geometry, the required bandwidth is far from a forbidden region and the sheath helix model is a reasonable approximation. In addition, the tape helix models predict radiating modes at low frequencies. It is believed that these are seen in simulations, however these travel near the speed of light and can be easily separated from the slow signals .

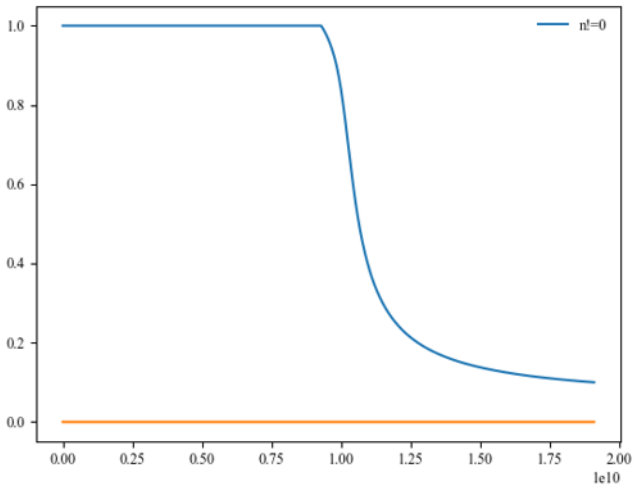

Figure 4.9: Dispersion for the first higher order mode.

4.2.4 Impedance Properties

Once the field coefficients and propagation are found, a complete description of the fields is known and the impedance can be calculated. For the three conductor geometry described above, two separate impedances can be defined: Z_i which between the inner conductor and the helix, and Z_e between the helix and pipe. The impedance in each region was calculated by

$$Z_i = \frac{\int_{R_i}^{a} E_{r,i} \mathrm{d}r}{a \int_{-\pi}^{\pi} H_{\theta,i}(a) \mathrm{d}\theta} \tag{4.46}$$

$$Z_e = \frac{\int_{a}^{R_e} E_{r,e} \mathrm{d}r}{R_e \int_{-\pi}^{\pi} H_{\theta,e}(R_e) \mathrm{d}\theta - a \int_{-\pi}^{\pi} H_{\theta,i}(a) \mathrm{d}\theta}. \tag{4.47}$$

In general, these are similar except at low frequencies (Fig. 4.10).

Reducing s maintains the high frequency behavior of the impedance but reduces the low frequency limit and reduces the variation at lower frequencies. This causes the impedance to converge more slowly to the high frequency behavior (Fig. 4.10). Ideally, a small enough

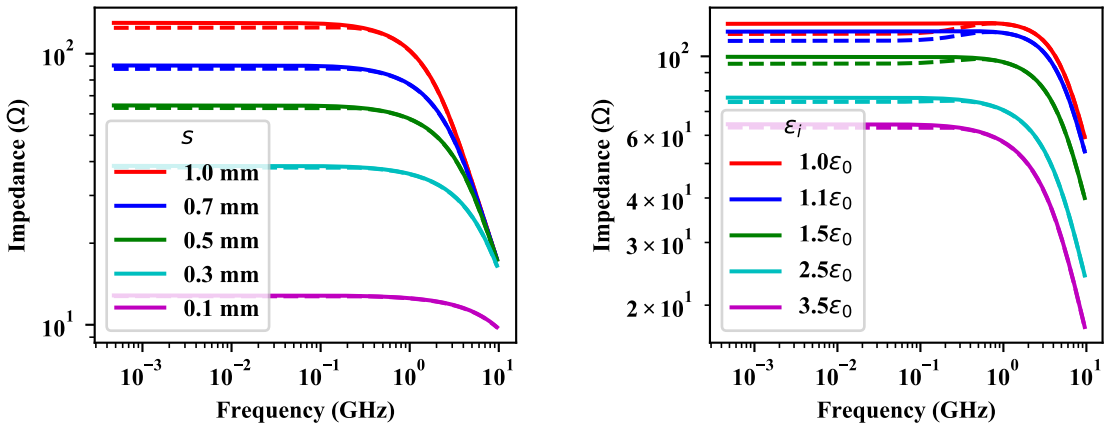

Figure 4.10: Impedance scaling with s and ϵ_i. The solid line is the external impedance and the dashed line is the internal. Helix parameters: s=0.5 mm, a=5 mm, R_e=23.75 mm, ψ=0.05, $\epsilon_i = \epsilon_0$.

s should be used to achieve a near constant Z over the desired bandwidth so the input and output of the helical transmission line can easily matched with a resistive network. Increasing the dielectric constant reduces the low frequency limit of the impedance and causes the impedance to start to decrease at a lower frequency. While it is preferable to use a lower dielectric constant to increase the bandwidth of near constant impedance region, the effect of the dielectric is not as significant as the effect of s.

To avoid internal reflections due to changes to the impedance caused by variations in construction, the geometric parameters were varied in the analytic model to determine to which the system is most sensitive. The impedance is primarily sensitive to the the inner conductor radius and helix radius, but they have opposite effects the impedance. For example as seen in Fig. 4.11, a 5% increase in the helix radius causes an almost 50% increase in the low frequency limit of the impedance while increasing the inner conductor radius by 5% reduces the impedance by $\sim 50\%$. Therefore, the separation between the helix and inner conductor must be constant along the transmission line to limit large variations in the impedance for

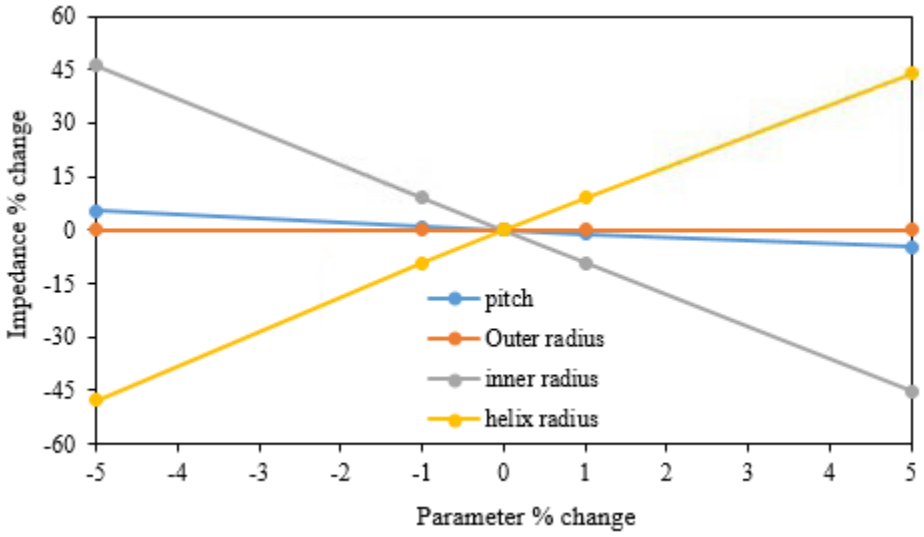

Figure 4.11: Sensitivity of the low frequency limit of the external impedance to variation of different parameters. The impedance is most susceptible to changes in s.

even small changes. The radius of the inner conductor can vary as long as the helix radius also changes to keep the separation the same. Other geometry factors, such as the pitch and outer pipe radius, have a minimal impact on the impedance compared to the separation.

4.2.4.1 Inductance and Capacitance

To create a circuit model of the transmission line, the inductance L and capacitance C per unit length of the lossless helical transmission line can be determined from the longitudinal propagation constant and impedance

$$L_{i,e} = \frac{h}{\omega}\frac{1}{Z_{i,e}} \tag{4.48}$$

$$C_{i,e} = \frac{h}{\omega}Z_{i,e}. \tag{4.49}$$

As with the impedance, these parameters are defined separately for the internal and external regions.

It was speculated above that the addition of the internal conductor increases the capacitance of the transmission line. This is effect can be seen by calculating the internal capacitance for different s (Fig. 4.12). Decreasing s does result in a larger capacitance at low frequency and converges to the same limit at high frequency. However, competing with this effect is a decrease in the inductance at low frequency with decreasing s which will increase the phase velocity. The inductance is decreased by almost the same factor as the increase in capacitance with the largest discrepancy seen at frequencies <1 GHz. This similarity results in minimal changes to the phase velocity and large changes to the impedance when changing s. As expected from Fig. 4.10, changing ϵ_i results in significant changes to the high and low frequency limits of the capacitance and impedance.

4.3 Simulations

Time domain simulations of the helical transmission line were performed in CST microwave studio with properties given in Table 4.1 unless otherwise stated. Simulations were performed up to 1.5 GHz which is well below the cutoff frequency of the first higher mode. Note, while it is best to minimize s to improve pulse propagation, $s = 0.5$ mm was used because it was impractical to create a mesh for smaller values. The mesh size was set to resolve the dielectric layer and spacing between windings with at least two mesh cells (Fig. 4.13). The helix has thickness Δa centered around the helix radius a.

4.3.1 Matching

The input signal was input using a stripline connected to the helix and inner conductor on either end of the helix (Fig. 4.14). For most simulations, the stripline impedance was

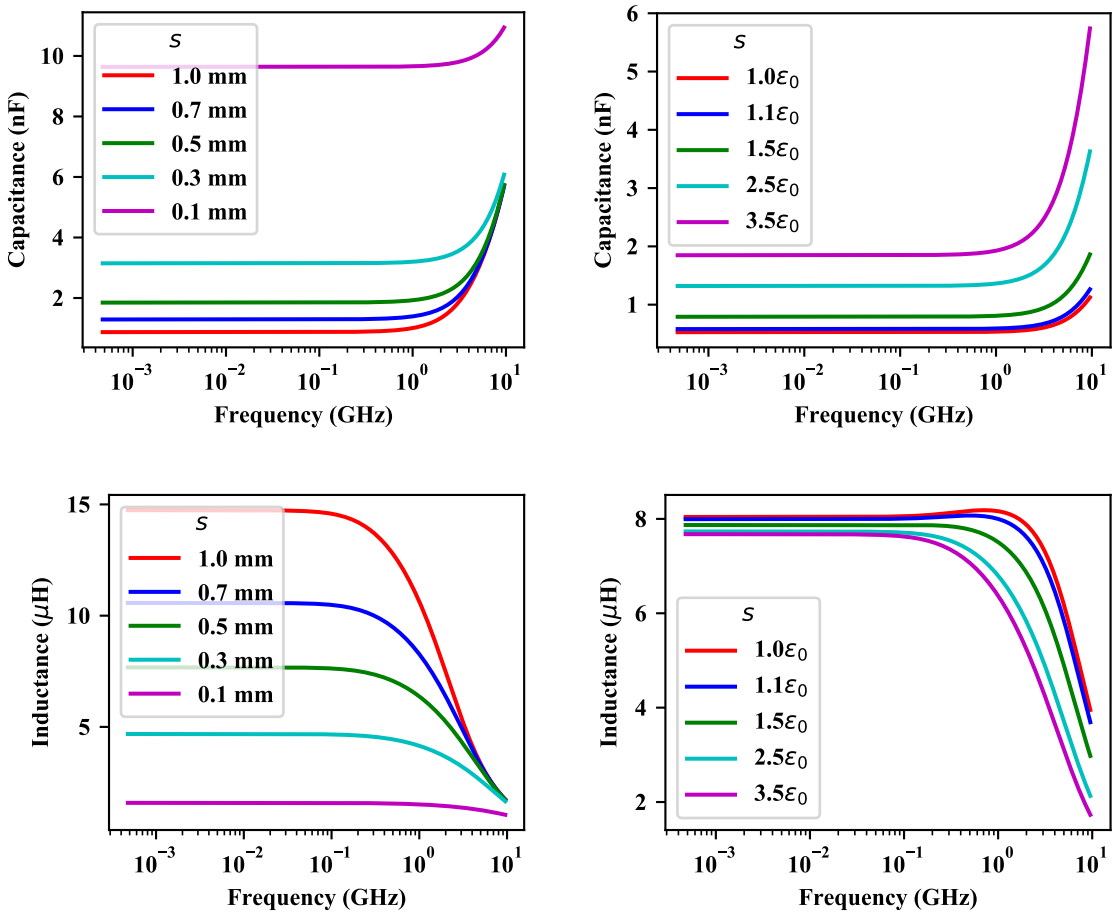

Figure 4.12: Scaling of the internal C and L with s and ϵ_i. The decreasing s reducing the capacitance and increases the inductance by approximately the same factor. Helix parameters: s=0.5 mm, a=5 mm, R_e=23.75 mm, ψ=0.05, $\epsilon_i = \epsilon_0$.

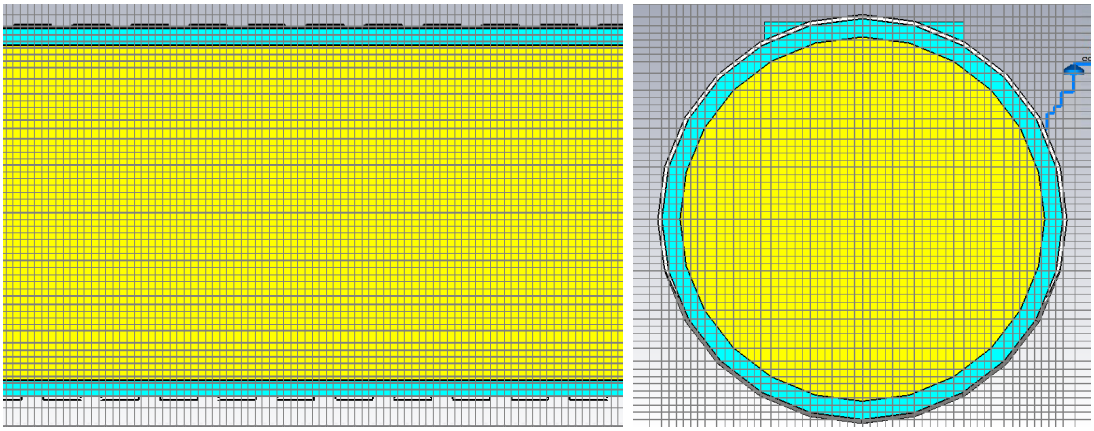

Figure 4.13: Meshing of helical transmission line in CST Microwave Studio for time domain simulations.

Table 4.1: Simulated helix parameters.

Pipe radius, R_e	20.65 mm
Inner conductor radius, R_i	4.5 mm
Helix radius, a	5 mm
Separation, s	0.5 mm
Pitch angle, ψ	0.05 rad
Dielectric constant, ϵ_i	$3.5\epsilon_0$
Helix wire width	1 mm
Helix wire thickness, Δa	0.1 mm

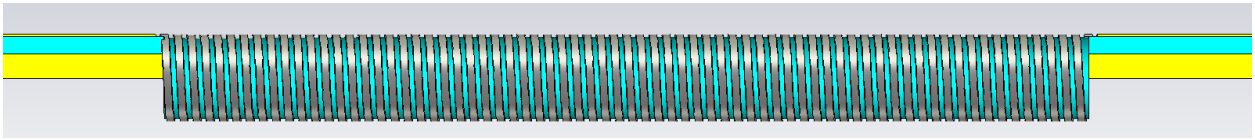

Figure 4.14: Helical transmission line model. Microstrips are used to match the input and output.

set equal to the low frequency limit of the helix impedance and no additional matching was done. Alternatively, the stripline impedance can also be mismatched from the helix impedance then matched using a resistive L-network. This matches the fields in the internal region. An additional resistor with impedance equal to the low frequency limit of Z_e must be placed between the outer conductor and helix to match the external fields (Fig. **??**).

With the stripline matched to the helix, a good match is seen with $S_{1,1}$ <-15 dB and $S_{2,1}$ >-1.5 dB up to 2 GHz. Strong resonances are seen corresponding the harmonics of the helix length for signals traveling at $v = \beta c$. These resonances are removed when the resistive L-network is used (Fig. 4.16). The L-network also reduces $S_{2,1}$ by ∼11 dB due to losses in the resistors .

With both matching geometries, a signal traveling at the speed of light proceeds the slow pulse that is a factor of ∼10 lower in amplitude (Fig. 4.17). The speed of light signal is not reflected when it reaches the end of the transmission line, however, it is seen again when the slow signal reaches the end of the helix. This signal may be a higher order mode. However,

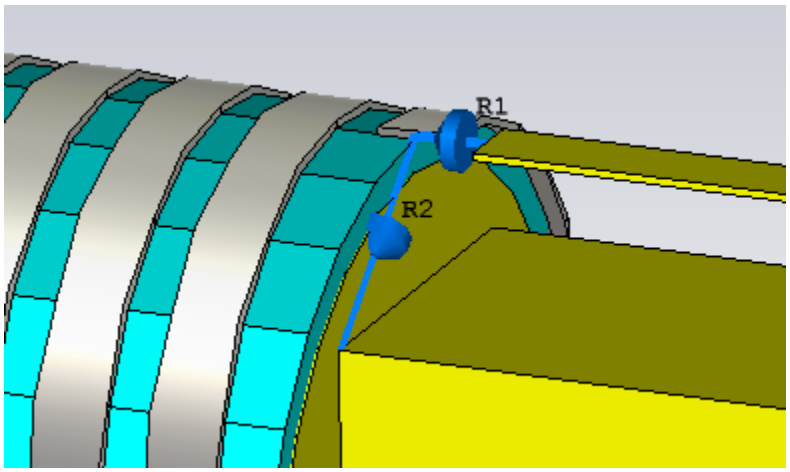

Figure 4.15: Lumped elements used for impedance matching.

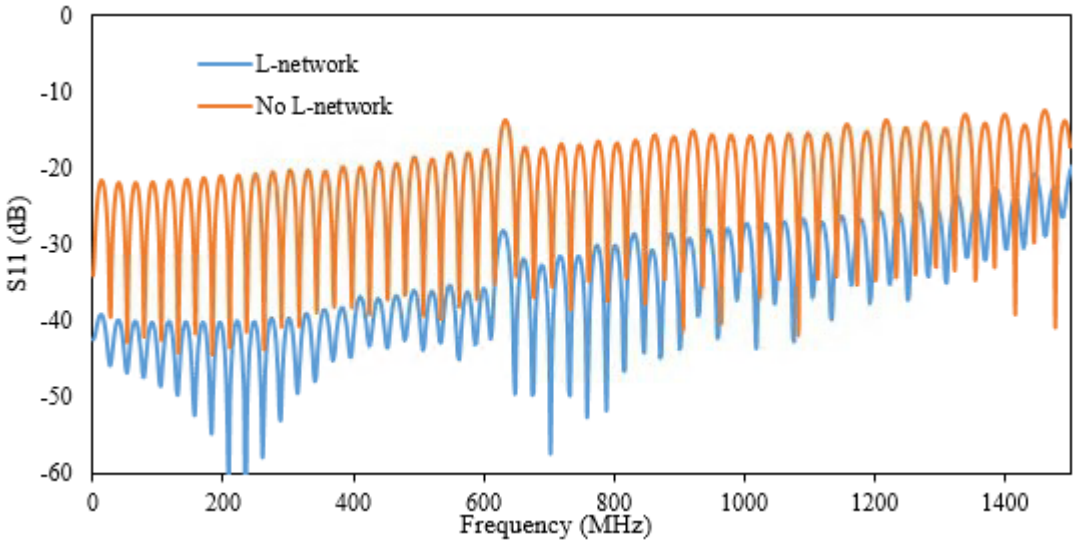

Figure 4.16: $S_{1,1}$ with and without a resistive L-network for matching.

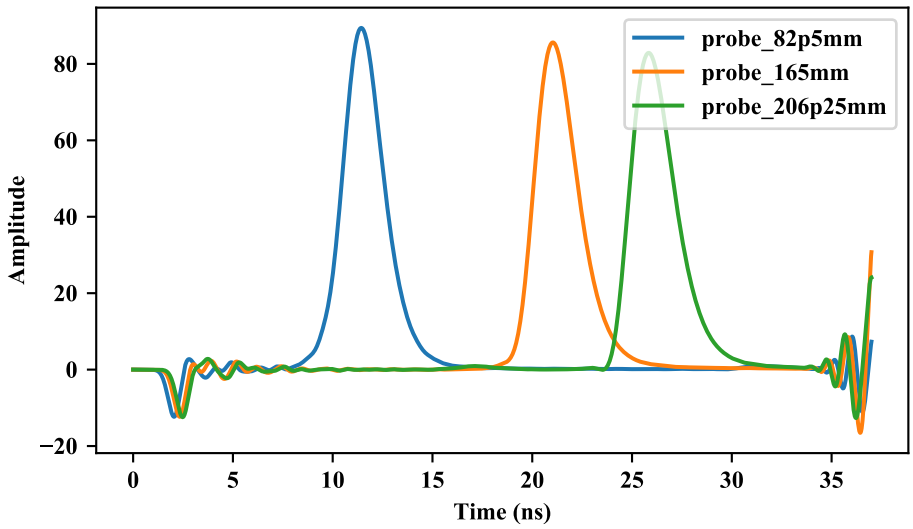

Figure 4.17: The radial electric field at the wall shows minimal deformation during propagation along the transmission line. The slow pulses are proceeded by a smaller speed of light signal that reappears once the slow pulse has reached the end of the transmission line.

the amplitude of the fast signal is independent of θ therefore it is not an $n > 0$ mode of the sheath helix. It could also be an evanescent mode, but the amplitude does not decrease with propagation distance. These signals may also be an artifact of the simulation.

4.3.2 Dispersion

The dispersion was measured by inputting a Gaussian pulse into the system and measuring the radial electric field using probes along the transmission line. Nine probes were evenly spaced along the transmission line. The probes should be placed as close as possible to the helix to measure the largest bandwidth. However, if a probe is too close it will measure near field effects from the winding of the helix. To ensure minimal near field effects, eight probes were placed around the helix in $\pi/4$ increments. The probes were moved from 0.25 mm to 2 mm off the helix to find the radius where the field is no longer significantly dependent on θ.

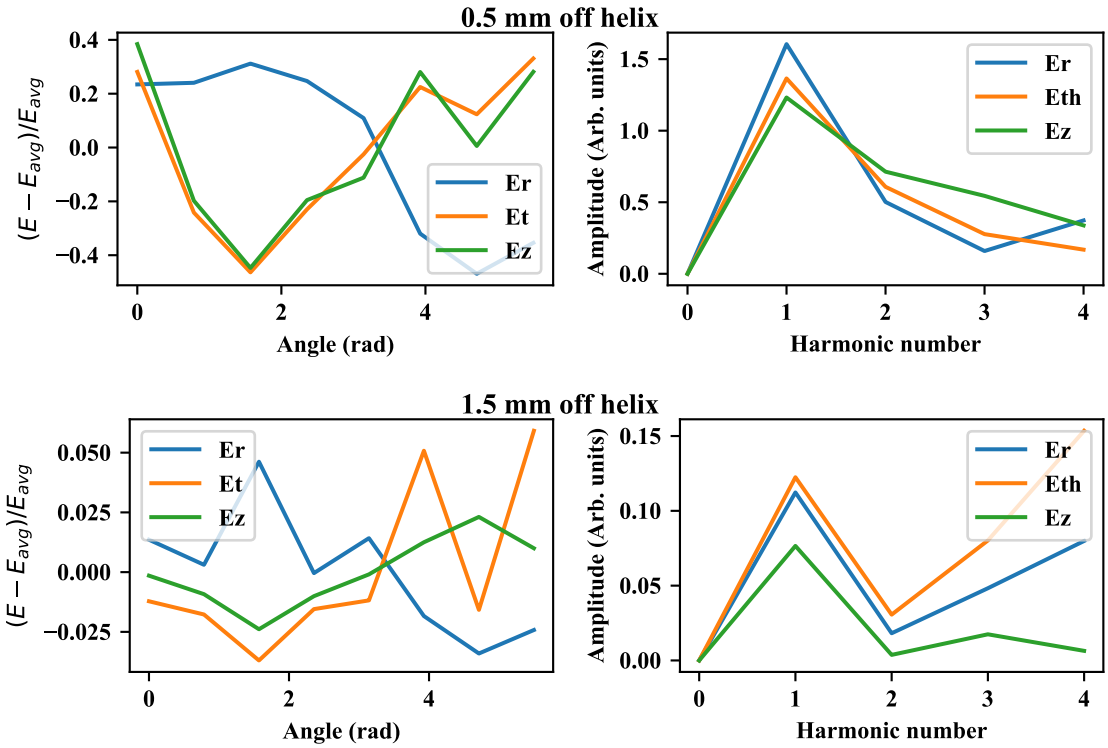

Figure 4.18: The electric field 0.5 mm away from the helix has a strong first harmonic due to the helix windings. At 1.5 mm away from the helix the the angular dependence is significantly reduced.

The fields 0.25 mm from the helix vary chaotically with θ by $\pm 50\%$. At 0.5 mm off the helix, the variations are slightly reduced and show a strong $\cos(\theta)$ dependence. This behavior is sufficiently reduced for the fields 1.5 mm radially off from the helix (Fig. 4.18) with variations on the 1-4% level. While the E_z field still has a clear $\cos(\theta)$ dependence its amplitude is small enough to ignore.

The probes were placed 1.5 mm away from the helix to maximize the measured bandwidth and avoid near field effects (Fig. 4.19). The time signals from each probe were transformed into the frequency domain to find the phases as a function of frequency. A linear fit of the phases as a function of the probe position gives the phase velocity for each frequency (Fig.

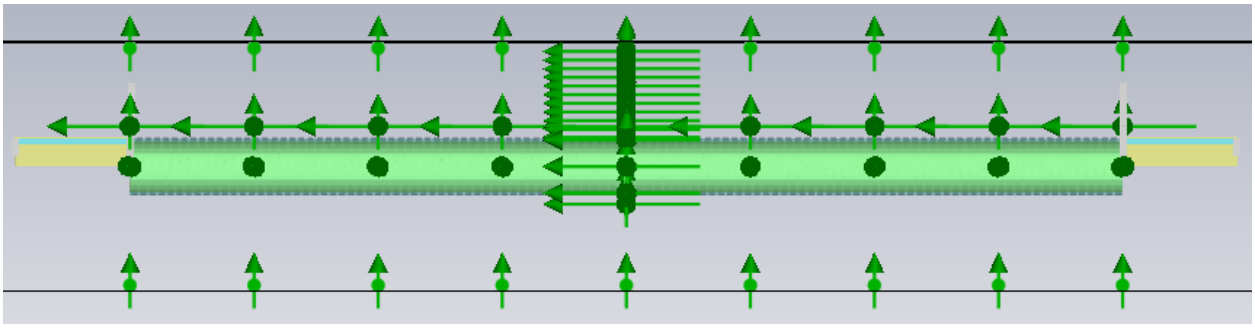

Figure 4.19: Probe suite used to measure the fields from the helix.

4.20)

$$\phi(f, z) = \frac{f}{v_p} z. \tag{4.50}$$

The measured phase velocity agrees with the sheath helix model within 3% up to 2 GHz at which point, the signals is dominated by noise. However, near exact agreement can be achieved by assuming $a = a + \Delta a = 0.51$ mm in the analytic model (Fig. 4.21). This value is the sum of the helix radius and the helix thickness in the simulation. This scaling also holds for thicker helices, however, the agreement is poorer most likely because the assumption of an infinitesimally thin helix used in the analytic model no longer holds.

The cause of this phenomenon is unknown and it is particularly strange considering in the simulations the helix conductor is placed at $r \in [a - \Delta a/2, a + \Delta a/2]$. The helix conductor does not reach $a + \Delta a$. In addition, increasing Δa will reduce s which should cause significant changes in the impedance and dispersion, but these effects are not seen.

4.3.3 Impedance

The impedance of the helical line was measured using $S_{1,1}$. For this measurement, the stripline impedance was changed to 102.5 Ω to be unequal to the helix impedance of $Z_{\text{helix}} =$ 64.5 Ω and matched to the helix using a resistive L-network to damp the resonances. In

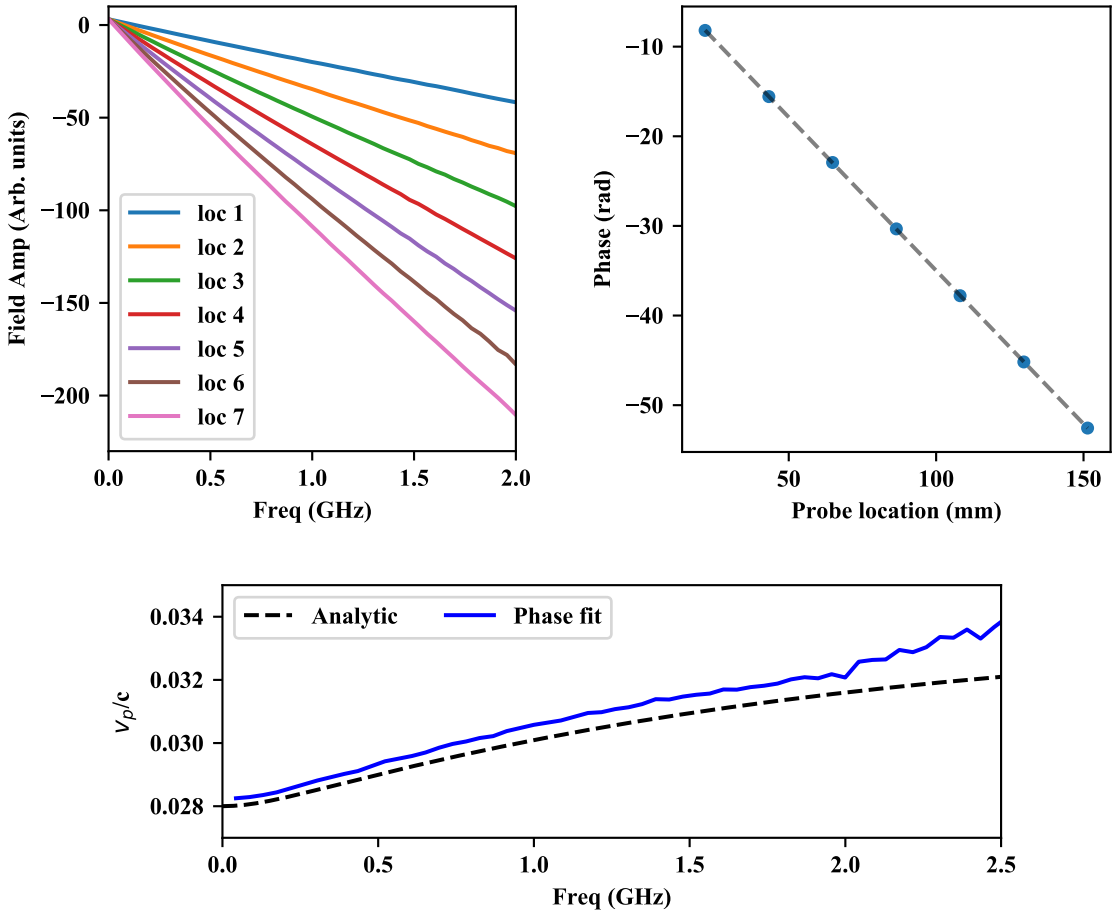

Figure 4.20: The phases at each frequency (top left) for each probe is fitting according to Eq. 4.50 to calculate the phase velocity. Shown is the fitting at 80 MHz (top left).

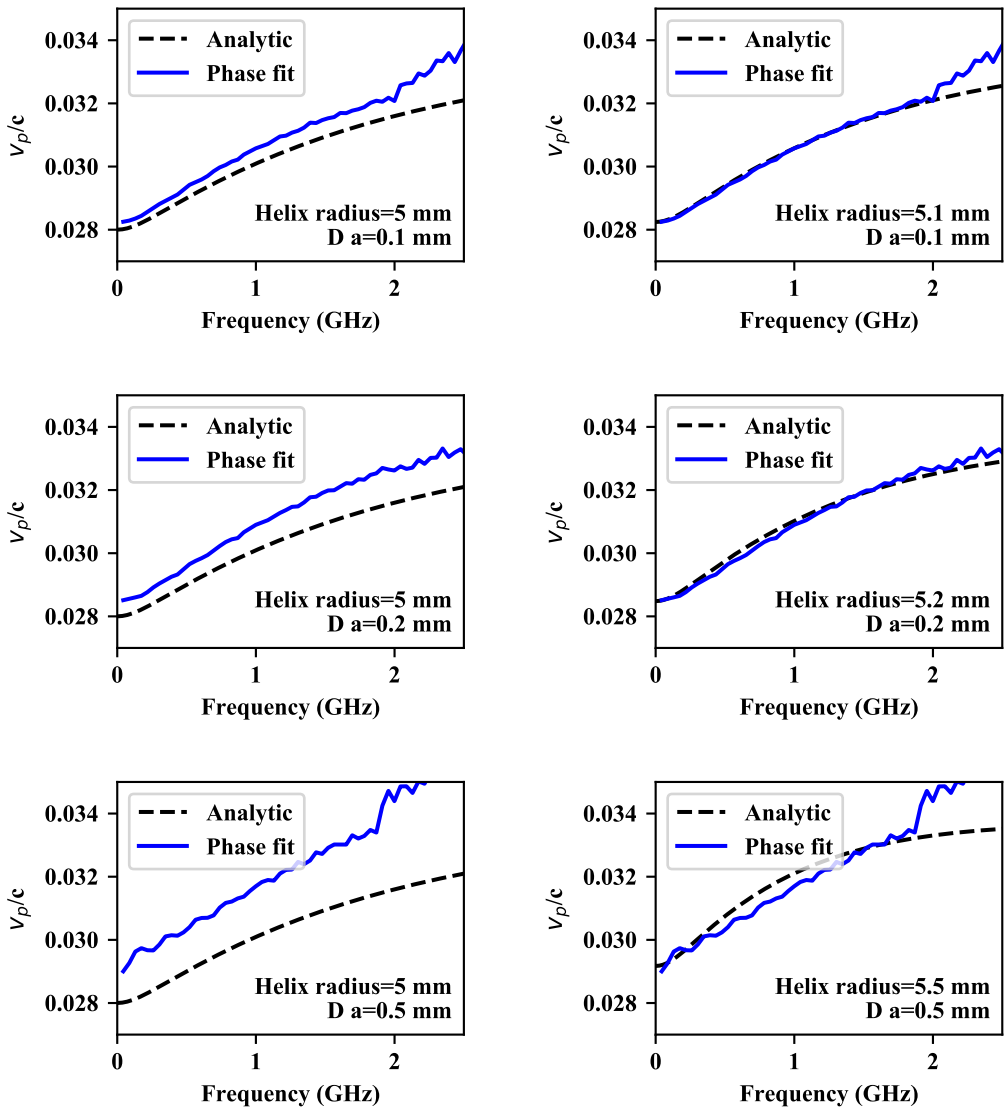

Figure 4.21: Exact matching of the dispersion can be achieved by setting the helix radius in the analytic model to the outer radius of the helix used in the simulations. The helix radius in simulations is 5 mm for all presented measurements with Δa given by Da on each plot. The stated helix radius is the radius used to analytically calculate the dispersion.

addition, to increase $S_{1,1}$ the L network was purposely poorly matched. With this network the helix impedance is given by:

$$Z_{\text{helix}} = \left(R_{sh}^{-1} + \left[Z_0 \frac{1 - S_{11}}{1 + S_{11}} + R \right]^{-1} \right)^{-1} \tag{4.51}$$

where Z_0 is the impedance of the microstrip, R is the series resistance, and R_{sh} is the shunt resistance.

The real part of the impedance from simulations agrees with the analytic model within 3% up to 2 GHz. The simulation also showed a small reactance that was <15% of the real impedance caused by material losses in the simulation which are not modeled analytically(Fig. 4.22). The reatance was not matched because the mismatch from using only the microstrip is deemed small enough because the size of the imaginary component is on the same order as the variation in the real component. Therefore there would be no significant improvement to the matching without also improving the match to the resistive component. In addition, when constructing a helical transmission line for the test stand, it would be best to use $s < 0.5$ mm which will result in less frequency dependence in Z and a better match.

4.3.4 Fields

The electric field was measured using field probes at multiple radii along the transmission line. The fields measured 1.5 mm off the helix were used to determine the field coefficients. The expected field near the pipe wall was then found using these coefficients and it agrees within 10% with the simulation results up to 0.4 GHz where noise starts to dominate (Fig. 4.23).

A significant feature of the fields, is near the helix the amplitude of the E_r field decreases

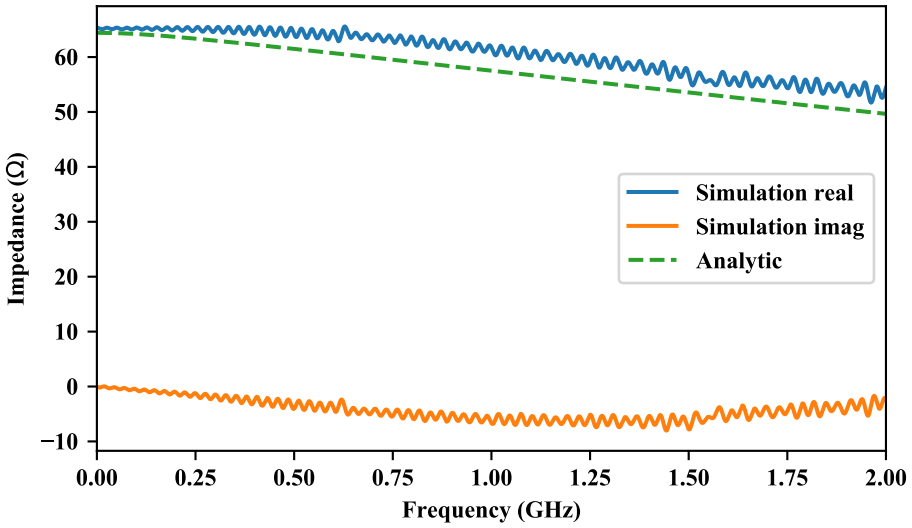

Figure 4.22: The analytic impedance matches the results from simulations with 5%

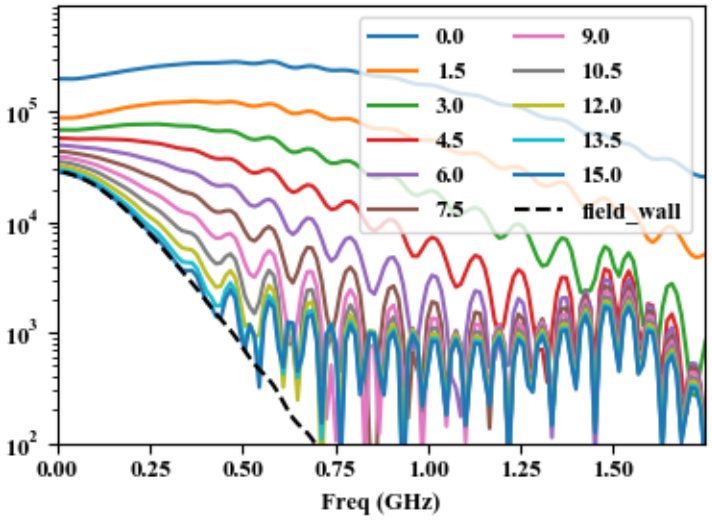

Figure 4.23: The field coefficients were derived from fitting the electric field 1.5 mm from the helix. These are used to calculate the analytic electric field 15 mm from the helix. This field profile agrees well with simulations.

at low frequency (Fig. 4.24). This is not present in the Gaussian input pulse nor are there signs of losses or reflections in the S parameters at low frequency.

It was found that this change in the spectra of the external fields is due to the coupling between the internal and external regions of the transmission line. This coupling can be derived analytically by the ratio of the internal and external radial electric fields at the helix

$$\left.\frac{E_{r,e}}{E_{r,i}}\right|_{r=a} = \frac{\gamma_i K_0^2(\gamma_e R_e) w_{1,i} w_{2,e}}{\gamma_e K_0^2(\gamma_i R_i) w_{1,e} w_{2,i}}. \tag{4.52}$$

This can be inverted to determine the appropriate input pulse to have a Gaussian field profile at the helix in the external region. This coupling agrees with the results of simulations (Fig. 4.24). While an exact input can be generated, for simplicity, for a Gaussian pulse input in the internal region, the spectra near the helix can be roughly fit to the difference of two Gaussians (Fig. 4.24)

$$E_{r,e}\big|_{r=a} \approx G_1 \exp(-2\pi^2\sigma_1^2 f^2) - G_2 \exp(-2\pi^2\sigma_2^2 f^2). \tag{4.53}$$

The standard deviations and amplitudes of the two Gaussian can be determined from the standard deviation σ_i of the input Gaussian pulse. For the parameters given in Table 4.1, the coefficients can be determined by

$$G_1 = 0.119e^{-0.653\sigma_i} \tag{4.54}$$

$$G_2 = 0.066e^{-0.826\sigma_i} \tag{4.55}$$

$$\sigma_1 = 0.905\sigma_i - 0.005 \tag{4.56}$$

$$\sigma_2 = 1.582\sigma_i + 0.111 \tag{4.57}$$

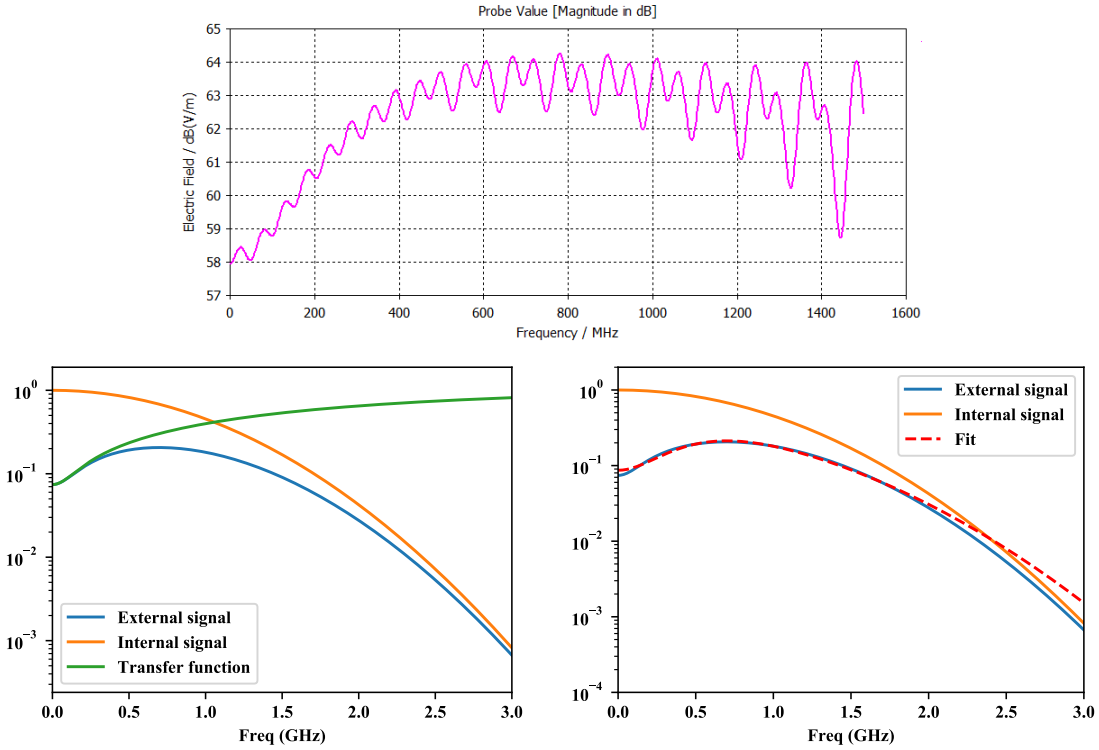

Figure 4.24: The field in the external region is suppressed at low frequency compared to the field in the internal region. This matches with signals measured 1.5 mm off the helix in simulations. For a Gaussian input, the field in the external region can be roughly fit to the difference of two Gaussians.

for σ_i in ns. This fitting can be inverted to determine the required input to achieve a Gaussian pulse of length σ_i in the external region. However, the quality of this fit deteriorates for pulses less than 100 ps rms.

4.3.5 Beam comparison

The electric field propagated by the helical transmission line needs to replicate the fields from a beam. The longitudinal profile can be set by the input pulse with proper consideration of the internal-external coupling. However, for non-relativistic beam, the transverse profile also affects the BPM measurements. The radial electric field from a line charge has the same general dependence on coordinates as the field from the helix (Eq. 4.12), however the beam

has g as a transverse propagation constant which corresponds to a fixed beam velocity while the helix has γ_e and the phase velocity varies with frequency.

This disparity in propagation constants causes the fields to scale differently with r therefore the fields of a beam and the helix cannot be the same over the entire pipe aperture. In order to replicate the fields from a beam, the longitudinal profile of the helix's external fields at the helix must match the longitudinal profile of the beam distribution. The transverse distribution of the beam can then be set by requiring E_r at the pipe wall to be similar. The radial electric field of the beam was fit to the field of the helix for a pencil beam, ring beam, and uniform beam using the beam radius as a fit parameter (Fig. 4.25). The ring distribution best fit the helix fields with deviation of at most 10% up to 1 GHz. Up to 0.5 GHz, the bandwidth of the FRIB BPMs, the ring distribution varies from the helix field by less than 1%.

The variation of the phase velocity of the helix also means a choice must be made for the velocity of the modeled beam. It was found for fitting up to 1 GHz, using $v_p(f = 1 \text{ GHz})$ gives the best fit. The complications this variation in phase velocity causes with modeling the beam is an addition reason to flatten the dispersion curve.

4.3.6 Offset helices

The analytic and simulation work presented in this chapter has all been concerned with centered helices. However, for the test stand to calibrate BPMs, the helix must be moved off center to replicate offset beams. The helix was moved off center in the pipe in 2 mm steps up to 10 mm. At each step the the dispersion was calculated from probes measuring the electric field 1.5 mm off the helix. No significant change in the dispersion was seen with offsetting the helix up to 2 GHz(Fig. 4.26). In addition, $S_{1,1}$ was also recorded for each helix

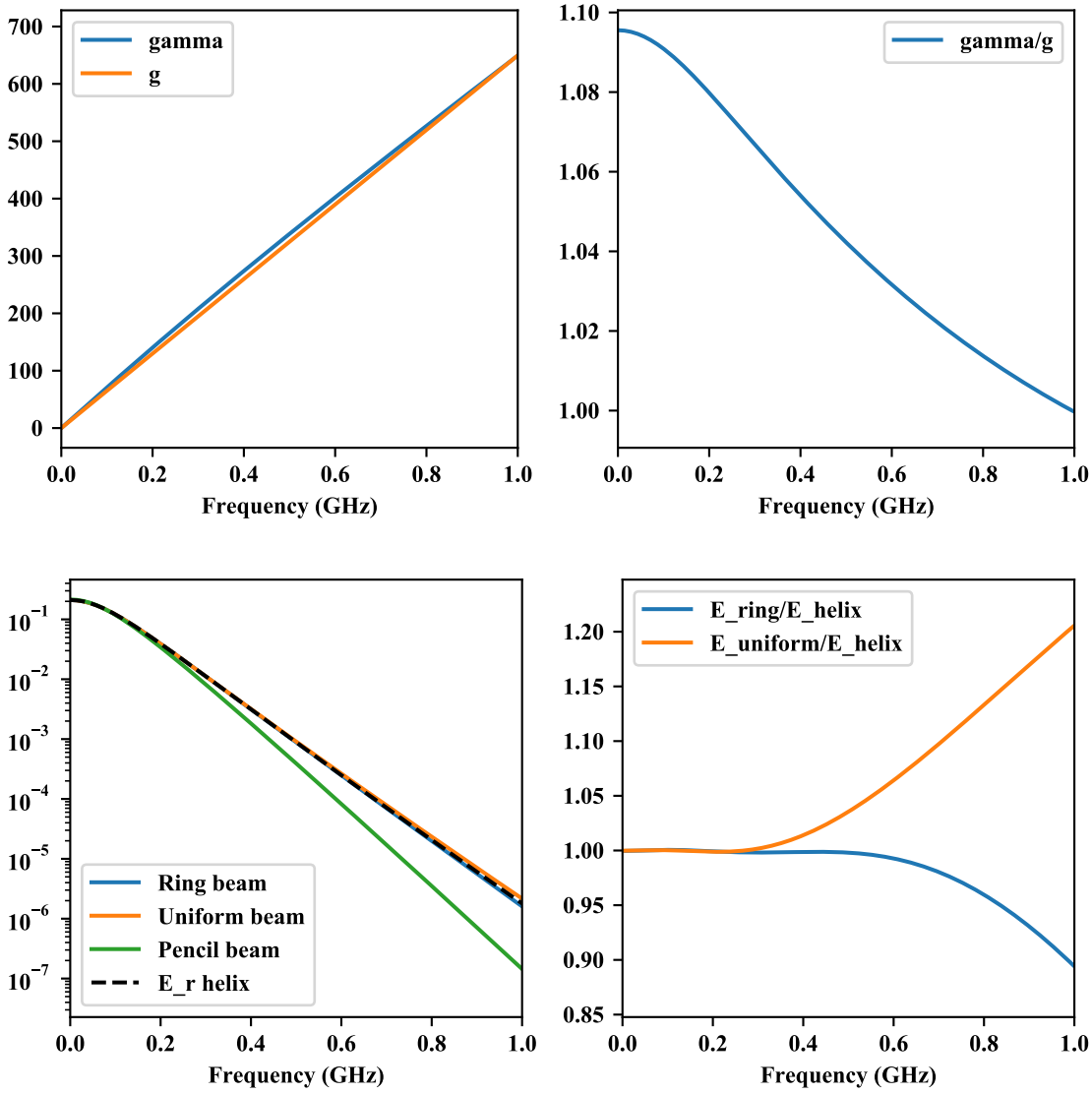

Figure 4.25: The fields from the helix best match a ring beam. R_i=4.5 mm, a=5 mm, R_e=20.65 mm, ψ=0.05, $\epsilon_i = 3.5\epsilon_0$

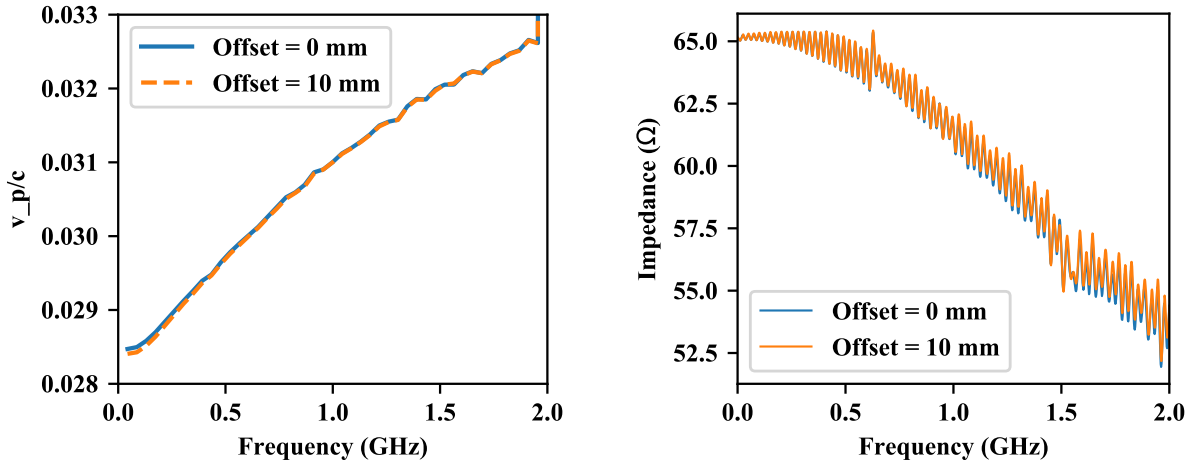

Figure 4.26: The dispersion and impedance sees no significant variation due to offsets up to 10 mm offsets.

location using the mismatched L-pad to measure the impedance. Once, again, no significant change in the impedance was seen when the helix was offset (Fig. 4.26). These are beneficial behaviors because no additional considerations need to be taken when the helix is offset.

Chapter 5

Summary

Further development of current diagnostic devices to measure low β beams is a challenging problem. For BPMs and other non-intercepting devices, the measured signals do not directly represent the beam unlike at higher energies. Therefore, care must be taken to understand exactly how the measurements relate to the beam. The measured electric fields from the beams are affected by not only the precise transverse and longitudinal bunch distribution, but also the geometry of the pickup. While in theory this can be leveraged to use a BPM to measure the transverse and longitudinal profiles of the beam, there can be too many variables and assumptions in the models to give reliable results. The analysis in chapter 3 attempts to remove as much model dependence as possible and this caused these measurements to fail at low energy in the MEBT of FRIB. I believe it is possible with additional model dependence, these measurements could be realized for a proton machine at the same energy where minimal retuning is needed. For heavy ion machines such as FRIB, different ion species with different charge to mass ratios will be accelerated and each one will have a different transverse profile and it becomes less practical to develop a new model for each one. At higher energies, once the transverse distribution dependence dies out, these measurements should still possible even for heavy ion machines and allow for using the extensive prevalent BPMs as longitudinal profile monitors. However, further calibrations of the FRIB BPMs at these higher energies are required for these measurements.

Key to the broadband BPM measurements and position measurements at low β is un-

derstanding the signals generated on the buttons and how they relate to the beam. Chapter 3 presents this solely through analytical and numerical methods. However, a test stand as described in chapter 4 would be greatly beneficial and allow for controlled measurements with a BPM that will be used in the beamline. What remains for this project is to construct and validate analytic and numeric model before it can be used as a test stand. This test stand would not only be useful for further studies of wide bandwidth BPM measurements but also for calibrating narrowband position measurements for non-relativistic effects.

Lastly, with phase space measurements, the detailed beam distribution is directly measured, however, standard practice to only take rms values hides many features. Modeling the beam in phase space to allow direct comparisons is challenging and the analysis in chapter 2 attempts to alleviate some of these difficulties by using action-phase coordinates which eliminates variations in linear optics. However, this method relies heavily on having an adequate model of the beam core for fitting the central parameters. In the PIP2IT MEBT the core was primarily Gaussian. However, while no transverse phase space distribution measurements were made in the FRIB MEBT, based on the profiles measured by the wire scanner, I believe developing a model of the core would be more difficult there. The analysis of the phase portraits in action-phase coordinates was intended to be used to study tail growth in the PIP2IT MEBT. However, beam jitter and electron noise confounded the measurements and making definitive claims about the tails was challenging. This analysis would benefit if it was applied to cleaner signals from a device with a larger dynamic range.

All three of these devices/techniques warrant further investigation and have the possibility to greatly benefit the beam diagnostic's toolbox. The broadband BPM measurements have the most obvious advantage of turning every BPM into a non-interceptive longitudinal profile monitor. The helical test stand should accompany these BPM measurements for

measurements at low energies. And the action-phase analysis can give a more detailed view of the beam distribution with less concern of the optics.

BIBLIOGRAPHY

BIBLIOGRAPHY

[1] Alan S. Fisher. Summary of the 2014 Beam-Halo Monitoring Workshop. In *Proceedings, 4th International Beam Instrumentation Conference, IBIC2015*, 2016. THBLA01.

[2] A. Aleksandrov and A. Shishlo. Path to beam loss reduction in the sns linac using measurements, simulation and collimation. In *Proc. of HB'16*, 2016. "THAM5Y01".

[3] I. Reichel, H. Burkhardt, and G. Roy. Observation and simulation of beam tails in lep. In *Proceedings of the 1997 Particle Accelerator Conference*, volume 2, pages 1819–1821 vol.2, Vancouver, BC, Canada, 1997. IEEE.

[4] R. Yang, T. Naito, S. Bai, A. Aryshev, K. Kubo, T. Okugi, N. Terunuma, D. Zhou, A. Faus-Golfe, V. Kubytskyi, S. Liu, S. Wallon, and P. Bambade. Evaluation of beam halo from beam-gas scattering at the kek accelerator test facility. *Phys. Rev. Accel. Beams*, 21:051001, May 2018.

[5] S. Y. Lee. *Accelerator physics*. World Scientific, Singapore, 1999.

[6] P. F. Derwent, J.-P. Carneiro, J. Edelen, V. Lebedev, L. Prost, A. Saini, A. Shemyakin, and J. Steimel. PIP-II injector test: challenges and status. In *Proc. of LINAC'16*, September 2016. WE1A01.

[7] P. W. Allison, J. D. Sherman, and D. B. Holtkamp. An emittance scanner for intense low-energy ion beams. *IEEE Transactions on Nuclear Science*, 30(4):2204–2206, 1983.

[8] A. Shemyakin, J.-P. Carneiro, B. Hanna, V. Lebedev, L. Prost, V. Scarpine A. Saini, V.L.S. Sista, and C. Richard. Experimental study of beam dynamics in the PIP-II MEBT prototype. In *Proc. of HB'18*, June 2018. MOP1WB03.

[9] A. Saini, B. Hanna, J. Huber, L. Prost, V. Scarpine, J. Steimel, S.V.L.S. Rao, and C. Richard. Beam tests of the pip-ii injector test radio frequency quadrupole. *Nuclear Instruments and Methods in Physics Research Section A: Accelerators, Spectrometers, Detectors and Associated Equipment*, 978:164368, 2020.

[10] C. Richard, M. Alvarez, J. P. Carneiro, B. Hanna, L. Prost, A. Saini, V. Scarpine, and A. Shemyakin. Measurements of a 2.1 mev h- beam with an allison scanner. *Review of Scientific Instruments*, 91(7):073301, 2020.

[11] M. Reiser. *Theory and Design of Charged Particle Beams*, volume 2. Wiley-VCH, Weinheim, Germany, 1994.

[12] L. Prost, J.-P. Carneiro, and A. Shemyakin. Low emittance growth in a low energy beam transport line with un-neutralized section. *Phys. Rev. Accel. Beams*, 21:020101, Feb 2018.

[13] Richard D'Arcy and Alexander Shemyakin. Calculation of the effect of slit size on emittance measurements made by a two-slit scanner, 2016.

[14] A. Saini and A. Shemyakin. Optical design of the PI-Test MEBT beam scraping system. In *Proc. of LINAC'16*, 2016. THPRC026.

[15] Tracewin code. http://irfu.cea.fr/dacm/logiciels/.

[16] L.R. Prost, R. Andrews, C.M. Baffes, J.-P. Carneiro, B.E. Chase, A.Z. Chen, E. Cullerton, P. Derwent, J.P. Edelen, J. Einstein-Curtis, D. Frolov, B.M. Hanna, D.W. Peterson, G.W. Saewert, A. Saini, V.E. Scarpine, A.V. Shemyakin, V.L. Sista, J. Steimel, D. Sun, A. Warner, and C. Richard. PIP-II injector test warm front end: Commissioning update. In *Proc. of HB'18*, June 2018. THYGBF2.

[17] J. Cuperus. Monitoring of Particle Beams at High Frequencies. *Nucl. Instrum. Meth.*, 145:219, 1977.

[18] Robert E. Shafer. Beam position monitor sensitivity for low-β beams. *AIP Conference Proceedings*, 319(1):303–308, 1994.

[19] Oren Yair, Jenna Crisp, Gerlind Kiupel, Steve Lidia, and Robert Webber. Frib beam position monitor pick-up design. In *Proceedings, International Beam Instrumentation Conference, IBIC2014*, 09 2014.

[20] A. Shishlo and A. Aleksandrov. Noninterceptive method to measure longitudinal twiss parameters of a beam in a hadron linear accelerator using beam position monitors. *Phys. Rev. ST Accel. Beams*, 16:062801, Jun 2013.

[21] Cst studio suite. https://www.cst.com.

[22] P Forck, P Kowina, and D Liakin. Beam position monitors. In *CERN Accelerator School: Course on Beam Diagnostics*, 05 2008.

[23] Robert E. Shafer. Beam position monitoring. *AIP Conference Proceedings*, 212(1):26–58, 1990.

[24] Samuel Sensiper. *Electromagnetic wave propagation on helical conductors*. PhD thesis, Massachusetts Institute of Technology, 1951.